

REPORT DOCUMENTATION PAGE

Form Approved
OMB No. 0704-0188

The public reporting burden for this collection of information is estimated to average 1 hour per response, including the time for reviewing instructions, searching existing data sources, gathering and maintaining the data needed, and completing and reviewing the collection of information. Send comments regarding this burden estimate or any other aspect of this collection of information, including suggestions for reducing the burden, to Department of Defense, Washington Headquarters Services, Directorate for Information Operations and Reports (0704-0188), 1215 Jefferson Davis Highway, Suite 1204, Arlington, VA 22202-4302. Respondents should be aware that notwithstanding any other provision of law, no person shall be subject to any penalty for failing to comply with a collection of information if it does not display a currently valid OMB control number.

PLEASE DO NOT RETURN YOUR FORM TO THE ABOVE ADDRESS.

1. REPORT DATE (DD-MM-YYYY) 5/Nov/2001	2. REPORT TYPE DISSERTATION	3. DATES COVERED (From - To)		
4. TITLE AND SUBTITLE ROTATIONAL RELAXATION IN CARBON MONOXDIE		5a. CONTRACT NUMBER	5b. GRANT NUMBER	
		5c. PROGRAM ELEMENT NUMBER		
6. AUTHOR(S) CAPT PHIPPS STEPHEN P		5d. PROJECT NUMBER	5e. TASK NUMBER	
		5f. WORK UNIT NUMBER		
7. PERFORMING ORGANIZATION NAME(S) AND ADDRESS(ES) UNIVERSITY OF NEW MEXICO			8. PERFORMING ORGANIZATION REPORT NUMBER CI01-298	
9. SPONSORING/MONITORING AGENCY NAME(S) AND ADDRESS(ES) THE DEPARTMENT OF THE AIR FORCE AFIT/CIA, BLDG 125 2950 P STREET WPAFB OH 45433			10. SPONSOR/MONITOR'S ACRONYM(S)	
			11. SPONSOR/MONITOR'S REPORT NUMBER(S)	
12. DISTRIBUTION/AVAILABILITY STATEMENT Unlimited distribution In Accordance With AFI 35-205/AFIT Sup 1				
13. SUPPLEMENTARY NOTES				
14. ABSTRACT				
20011115 154				
15. SUBJECT TERMS				
16. SECURITY CLASSIFICATION OF: a. REPORT		17. LIMITATION OF ABSTRACT	18. NUMBER OF PAGES 165	19a. NAME OF RESPONSIBLE PERSON 19b. TELEPHONE NUMBER (Include area code)

**ROTATIONAL RELAXATION
IN
CARBON MONOXIDE**

by

Stephen P. Phipps
Captain, USAF

B.S., Physics, Brigham Young University, 1991
M.S., Physics, University of New Mexico, 1996

Dissertation

Submitted in Partial Fulfillment of the
Requirements for the Degree of

Doctor of Philosophy
Optical Sciences

The University of New Mexico
Albuquerque, New Mexico

2001

Stephen P. Phipps

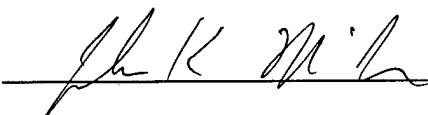
Candidate

Physics and Astronomy

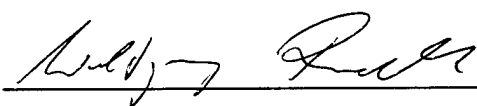
Department

This dissertation is approved, and it is acceptable in quality
and form for publication on microfilm:

Approved by the Dissertation Committee:



, Chairperson



Accepted:

Dean, Graduate School

Date

ROTATIONAL RELAXATION IN CARBON MONOXIDE

Stephen P. Phipps

B. S., Physics, Brigham Young University, 1991

M. S., Physics, University of New Mexico, 1996

Ph.D., Optical Sciences, University of New Mexico, 2001

ABSTRACT

The results of an infrared-infrared pump-probe experiment investigating the rate of rotational self-relaxation in carbon monoxide are presented. Room-temperature CO molecules in the ground electronic and vibrational state were excited into the $J = 0, 7$, and 14 rotational levels of $v = 2$ using a pulsed, narrow-band optical parametric oscillator. A cw lead-salt diode laser, tuned to resonant transitions between $v = 2$ and 3, probed subsequent population changes in the $J = 0 - 18$ rotational levels. The time-dependent absorption linewidths of the probe transitions caused by the sub-Doppler OPO pump were also measured. The rotational populations were compared with theoretical predictions based on the statistical power gap, statistical power exponential gap, modified exponential gap, and energy corrected sudden rate constant models. The pump-probe data show that rotational energy transfer occurs faster and multi-quantum transitions occur more often than one would predict based on previously published CO-CO collision data. Homonuclear propensity is clearly evident in the pump-probe data but only for transitions with small energy gaps. The linewidth measurements indicate the energy gap between rotational levels rather than the difference in angular momentum controls rotational energy transfer in carbon monoxide.

ROTATIONAL RELAXATION IN CARBON MONOXIDE

Stephen P. Phipps

B. S., Physics, Brigham Young University, 1991

M. S., Physics, University of New Mexico, 1996

Ph.D., Optical Sciences, University of New Mexico, 2001

ABSTRACT

The results of an infrared-infrared pump-probe experiment investigating the rate of rotational self-relaxation in carbon monoxide are presented. Room-temperature CO molecules in the ground electronic and vibrational state were excited into the $J = 0, 7$, and 14 rotational levels of $v = 2$ using a pulsed, narrow-band optical parametric oscillator. A cw lead-salt diode laser, tuned to resonant transitions between $v = 2$ and 3, probed subsequent population changes in the $J = 0 - 18$ rotational levels. The time-dependent absorption linewidths of the probe transitions caused by the sub-Doppler OPO pump were also measured. The rotational populations were compared with theoretical predictions based on the statistical power gap, statistical power exponential gap, modified exponential gap, and energy corrected sudden rate constant models. The pump-probe data show that rotational energy transfer occurs faster and multi-quantum transitions occur more often than one would predict based on previously published CO-CO collision data. Homonuclear propensity is clearly evident in the pump-probe data but only for transitions with small energy gaps. The linewidth measurements indicate the energy gap between rotational levels rather than the difference in angular momentum controls rotational energy transfer in carbon monoxide.

**ROTATIONAL RELAXATION
IN
CARBON MONOXIDE**

by

Stephen P. Phipps

B.S., Physics, Brigham Young University, 1991
M.S., Physics, University of New Mexico, 1996

Dissertation

Submitted in Partial Fulfillment of the
Requirements for the Degree of

**Doctor of Philosophy
Optical Sciences**

The University of New Mexico
Albuquerque, New Mexico

December 2001

ACKNOWLEDGMENTS

This work was funded by the United States Air Force and performed at the Air Force Research Laboratory's High Power Gas and Chemical Laser Branch (AFRL/DELC) at Kirtland Air Force Base, Albuquerque, New Mexico. I am grateful for the ever-willing assistance of the branch members and contractors. In particular, thanks go to Dr. Gordon D. Hager who enthusiastically sponsored and guided the research. His advice and friendship were invaluable.

I am also grateful to Col. James Head and Col. Rolf Enger of the USAF Academy Physics Department for giving me the opportunity to earn this degree.

The views expressed in this dissertation are those of the author and do not reflect the official policy or position of the United States Air Force, Department of Defense, or the U. S. Government.

**ROTATIONAL RELAXATION
IN
CARBON MONOXIDE**

by

Stephen P. Phipps

Abstract of Dissertation

Submitted in Partial Fulfillment of the
Requirements for the Degree of

**Doctor of Philosophy
Optical Sciences**

The University of New Mexico
Albuquerque, New Mexico

December 2001

ROTATIONAL RELAXATION IN CARBON MONOXIDE

Stephen P. Phipps

B. S., Physics, Brigham Young University, 1991

M. S., Physics, University of New Mexico, 1996

Ph.D., Optical Sciences, University of New Mexico, 2001

ABSTRACT

The results of an infrared-infrared pump-probe experiment investigating the rate of rotational self-relaxation in carbon monoxide are presented. Room-temperature CO molecules in the ground electronic and vibrational state were excited into the $J = 0, 7$, and 14 rotational levels of $v = 2$ using a pulsed, narrow-band optical parametric oscillator. A cw lead-salt diode laser, tuned to resonant transitions between $v = 2$ and 3 , probed subsequent population changes in the $J = 0 - 18$ rotational levels. The time-dependent absorption linewidths of the probe transitions caused by the sub-Doppler OPO pump were also measured. The rotational populations were compared with theoretical predictions based on the statistical power gap, statistical power exponential gap, modified exponential gap, and energy corrected sudden rate constant models. The pump-probe data show that rotational energy transfer occurs faster and multi-quantum transitions occur more often than one would predict based on previously published CO-CO collision data. Homonuclear propensity is clearly evident in the pump-probe data but only for transitions with small energy gaps. The linewidth measurements indicate the energy gap between rotational levels rather than the difference in angular momentum controls rotational energy transfer in carbon monoxide.

TABLE OF CONTENTS

Signature Page	i
Title Page	ii
Dedication Page	iii
Acknowledgement Page	iv
Abstract Title Page	v
Abstract	vi
Table of Contents	vii
List of Figures	xi
List of Tables	xiv
Chapter 1: CO and Rotational Relaxation	1
Interest in CO	1
Carbon Monoxide	1
Scientific Interest in CO	2
Air Force Interest in CO	3
Molecular Energy and Energy Transfer	4
Thermal Equilibrium Population Distributions	8
Molecular Energy Transfer and Collisions	10
Molecular Energy Transfer and Optical Transitions	11
The CO Laser and Optical Pumping	12

Previous CO Work	16
Free Jet Experiments	17
Linewidth Experiments	17
Pump-Probe or Double Resonance Experiments	18
Complications with Pump-Probe Experiments	20
Collision Losses from CO($v=2$)	21
Optical Losses and CO($v=2$)	22
Anisotropic Velocity Distribution	22
Angular Momentum Reorientation	23
 Chapter 2: J-Level Populations and Theory	24
Rotational Populations: Experimental	24
Vibrational Relaxation	25
Time-Dependent Velocity Distribution and Lineshape	25
Angular Momentum Reorientation	26
Rotational Populations: theoretical	31
Rate Constant Models	32
 Chapter 3: Equipment and Procedures	37
The OPO	37
Nd:YAG Laser	38
CW Diode Laser	39
OPO Cavity	39
OPO Pulse Characteristics	41
CO Resonance	43
OPO Operating Procedures	45
Experimental Cell	46
Probe Laser (Lead Salt diode laser)	48
Wavelength Tuning	49
Probe Polarization	52

Probe Beam Path	52
InSb Detector	53
Probe, Detector, and Monochromator Operation	56
Probe Absorption and Beer's Law	60
Data Acquisition: The Oscilloscope	62
Data Acquisition: Procedure	66
Data Acquisition: Data Manipulation	67
Different Pressures	67
Pump Energy Fluctuations	69
Experimental Improvements	70
 Chapter 4: Experimental Results	72
Vibrational loss from $v = 2$	72
Lineshape Relaxation	76
The Experiment	77
Equipment Limitations	78
Frequency Calibration and the Pumped Levels	79
Analysis Procedure	81
The Linewidth Data	84
Pump Bandwidth	95
Magnetic Sublevels and the Magic Angle	97
Rotational Relaxation Data	98
Rate Constant Model Fits	116
 Chapter 5: Discussion	121
Fitting Law Analysis	121
Rate Constants and the Intermolecular Potential	123
Rotational Populations	125
Linewidths	126
Homonuclear Propensity and the Intermolecular potential	128

The Dominant Factor: ΔJ or ΔE	129
Future Work	130
Conclusion	130
List of Appendices	131
Appendix A: Computer Study of Optical Pumping	132
Appendix B: The Pump Source for Optical Pumping	138
Appendix C: Coherent Effects in CO	140
Appendix D: OPO Calculations	147
Uniaxial and Biaxial Crystals.	147
Light Propagating Through Uni- and Biaxial Crystals	149
Phase Matching Angles	151
Efficiency	153
The Initial OPO Configuration	153
Appendix E: Mode Matching Circuit	157
References	159

LIST OF FIGURES

Figure 1. Atmospheric transmission vs. wavelength	3
Figure 2. Potential energy diagram for a diatomic molecule	7
Figure 3. Boltzmann distributions	9
Figure 4. Basic pump-probe elements.	18
Figure 5. Energy level diagram showing pump-probe transitions	19
Figure 6. Post-pump population distribution	20
Figure 7. Probe transmission vs. time	21
Figure 8. Post-pump sublevel populations	30
Figure 9. Intermolecular potential variables	35
Figure 10. The experiments major components.	37
Figure 11. The Optical Parametric Oscillator (OPO)	38
Figure 12. OPO pulse profile and bandwidth.	42
Figure 13. OPO spatial profile	43
Figure 14. Pump transmission vs. pressure	44
Figure 15. Seeded and unseeded YAG pulse	47
Figure 16. Diode laser mode hop	51
Figure 17. InSb detector response function	54
Figure 18. Deconvolution of the pumped level	55
Figure 19. P29 probe transmission vs. pressure ($v = 0$ to 1).	56
Figure 20. Evidence for non-resonant modes	58
Figure 21. Testing Beer's Law with the diode.	61
Figure 22. Independent population predictions	62
Figure 23. Oscilloscope averaging and offset abilities	64
Figure 24. Oscilloscope noise subtraction	65
Figure 25. Legitimacy of averaging	65
Figure 26. Scaling data taken at different pressures	68
Figure 27. Vibrational relaxation	72
Figure 28. Sample of vibrational relaxation data	73

Figure 29. Weighted fit to vibrational relaxation data	74
Figure 30. The influence of lineshape relaxation	76
Figure 31. Simulated lineshape data: method 1	77
Figure 32. Simulated lineshape data: method 2	78
Figure 33. Linewidth data	81
Figure 34. Lineshape data	83
Figure 35. Linewidth vs. collision number	83
Figure 36. Linewidth relaxation: P1 pump ($J = 0$ to $J = 5$)	86
Figure 37. Linewidth relaxation: P1 pump ($J = 6$ to $J = 12$)	87
Figure 38. Linewidth relaxation: P1 pump ($J = 13$) and R6 pump ($J = 0$ to $J = 3$)	88
Figure 39. Linewidth relaxation: R6 pump ($J = 4$ to $J = 10$)	89
Figure 40. Linewidth relaxation . R6 pump: ($J = 11$ to $J = 17$)	90
Figure 41. Linewidth relaxation: R13 pump ($J = 7$ to $J = 13$)	91
Figure 42. Linewidth relaxation: R13 pump ($J = 16$ to $J = 18$)	92
Figure 43. Linewidth comparison: P1 pump	93
Figure 44. Linewidth comparison: R6 pump	93
Figure 45. Linewidth comparison: R13 pump.	94
Figure 46. Initial linewidth fractions and error	96
Figure 47. Evidence of magnetic sublevel alignment memory	97
Figure 48. Rotational population: P1 Pump ($J = 0$ to $J = 5$)	100
Figure 49. Rotational Populations: P1 Pump ($J = 6$ to $J = 11$)	101
Figure 50. Rotational Populations: P1 Pump ($J = 12$ to $J = 18$)	102
Figure 51. Rotational Populations: R6 Pump ($J = 0$ to $J = 5$)	103
Figure 52. Rotational Populations: R6 Pump ($J = 6$ to $J = 11$)	104
Figure 53. Rotational Populations: R6 Pump ($J = 12$ to $J = 18$)	105
Figure 54. Rotational Populations: R13 Pump ($J = 0$ to $J = 5$)	106
Figure 55. Rotational Populations: R13 Pump ($J = 6$ to $J = 11$)	107
Figure 56. Rotational Populations: R13 Pump ($J = 12$ to $J = 18$)	108
Figure 57. Start of population growth (R13 pump)	111
Figure 58. Close up of pumped levels	112

Figure 59. Sum of the rotational levels	113
Figure 60. P1 pump populations	115
Figure 61. R6 pump populations	115
Figure 62. R13 pump populations	116
Figure 63. Fitting Errors	118
Figure 64. Fractional error associated with each model	119
Figure 65. Color contour plots of the rate constant matrices	120
Figure 66. Center-of-mass coordinate system for a bimolecular collision	124
Figure 67. The relative speeds of rotational and velocity relaxation	128
Figure 68. The experimental set-up modeled in the AFRL computer code	132
Figure 69. 5-J predicted absorption	134
Figure 70. ASE threshold	135
Figure 71. Diluent effects	136
Figure 72. Pump concept	139
Figure 73. Uniaxial crystal	148
Figure 74. Biaxial crystal	149
Figure 75. Power OPO	155
Figure 76. Main components of the mode matching circuit	158

LIST OF TABLES

Table 1. Spectroscopic Constants for CO	7
Table 2. CO vibrational energies in the electronic ground state	8
Table 3. $\Delta v = 1$ wavelengths in CO	13
Table 4. Einstein A-Coefficients for $\Delta v = 1$ transitions	14
Table 5. Fitting laws	34
Table 6. OPO diode wavenumbers	40
Table 7. Probe laser settings	51
Table 8. Vibrational relaxation data	75
Table 9. Linewidth fit parameters (P1 Pump)	85
Table 10. Linewidth fit parameters (R6 Pump)	85
Table 11. Linewidth fit parameters (R13 Pump)	85
Table 12. Initial and Equilibrium Linewidths	95
Table 13. Pump Bandwidth Calculation Parameters	96
Table 14. P1 pump rotational fit coefficients	109
Table 15. R6 pump rotational fit coefficients	109
Table 16. R13 pump rotational fit coefficients	110
Table 17. RET model parameters	122
Table 18. Literature RET model parameters	122
Table 19. AFRL Code Program Inputs	133
Table 20. Principal indices for KTP at the seed and power OPO wavelengths	149
Table 21. Phase Matching Angles, d_{eff} , and ρ	152
Table 22. Frequency Doubling Efficiency (eo case)	153
Table 23. Seed OPO (eo case) _{XZ-plane} and Power OPO (ooe) _{XZ-plane}	154

CHAPTER 1: CO AND ROTATIONAL RELAXATION

This dissertation describes the most extensive pump-probe investigation of rotational relaxation in CO to date. Rotational relaxation is the transfer of rotational energy that occurs when molecules collide. Rotational relaxation influences how sound and heat propagate through a gas, how rapidly chemical reactions take place, and how molecules absorb light. In CO, the speed of rotational relaxation—characterized by rate constants—has not been precisely measured [1]. The purpose of this experiment was to measure the rate of rotational energy transfer (RET) in CO.

The text is organized as follows. Chapter 1 explains scientific interest in CO, reviews molecular energy states and energy transfer mechanisms, outlines some of the experiments previously done on RET in CO, and previews the complications associated with pump-probe experiments. Chapter 2 rehearses the theory for extracting rate constant information from the intensity data. It also describes the models used to predict rotational relaxation rate constants. Chapter 3 catalogues experimental equipment and procedures and Chapter 4 presents the data and fits to the data. Chapter 5 submits conclusions and suggests topics for further study.

INTEREST IN CO

CO is a surprisingly abundant molecule known mostly as a dangerous pollutant. But it also has practical uses ranging from metal purification to laser remote sensing.

Carbon Monoxide

CO is the second most abundant molecule in the universe after H₂ [2] and is the twelfth largest constituent in earth's atmosphere with a concentration of ~100 ppb. Of CO's six stable isotopes, two make up more than 99.7% of the total: ¹²C¹⁶O (98.66%) and ¹³C¹⁶O (1.10%). CO is produced when carbon-containing fuels are burned, especially when the fuels combust in an oxygen-poor environment such as a poorly ventilated furnace or an automobile engine. Carbon monoxide is colorless, odorless, and when breathed bonds 200 times more often with the iron in hemoglobin than does oxygen. It

also forms a stronger bond than oxygen, making CO difficult to remove from the bloodstream. The symptoms of CO poisoning are deceptively mild starting with headaches and nausea followed by fatigue, unconsciousness, and death. These properties make CO the leading cause of poisoning deaths in the United States [3].

Despite its hazards, carbon monoxide has beneficial uses. Smelters purify iron and nickel with CO, while the chemical industry uses CO to manufacture methanol, ammonia, and acetic acid. CO is a gas additive in semiconductor fluorocarbon processes and acts as a feed gas for semiconductor dry etching. It serves as a gain medium in industrial lasers which cut metal, drill holes in rock, vaporize surface water, act as surgical tools, and alter the surface of synthetic fabrics to make them appear more natural [4][5]. CO lasers operate over a wide range of wavelengths and can remotely detect H_2O , CO_2 , CH_4 , N_2O , NO_2 , NO , acetone, benzene, and methanol [6]. CO's role as a versatile source of infrared laser light prompted this research.

Scientific Interest in CO

Astronomers have detected CO in the sun and other similar stars [7], in the atmospheres of the planets [8], and in interstellar gas clouds [9]. Astrophysicists use CO's emission spectrum to indirectly detect H_2 and other molecules that do not have a spectrum visible from earth [10]. Atmospheric scientists monitor CO concentrations to study seasonal fluctuations in the earth's mesosphere [11], and energy exchange mechanisms in CO reveal how radiative transfer affects climate [12]. Chemists and engineers control combustion processes by detecting CO levels in exhaust products. Finally, CO's simple structure allows theoreticians to accurately model the intermolecular potential and predict collision dynamics, dynamics that affect CO's performance as a laser.

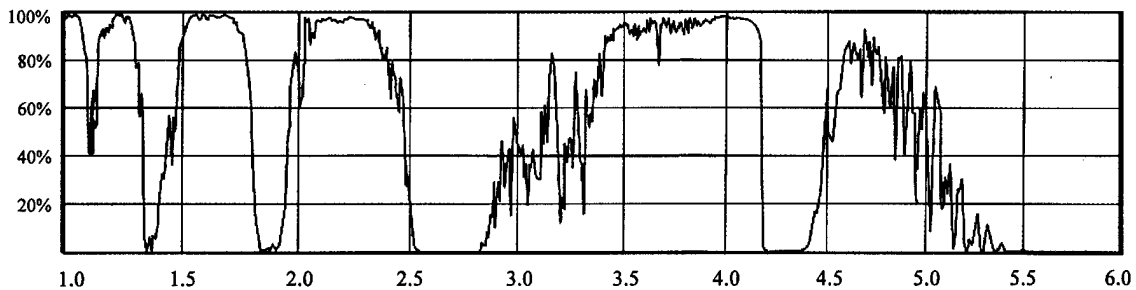


Figure 1. Atmospheric transmission vs. wavelength. The graph shows the atmospheric transmission percentage versus wavelength in μm . Transmission was recorded after the light passed through 1 km of atmosphere along a horizontal path at 15 $^{\circ}\text{C}$ and 46% relative humidity.

Air Force Interest in CO

Only four lasers have demonstrated cw output in excess of 100 kW: the CO_2 gas dynamic laser; the HF and DF chemical lasers; the chemical oxygen iodine laser (COIL); and the electrically excited CO laser. Patel [13] developed the first carbon monoxide laser in 1964 at Bell Laboratories. By the early 1970's, 100-kW class CO lasers had been built by passing an electric discharge through cryogenically cooled CO gas. Super-cooled CO converts up to 90% of the discharge energy into the molecular vibrational energy used for lasing [14]. But the logistics of keeping the CO cold enough to lase efficiently limited the laser's applications. In addition, the atmosphere strongly absorbs the 5-6 μm wavelength light emitted by electric-discharge CO lasers (see Fig. 1). Large-scale CO lasers were eventually abandoned because they could not simultaneously operate at high powers and convenient temperatures with a useful wavelength. Interest has reemerged as scientists develop new methods for making CO lase at shorter wavelengths.

Understanding how these methods work requires understanding the molecule's energy structure.

MOLECULAR ENERGY AND ENERGY TRANSFER

A molecule's energy states are calculated by solving the Schrödinger equation

$$\mathbf{H}\Psi_m(\mathbf{r}, \mathbf{R}) = E_m \Psi_m(\mathbf{r}, \mathbf{R}) \quad (1.1)$$

where \mathbf{H} is the molecular Hamiltonian, $\Psi_m(\mathbf{r}, \mathbf{R})$ is the molecular wave function, and E_m is the total energy of the system made up of translational, vibrational, rotational, and electronic energy. The vectors \mathbf{r} and \mathbf{R} represent the positions of the electrons and atomic nuclei respectively. Eq. (1.2) lists the terms of the Hamiltonian in the molecule's rest frame:

$$\mathbf{H} = -\frac{\hbar}{2m_e} \sum_i \nabla_i^2 - \frac{\hbar}{2} \sum_A \frac{1}{M_A} \nabla_A^2 - \sum_{A,i} \frac{Z_A e^2}{\mathbf{r}_{Ai}} + \sum_{A>B} \frac{Z_A Z_B e^2}{\mathbf{R}_{AB}} + \sum_{i>j} \frac{e^2}{\mathbf{r}_{ij}}. \quad (1.2)$$

From left to right, the terms represent the kinetic energy of the electrons, the kinetic energy of the nuclei, the attraction between the electrons and the nuclei, the repulsion between the nuclei, and the repulsion between the electrons. Using the Born-Oppenheimer approximation [15][16], the first, middle, and last terms in Eq. (1.2) can be condensed into a single function $E_e(\mathbf{R}_{AB})$ representing the electronic energy:

$$\mathbf{H} = -\frac{\hbar}{2} \sum_A \frac{1}{M_A} \nabla_A^2 + \sum_{A>B} \frac{Z_A Z_B e^2}{\mathbf{R}_{AB}} + E_e(\mathbf{R}_{AB}). \quad (1.3)$$

Limiting the calculation to diatomic molecules in the electronic ground state, combining the nuclear and electronic energy terms into a single function $U(\mathbf{R}_{AB})$, and choosing the center-of-mass coordinate system simplifies Eq. (1.3) further

$$\mathbf{H} = -\frac{\hbar}{2\mu} \nabla^2 + U(\mathbf{R}_{AB}) \quad (1.4)$$

where μ is the reduced mass of the two-particle system. Eq. (1.4) represents a free particle in a spherical potential with a well-known solution: $\Psi_m(\mathbf{R}) = R(r) \Theta_{J,m}(\theta) \Phi_m(\phi)$.

The $\Phi_m(\phi)$ and $\Theta_{J,m}(\theta)$ functions are given by

$$\begin{aligned}\Phi_m(\phi) &= \frac{1}{\sqrt{2\pi}} e^{im\phi} \\ \Theta_{J,m}(\theta) &= \left[\frac{(2J+1)(J-|m|)!}{2(J-|m|)!} \right]^{\frac{1}{2}} P_J^{|m|}(\cos\theta)\end{aligned}\quad (1.5)$$

where J is restricted to positive integer values or zero and m is restricted to integer values ranging from $-J$ to J . J characterizes the molecule's angular momentum while m gives the angular momentum's orientation with respect to a conveniently chosen axis. The functions $P_J^{|m|}(\cos\theta)$ are the associated Legendre polynomials. The energies associated with $\Phi_m(\phi)$ $\Theta_{J,m}(\theta)$ are those of the rigid rotator given by

$$E_{J,m} = \frac{\hbar^2}{2I_{in}(R_{AB})} J(J+1) \quad (1.6)$$

where $I_{in}(R_{AB})$ represents the molecule's moment of inertia. As rotational energy does not depend on m , J levels are $2J+1$ degenerate.

Solutions to the radial function $R(r)$ depend on the form of $U(R_{AB})$. Experiment shows that $U(R_{AB})$ often looks like the red curve in Fig. 2. As a first approximation, $U(R_{AB})$ can be represented by the parabolic potential of a harmonic oscillator. Solving for $R(r)$ gives the vibrational energy values

$$E_v = E_0(v + \frac{1}{2}) \quad (1.7)$$

where v has integer values of zero or greater.

When the harmonic oscillator and rigid rotator expressions do not adequately describe the energy states of a molecule, higher order correction terms may be added. Eq. (1.8) gives the corrected expression for vibrational energy in terms of band spectrum coefficients common in spectroscopic literature. The coefficients have units of cm^{-1} .

$$E_v = \omega_e(v + \frac{1}{2}) - \omega_e \chi_e (v + \frac{1}{2})^2 + \omega_e y_e (v + \frac{1}{2})^3 + \dots \quad (1.8)$$

Similar corrections to Eq. (1.6) account for the nuclei pulling farther apart the faster the molecule rotates.

$$E_J = B_v J(J+1) - D_e J^2 (J+1)^2 + \dots \quad (1.9)$$

Vibrational and rotational energies are coupled. As the vibrational energy grows, the average distance between the nuclei expands, increasing the rotational inertia. Rotation stretches the distance between nuclei, altering the vibrational force constant. The coupling is usually small since vibrations have a period of 10^{-14} s while rotations have a period of 10^{-12} s [17]. Vibrational-rotational coupling enters the energy expression of Eq. (1.9) through B_v :

$$B_v = B_e - \alpha_e (v + \frac{1}{2}) + \dots \quad (1.10)$$

With corrections, the energy of a diatomic molecule becomes

$$E_T = E_e(R) + \omega_e(v + \frac{1}{2}) - \omega_e \chi_e (v + \frac{1}{2})^2 + \omega_e y_e (v + \frac{1}{2})^3 + B_v J(J+1) - D_e J^2 (J+1)^2 + \dots \quad (1.11)$$

A more compact expression is given by

$$E_{vJ} = \sum_{i,j} Y_{ij} (v + \frac{1}{2})^i J^j (J+1)^j \quad (1.12)$$

where Y_{ij} are called the Dunham coefficients. Eq. (1.13) relates the spectroscopic constants to the Dunham coefficients:

$$\begin{aligned} Y_{10} &\approx \omega_e & Y_{01} &\approx B_e \\ Y_{20} &\approx -\omega_e \chi_e & Y_{02} &\approx -D_e \\ Y_{30} &\approx \omega_e y_e & Y_{11} &\approx \alpha_e \end{aligned} \quad (1.13)$$

Table 1 gives the spectroscopic constants based on recently published Dunham coefficients [18]. Table 2 gives the energies of the first four vibrational levels. Figure 2 shows the energy levels graphically.

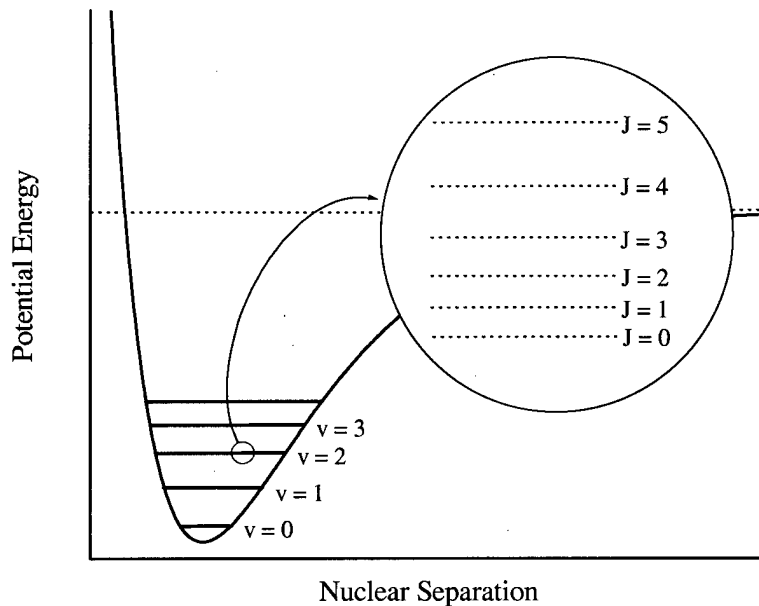


Figure 2. Potential energy diagram for a diatomic molecule. The curve shows the potential energy approximated by the Morse potential. The dashed line represents the dissociation energy. Also shown are the vibrational and rotational energy levels.

Table 1. Spectroscopic Constants for CO

Constant	Value (cm ⁻¹)
ω_e	2169.8124
$\omega_e \chi_e$	13.2879
$\omega_e y_e$	0.0104
B_e	1.9312
D_e	0.0175
α_e	6.12E-06

Table 2. CO vibrational energies in the electronic ground state.
Values have units of cm^{-1} .

	v = 0	v = 1	v = 2	v = 3
J = 0	0.000	2143.270	4260.059	6350.428
1	3.845	2147.080	4263.834	6354.168
2	11.535	2154.700	4271.384	6361.648
3	23.069	2166.130	4282.708	6372.867
4	38.448	2181.369	4297.807	6387.826
5	57.670	2200.416	4316.679	6406.523
6	80.735	2223.271	4339.324	6428.958
7	107.642	2249.933	4365.741	6455.130
8	138.390	2280.400	4395.929	6485.037
9	172.978	2314.673	4429.886	6518.680
10	211.404	2352.749	4467.612	6556.056
11	253.667	2394.627	4509.105	6597.163
12	299.765	2440.305	4554.363	6642.001
13	349.697	2489.782	4603.385	6690.568
14	403.461	2543.056	4656.168	6742.861
15	461.054	2600.124	4712.711	6798.879
16	522.475	2660.984	4773.011	6858.619
17	587.721	2725.635	4837.067	6922.080
18	656.789	2794.073	4904.875	6989.257
19	729.677	2866.296	4976.433	7060.150
20	806.382	2942.301	5051.738	7134.755
21	886.902	3022.085	5130.787	7213.069
22	971.232	3105.645	5213.577	7295.089
23	1059.370	3192.979	5300.105	7380.811
24	1151.313	3284.081	5390.367	7470.234
25	1247.057	3378.950	5484.361	7563.352
26	1346.598	3477.581	5582.081	7660.162
27	1449.933	3579.970	5683.525	7760.661
28	1557.057	3686.114	5788.689	7864.845
29	1667.966	3796.008	5897.568	7972.708
30	1782.657	3909.649	6010.158	8084.248

Thermal Equilibrium Population Distributions

The previous section ignored the translational kinetic energy associated with moving molecules. When molecules collide, they convert kinetic energy into internal energy and vice versa. The energy exchange maintains the thermal equilibrium populations described by the Boltzmann distribution:

$$F_s = \frac{g_s e^{-E_s/kT}}{\sum_{s=0}^{\infty} g_s e^{-E_s/kT}}. \quad (1.14)$$

In Eq. (1.14), F_s represents the fraction of molecules in level s , E_s is the energy value of level s , and g_s is the number of degenerate states in level s . The Boltzmann distribution shows a level's population depends on the energy required to reach that level relative to kT . At room temperature, $kT \approx 205 \text{ cm}^{-1}$. Since the energy gap between electronic and vibrational energy levels is $65,000 \text{ cm}^{-1}$ [19] and 2000 cm^{-1} respectfully, solving Eq. (1.14) shows practically all room temperature CO molecules are in the ground electronic and vibrational levels. In contrast, the rotational levels have small energy gaps and are significantly populated. Figure 3 shows the population distribution among rotational levels in CO at 80 and 293K.

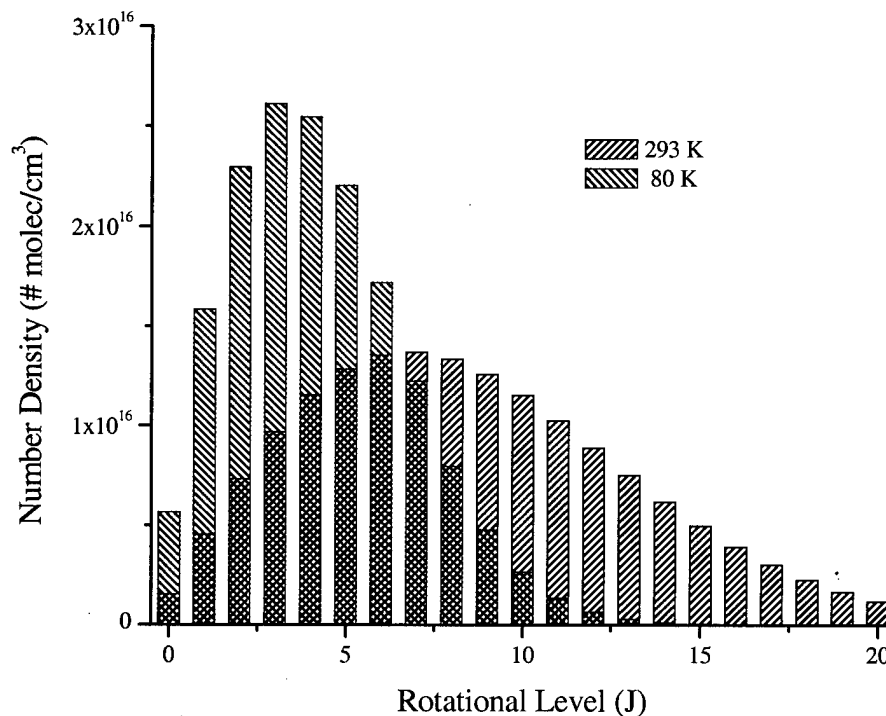


Figure 3. Boltzmann distributions. The number density in both plots is the same.

The average kinetic energy of the molecules can be calculated from the Maxwell distribution which predicts the fraction of molecules having a velocity between v_z and $v_z + dv_z$ along any axis (here the z-axis):

$$F(v_z) dv_z = \sqrt{\frac{m}{2\pi kT}} e^{-\frac{mv_z^2}{2kT}} dv_z. \quad (1.15)$$

Quantities such as the collision frequency v_c and the mean free path ℓ , given in Eq. (1.16), are based on the Maxwell distribution.

$$v_c = \rho (\pi d^2) \sqrt{\frac{16 kT}{m\pi}} \quad (1.16)$$

$$\ell = \frac{1}{\sqrt{2\rho (\pi d^2)}}$$

In Eq. (1.16), ρ is the gas number density and d is the molecule's hard sphere collision diameter. The hard sphere diameter for CO-CO collisions is 4 Å [20]. At 0.5 torr and 296K, the mean time between collisions ($1/v_c$) is 182 ns and the mean free path is 86 μm.

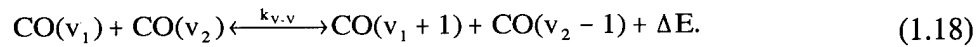
Molecular Energy Transfer and Collisions

Molecules exchange energy through collisions, and when a chemical reaction or optical excitation disturb the equilibrium distribution, collisions reestablish it. How fast collisions restore equilibrium depends on the energy transfer pathway. The slowest energy transfer pathway is Vibration-to-Translation or V-T relaxation. In V-T relaxation, a molecule expends vibrational energy increasing the separation speed of the collision partners or it converts kinetic energy into vibrational energy. Eq. (1.17) describes V-T relaxation.



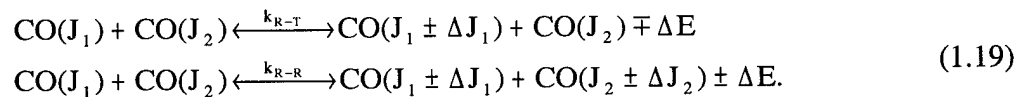
The rate constant k_{V-T} characterizes the efficiency of V-T relaxation. In CO k_{V-T} equals $3 \times 10^{-17} \text{ cm}^3 \text{ molecule}^{-1} \text{ sec}^{-1}$ [21], resulting in a V-T relaxation time of 2 s at a CO pressure of 0.5 torr.

A faster relaxation mechanism is Vibration-to-Vibration or V-V relaxation. In V-V relaxation, two vibrationally excited molecules collide and one molecule gives up its vibrational energy to the other as described in Eq. (1.18):



The k_{V-V} rate constants in CO have values on the order of $2 \times 10^{-12} \text{ cm}^3 \text{ molecule}^{-1} \text{ sec}^{-1}$. At a pressure of 0.5 torr, the V-V relaxation time is $\sim 20 \mu\text{s}$.

The fastest relaxation processes are Rotation-to-Translation (R-T) and Rotation-Rotation (R-R) relaxation. In R-T relaxation, a molecule changes J levels by absorbing or releasing kinetic energy. In R-R relaxation, both collision partners change J levels. Eq. (1.19) describes both processes.



The CO R-T and R-R rate constants equal $\sim 2 \times 10^{-11} \text{ cm}^3 \text{ molecule}^{-1} \text{ sec}^{-1}$. At 0.5 torr, the rotational relaxation time is $\sim 2 \mu\text{s}$.

Molecular Energy Transfer and Optical Transitions

While collisions are the dominant means of energy exchange, they are not the only means. Molecules also exchange energy by emitting or absorbing radiation, and given the proper conditions, radiation transfers energy faster than do collisions. This is especially true in low pressure systems where the mean time between collisions is longer than the radiative lifetime of the excited state or when the excited molecules are subject to a laser radiation field. Selection rules govern the vibrational, rotational, and m_J levels coupled by radiation.

For an ideal harmonic oscillator only $\Delta v = 1$ transitions are allowed. Because diatomic molecules only approximate harmonic oscillators, $\Delta v \geq 2$ transitions also occur though much less often. In CO, $\Delta v = 1$ transitions are ~ 100 times more likely than $\Delta v = 2$ transitions, and $\Delta v = 2$ transitions are ~ 100 times more likely than $\Delta v = 3$ transitions. The selection rule governing rotational levels is $\Delta J = \pm 1$ with an additional restriction that $\Delta m_J = 0$ or $\Delta m_J = \pm 1$ depending on the polarization of the radiation.

Spectroscopists identify radiative transitions between vibrational and rotational levels according to whether $\Delta J = 1$ or $\Delta J = -1$. The letter P is assigned to radiative transitions—absorbing or emitting—when the upper state J value is one less than the lower state J value. The particular transition is identified by including the lower state J value in parenthesis: $P(J_{\text{lower}})$. For example, a radiative transition between $v = 0, J = 7$ and $v = 1, J = 6$ is a $P(7)$ transition. The letter R is assigned to transitions whose upper state J value is one greater than the lower state value. The transition between $v = 0, J = 7$ and $v = 1, J = 8$ is an $R(7)$ transition. Table 3 gives the wavelengths in microns for the R and P $\Delta v = 1$ transitions among the first three vibrational levels in CO.

The Einstein A coefficient characterizes the likelihood of a radiative transition. Eq. (1.20) gives the A coefficient

$$A_{v_i, J_i}^{v_u, J_u} = \frac{64\pi(\Delta E_{v_i, J_i}^{v_u, J_u})^3}{3h^4 c^3} \frac{S_{v_i, J_i}^{v_u, J_u}}{2J_u + 1} |D_{v_i, J_i}^{v_u, J_u}|^2 \quad (1.20)$$

where $v_{u,l}$ and $J_{u,l}$ represent the upper and lower vibrational and rotational levels respectively. ΔE is the energy gap between states, S is the Hönl-London factor ($S = J_i$ for P and $J_i + 1$ for R transitions), and D is the transition dipole moment. Table 4 gives A coefficients based on the calculated dipole moment matrix elements from Ref [22].

THE CO LASER AND OPTICAL PUMPING

Electric discharge pumping made high-power CO lasers possible, but it also permitted the lasers to run at the longer wavelength absorbed by the atmosphere. When CO collides with the electrons in a discharge, the CO converts the electrons' kinetic

Table 3. $\Delta v = 1$ wavelengths in CO. All values are in 10^{-6} m.

Lower J	$v = 0$ to $v = 1$		$v = 1$ to $v = 2$		$v = 2$ to $v = 3$	
	R	P	R	P	R	P
0	4.6575	—	4.7157	—	4.7753	—
1	4.6493	4.6742	4.7074	4.7327	4.7669	4.7925
2	4.6412	4.6826	4.6992	4.7413	4.7585	4.8013
3	4.6333	4.6912	4.6911	4.7500	4.7503	4.8101
4	4.6254	4.7000	4.6832	4.7589	4.7422	4.8191
5	4.6177	4.7088	4.6753	4.7678	4.7342	4.8282
6	4.6100	4.7177	4.6675	4.7769	4.7263	4.8375
7	4.6024	4.7267	4.6598	4.7861	4.7185	4.8468
8	4.5950	4.7359	4.6523	4.7954	4.7109	4.8563
9	4.5876	4.7451	4.6448	4.8048	4.7033	4.8658
10	4.5804	4.7545	4.6375	4.8143	4.6958	4.8755
11	4.5732	4.7640	4.6302	4.8240	4.6885	4.8853
12	4.5662	4.7736	4.6230	4.8337	4.6812	4.8952
13	4.5592	4.7833	4.6160	4.8436	4.6740	4.9053
14	4.5524	4.7931	4.6090	4.8536	4.6670	4.9155
15	4.5456	4.8031	4.6022	4.8637	4.6600	4.9257
16	4.5389	4.8131	4.5954	4.8739	4.6532	4.9362
17	4.5324	4.8233	4.5888	4.8843	4.6464	4.9467
18	4.5259	4.8336	4.5822	4.8948	4.6398	4.9574
19	4.5195	4.8440	4.5757	4.9054	4.6332	4.9681
20	4.5132	4.8546	4.5694	4.9161	4.6268	4.9791
21	4.5071	4.8652	4.5631	4.9270	4.6204	4.9901
22	4.5010	4.8760	4.5569	4.9379	4.6142	5.0013
23	4.4950	4.8869	4.5509	4.9490	4.6080	5.0126
24	4.4891	4.8980	4.5449	4.9603	4.6020	5.0240
25	4.4833	4.9091	4.5390	4.9716	4.5960	5.0356
26	4.4775	4.9204	4.5332	4.9831	4.5901	5.0473
27	4.4719	4.9318	4.5275	4.9947	4.5844	5.0591
28	4.4664	4.9434	4.5219	5.0065	4.5787	5.0711
29	4.4609	4.9550	4.5164	5.0184	4.5731	5.0832
30	4.4556	4.9668	4.5110	5.0304	4.5677	5.0954

energy into molecular vibrational energy. vibrationally excited molecules are created so quickly that rapid V-V relaxation promotes many molecules into upper vibrational levels, preventing gain from building between the lower vibrational levels. Lasing between upper vibrational levels yields the longer wavelengths absorbed by the atmosphere whereas lasing between low-lying vibrational levels yields shorter wavelengths. Optical pumping is one way to build gain between lower vibrational levels faster than V-V relaxation destroys it [23] [24] [25]. With optical pumping, a laser pulse tuned to a

Table 4. Einstein A-Coefficients for $\Delta v = 1$ transitions. The values are for $^{12}\text{C}^{16}\text{O}$ in the electronic ground state. All values have units of s^{-1} .

Lower J	$v = 0$ to $v = 1$		$v = 1$ to $v = 2$		$v = 2$ to $v = 3$	
	R	P	R	P	R	P
0	11.99	–	23.07	–	33.25	–
1	14.47	35.58	27.84	68.45	40.12	98.67
2	15.59	23.59	29.99	45.38	43.22	65.41
3	16.26	21.11	31.27	40.61	45.06	58.54
4	16.71	19.99	32.15	38.46	46.33	55.44
5	17.06	19.32	32.82	37.18	47.29	53.59
6	17.34	18.86	33.35	36.29	48.06	52.31
7	17.58	18.51	33.81	35.62	48.72	51.34
8	17.79	18.23	34.21	35.07	49.29	50.56
9	17.97	17.98	34.57	34.61	49.80	49.89
10	18.15	17.77	34.89	34.20	50.27	49.31
11	18.30	17.58	35.19	33.83	50.70	48.78
12	18.45	17.41	35.48	33.50	51.11	48.29
13	18.59	17.24	35.75	33.18	51.49	47.84
14	18.73	17.09	36.01	32.88	51.86	47.41
15	18.86	16.94	36.25	32.60	52.22	47.01
16	18.98	16.80	36.49	32.33	52.56	46.61
17	19.10	16.66	36.72	32.07	52.89	46.23
18	19.22	16.53	36.95	31.81	53.21	45.87
19	19.34	16.40	37.17	31.56	53.52	45.51
20	19.45	16.27	37.38	31.32	53.83	45.16
21	19.56	16.15	37.59	31.08	54.12	44.81
22	19.67	16.02	37.80	30.84	54.42	44.47
23	19.77	15.90	38.00	30.61	54.71	44.14
24	19.88	15.78	38.20	30.38	54.99	43.81
25	19.98	15.67	38.39	30.15	55.27	43.48
26	20.08	15.55	38.58	29.93	55.54	43.16
27	20.18	15.43	38.77	29.71	55.81	42.84
28	20.28	15.32	38.96	29.49	56.07	42.52
29	20.38	15.21	39.14	29.27	56.33	42.20
30	20.47	15.09	39.33	29.05	56.59	41.89

CO resonance excites molecules from $v = 0$ into $v = 2$. Because the thermal population in $v = 1$ is negligible, the pulse immediately creates gain between $v = 2$ and $v = 1$ and the CO lasers in the atmospheric transmission window with a wavelength between 4.6 and 4.8 microns. Appendix A reports the results of a computer study investigating the scalability of an optically pumped CO laser.

Optical pumping can be efficient and scalable. In 1990 an optically-pumped ammonia gas laser produced 4.6-J pulses at 12 microns when pumped with 13-J pulses at 9 microns from a TEA CO₂ laser [26]. Whether an efficient, high-energy optically-pumped CO laser is possible depends on how much energy the pump couples into the CO.

Coupling large amounts of optical energy into CO is difficult for two reasons. First, CO has a narrow absorption linewidth: 300 MHz (FWHM) at room temperature and a pump wavelength of 2.35 μm . For CO to absorb the energy efficiently, the pump's frequency bandwidth must fall within the 300-MHz window. Only laser light has such a narrow bandwidth. Appendix B describes a narrow-band pump laser. The second problem is saturation. A high-energy pump saturates a transition by exciting half the ground-state molecules into the upper state. After saturation, the pump removes as much energy from the gas as it deposits. Saturation is evident mathematically in the equation describing photon absorption and emission [27]:

$$\frac{dn(z,t)}{dt} = \sigma(v) cn \left[N_u(z,t) - \frac{g_u}{g_l} N_l(z,t) \right] \\ \sigma(v) = \frac{A\lambda^2}{8\pi} S(v). \quad (1.21)$$

In Eq. (1.21), $N_{u,l}$ is the number density of molecules in the upper or lower energy level respectively; $g_{u,l}$ is the number of degenerate states in the upper or lower level; $n(z,t)$ is the number density of photons at position z and time t ; c is the speed of light; $\sigma(v)$ is the resonance absorption cross section; A is the Einstein coefficient; λ is the wavelength; $S(v)$ is the transition lineshape, and v is the transition frequency. Eq. (1.21) shows that the CO quits absorbing light ($dn/dt \approx 0$) when $N_u \approx \frac{g_u}{g_l} N_l$. To prevent saturation, a fast relaxation mechanism such as rotational relaxation can transfer molecules out of the upper state or replace molecules removed from the lower state.

Rotational relaxation's ability to prevent high energy pulses from saturating an absorption transition has already been demonstrated [28]. If fast enough, rotational relaxation allows a high energy pump pulse to invert the entire vibrational band instead of a single pair of rotational levels within the band. Eq. (1.22) gives the rate at which rotational relaxation changes the population in a rotational level

$$\frac{d N_i}{dt} = - \sum_{j=0(i \neq j)}^{\infty} k_{ij} N_i M + \sum_{j=0(i \neq j)}^{\infty} k_{ji} N_j M \quad (1.22)$$

where N_i represents the number density of molecules in level i , N_j represents the number density in any rotational level other than i , and M represents the number density of the collision partners. The first term on the right-hand side of Eq. (1.22) accounts for molecules leaving N_i while the second term accounts for molecules entering N_i . The rate constants k_{ji} and k_{ij} characterize the probability that a molecule leaves N_j and enters N_i and vice versa. The larger a transition's rate constant, the more likely the transition will occur.

The quantities most closely linked to the rate constants in Eq. (1.22) are the rotational level populations. Because the populations are interdependent, an individual rate constant cannot be measured in isolation. As a result, all experiments—some more than others—are limited to observing quantities whose values depend simultaneously on many rate constants [29].

PREVIOUS CO WORK

Early efforts at finding the rate constants relied on thermal conductivity or speed-of-sound measurements since both properties depend on RET [30]. Because molecules in a single rotational level could not be isolated, such measurements were insensitive to individual rate constants. Two other methods for studying rotational relaxation in CO suffer the same difficulty: terminal population studies in free jets and radiative transition linewidth measurements.

Free Jet Experiments

Free jet experiments rely on supersonic expansion to cool the gas and perturb the population distribution among rotational levels. After the gas passes through the supersonic nozzle, its translational temperature drops rapidly and collisions cannot immediately restore equilibrium between the rotational and translational temperatures. Rate constants can be deduced by measuring the extent to which the rotational populations reach equilibrium before collisions in the freely expanding gas stop.

Bassi [31] measured the terminal population distribution among rotational levels in CO with a tuneable IR diode laser and a bolometer. The work was conducted at low temperatures (<100 K) and only the few rotational levels populated at those temperatures ($J = 0 - 5$) were investigated. Ahern conducted a similar terminal population study [32]. Ahern measured the final populations by resonance-enhanced multi-photon ionization (REMPI). In REMPI a short wavelength laser pulse ionizes CO molecules in the jet. The rotational level populations are extracted from the ion signal. Belikov [1][33] and Sharafutdinov [34] monitored rotational population distributions at different points along a free jet using an electron beam. The electron beam ionizes CO molecules (N_2 in Sharafutdinov) in the jet, and fluorescence from the ions reveals the rotational level populations. In all these experiments the molecules remain in a near-equilibrium distribution. Without significant departures from equilibrium, distinguishing the contribution of one rate constant over another is difficult, and deciding which rate constant model best fits CO becomes problematic.

Linewidth Experiments

With tuneable diode lasers operating reliably in the near and mid IR spectrum, many studies have focused on CO's spectral properties such as line position, line strength, and linewidth [35]. Linewidth measurements reveal information about rotational relaxation [36][37][38][39] because rotational relaxation rates determine the state lifetimes. The many collisions that contribute to line broadening introduce contributions from all the rate constants. Consequently no subset of rate constants dominates, and the

linewidth data yields no conclusive preference for one model over another with one exception. At high pressures CO supports stimulated Raman scattering and, under the right conditions, the linewidth of the vibrational Q-branch Raman spectra narrows. In a Raman Q-branch transition, a molecule absorbs light from an incident beam and makes an R or P transition into an excited virtual level. The excited molecule emits light at the Raman wavelength and returns via a P or R transition to the rotational energy state it originally left, though in a vibrational level one up from the initial vibrational level. As collisions cause the narrowing in the Q-branch spectra, the narrowing is related to the rotational relaxation rate constants. Looney [38] found that the SPEG fitting law, restricted to $\Delta J = 2$ transitions, predicted the pressure at which Q-branch narrowing started while other fitting laws could not.

Pump-Probe or Double Resonance Experiments

An experiment sensitive to individual rate constants is the pump-probe or double resonance experiment. Figure 4 shows the basic elements of a pump-probe experiment. A pump laser excites molecules into an upper state. The excited molecules then amplify

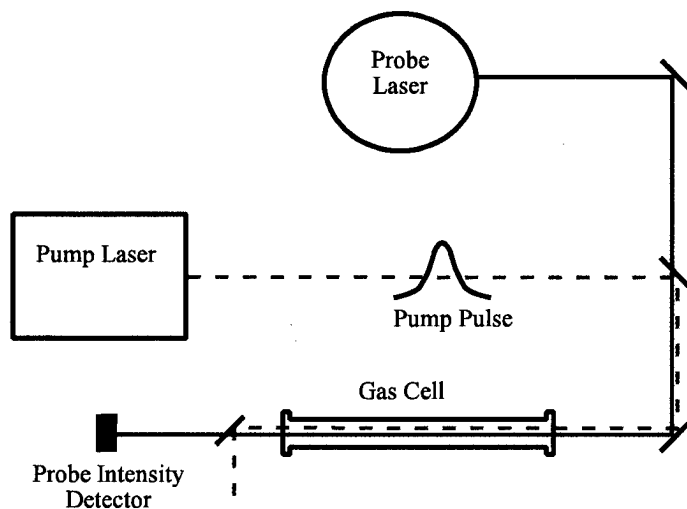


Figure 4. Basic pump-probe elements. The figure shows the elements of a laser pump-probe experiment. An ideal pump produces short pulses so pumping is complete before relaxation occurs; the ideal probe is cw to track the excited state population continuously.

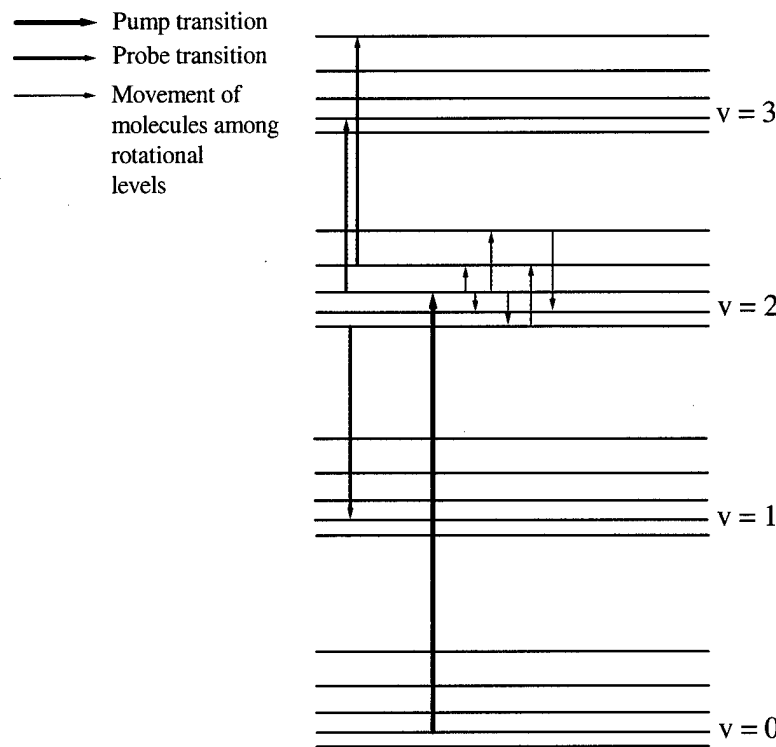


Figure 5. Energy level diagram showing pump-probe transitions.

or absorb light from a probe laser. A detector monitors the change in the probe laser's intensity caused by relaxation among the excited-state populations. Figure 5 shows an energy-level diagram of the experiment.

Laser pump-probe studies are sensitive to individual rate constants because the pump populates a single rotational level and rate constants linked to the pumped level dominate the initial population changes. Figure 6 shows the excited-state population distribution immediately following the pump and after rotational relaxation is complete.

Researchers have conducted pump-probe experiments on several diatomic molecules specifically to measure rotational relaxation rates. Sitz and Farrow [40] studied $N_2(v=1, J=0-14)$ using stimulated Q-branch Raman pulses as a pump and UV REMPI pulses as a probe. Sudbo and Loy conducted a similar experiment on NO using infrared pulses from an F-center laser as the pump and UV REMPI pulses as the probe

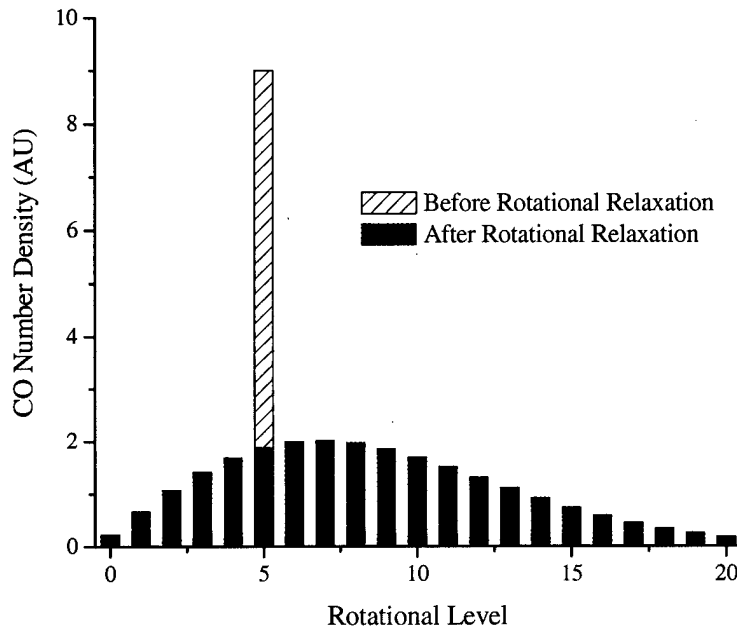


Figure 6. Post-pump population distribution. The bars show the population distributions before and after rotational relaxation.

[41]. Copeland and Crim studied HF [42] and Muyskens and Crim studied DF [43]. The HF/DF studies used pulsed HF/DF lasers as the pump and cw HF/DF lasers as the probe. In all these experiments, unambiguous state-to-state RR rate constants were derived.

Despite their suitability for determining rate constants, researchers have performed only a handful of pump-probe experiments on CO [44][45]. Brechignac used a pulsed CO laser as the pump ($v=0 \rightarrow 1$) and a second cw CO laser as a probe ($v=1 \rightarrow 2$). Because only a small group of rotational levels around $J = 10$ were investigated, Brechignac's experiments did not provide a full complement of rate constants.

COMPLICATIONS WITH PUMP-PROBE EXPERIMENTS

Extracting rate constant values from pump-probe data requires accounting for vibrational losses, unwanted optical transitions, and anisotropic velocity and angular momentum distributions.

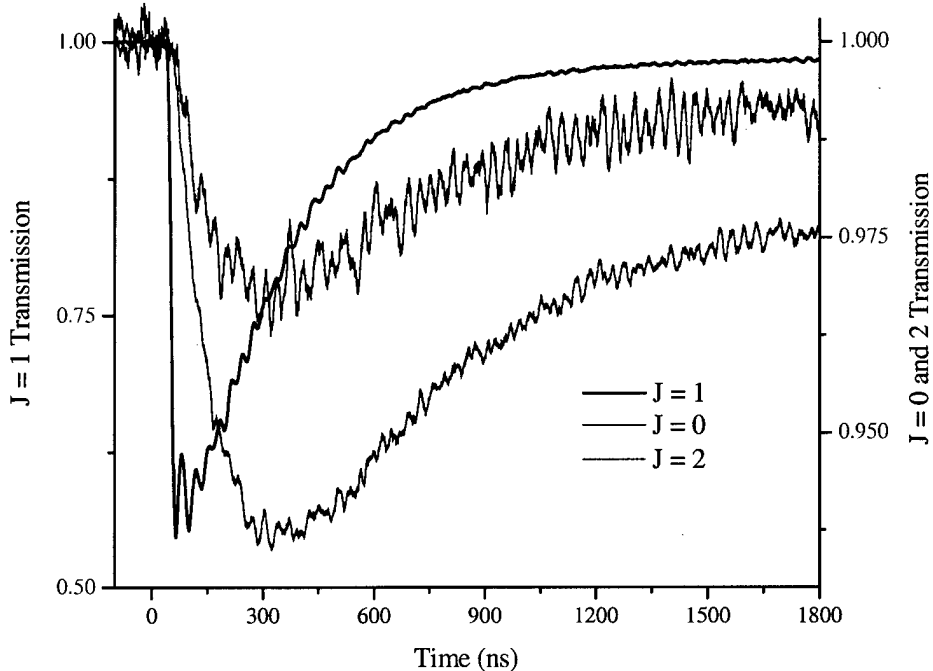


Figure 7. Probe transmission vs. time. The curves show the probe transmission fraction with 0.3 torr of room temperature CO. The R(0) pump populates the CO($v=2$, $J=1$) level. The probe monitors the $J = 0, 1$, and 2 populations using R(0), R(1), and R(2) transitions between $v = 2$ and $v = 3$.

Collision Losses from CO($v=2$)

Figure 7 shows a sample of probe transmission data. An R0 pump initially populates the $v=2, J=1$ level as indicated by the almost instantaneous 40% drop in the $J_{R0} = 1$ probe transmission (the subscript indicates the pump transition). Transmission recovers as molecules relax out of $J_{R0} = 1$ into adjacent levels. The probes of $J_{R0} = 0$ and $J_{R0} = 2$ show molecules entering and leaving those levels. All three J level populations reach steady state values after ~ 1600 ns showing that rotational relaxation is complete. V-V and V-T relaxation out of the $v = 2$ causes the gradual rise in transmission after 1600 ns. Figure 7 makes it clear vibrational loss is slow compared with the rate of rotational relaxation. Eq. (1.23) describes the rate of population change in $v = 2$ where N_v represents the total population in vibrational level v :

$$\frac{dN_2}{dt} = -k_{\text{loss}} N_2 M + k_{02} N_0 M + k_{12} N_1 M + k_{32} N_3 M + \dots \quad (1.23)$$

N_0 and N_1 contribute negligibly to N_2 because the energy gap between vibrational levels is large compared to kT . Vibrational levels above $v = 2$ do not contribute because they are initially unpopulated and because few molecules leave and re-enter $v = 2$ before CO reaches rotational equilibrium. Without the contributing terms, Eq. (1.23) has an exponential decay solution:

$$\begin{aligned} \frac{dN_2}{dt} &= -k_{\text{loss}} N_2 M \\ N_2(t) &= N_2(0) e^{-k_{\text{loss}} M t} \end{aligned} \quad (1.24)$$

Optical Losses and CO($v=2$)

Optical pumping experiments conducted at Air Force Research Laboratory (AFRL) found that the 2.3-micron pump produced a strong 4.7-micron pulse that exited the CO almost simultaneously with the pump. The 4.7-micron pulse was amplified spontaneous emission (ASE). ASE leaches energy from the excited CO as fast as the pump deposits it. Such rapid radiative loss drastically alters the population of the pumped rotational level. ASE takes place between the $v = 2$ and $v = 1$ vibrational levels or between rotational levels within the pumped vibrational level [43]. Increasing the pump diameter reduces the gain, making ASE less likely.

Expanding the pump beam to avoid ASE prevents coherent effects such as self-induced transparency (SIT). SIT would reduce the number of molecules the pump pulse excites. Appendix C reviews coherence and the pump-probe experiment.

Anisotropic Velocity Distribution

Assuming the 5.7-ns pump pulse has a Gaussian temporal profile (see Figure 3.3), the transform-limited spectral bandwidth is 109 MHz FWHM. As the pump profile is not perfectly Gaussian, a Fourier transform of the pump's electric field (derived from the intensity profile) predicts a 149-MHz bandwidth. Measurements of the excited-state CO

absorption bandwidth immediately following the pump pulse suggest the pump's actual bandwidth is 165 MHz. At a pump wavelength of 2.35 microns, the FWHM Doppler bandwidth of CO at 296 K is 297 MHz. The pump's sub-Doppler bandwidth creates an anisotropic velocity distribution in the excited state, giving the excited molecules a narrower linewidth than the gas temperature will support. As collisions reestablish a thermal velocity distribution, the linewidth of the excited molecules broadens, causing the probe transmission to increase.

Angular Momentum Reorientation

When the linearly polarized pump passes through the CO, it preferentially excites ground state molecules whose bond axes lie in the plane of polarization. Because the molecules retain their original angular momentum direction during excitation, the excited state population is optimally aligned to absorb a probe with a polarization parallel to that of the pump. On the other hand, the aligned molecules would poorly absorb a probe polarized perpendicular to the pump. Until collisions randomize the sublevel populations, the difference in probe absorption with polarization must be accounted for.

CHAPTER 2: J-LEVEL POPULATIONS AND THEORY

The rotational relaxation rate constants are determined by matching the predicted and measured speed at which the rotational populations return to equilibrium. The first step in comparing measurement with theory is to extract the populations from the probe absorption data.

ROTATIONAL POPULATIONS: EXPERIMENTAL

In pump-probe double resonance experiments, changes in probe intensity reveal changes in level populations. Beer's law relates the populations to the intensity:

$$\ln\left[\frac{I(y,t)}{I(0,0)}\right] = \sum_m \sum_{m'} \sigma_{j,j'}(m, m', v, t) [N'_{v',j',m'}(t) - N_{v,j,m}(t)] y. \quad (2.1a)$$

In Eq. (2.1a), $I(y,t)$ is the probe intensity at position y and time t where the beam propagates in the y direction, $\sigma_{j,j'}(m, m', v, t)$ is the absorption cross section between the lower (v, j, m) and upper (v', j', m') states, and $N_{v,j,m}(t)$ is the population in magnetic sublevel m of rotational level j in vibrational level v . Eq. (2.1a) can be simplified by noting the upper state population N' remained negligible throughout the experiment. Additionally, if the polarization direction of the linearly-polarized pump defines the z -axis, the transitions induced by the pump obey the $\Delta m = 0$ selection rule such that $m' = m$. With these assumptions, Eq. (2.1a) becomes

$$\ln\left[\frac{I(y,t)}{I(0,0)}\right] \approx -y \sum_m \sigma_{j,j'}(m, v, t) N_{v,j,m}(t). \quad (2.1b)$$

Factoring the m -dependence out of $\sigma_{j,j'}(m, v, t)$ with the term $\alpha_{j',j}(m)$ leaves the expression for the cross section given in Eq. (1.21):

$$\ln\left[\frac{I(y,t)}{I(0,0)}\right] = -\frac{A\lambda^2}{8\pi} S(v, t) y \sum_m \alpha_{j',j}(m) N_{v,j,m}(t). \quad (2.1c)$$

In Eq. (2.1c), $S(v,t)$ is the lineshape and the α factors are combinations of the Clebsch-Gordan coefficients described later in the chapter. With the path length of the probe through the CO fixed at L , $I(y,t)$ becomes $I(L,t) = I(t)$:

$$-\frac{8\pi}{A\lambda^2 L} \ln \left[\frac{I(t)}{I(0)} \right] = S(v,t) \sum_m \alpha_{j,j'}(m) N_{v,j,m}(t). \quad (2.1d)$$

The right-hand side of Eq. (2.1d) includes effects unrelated to rotational relaxation: vibrational relaxation, lineshape relaxation, and magnetic sublevel alignment.

Vibrational Relaxation

Eq. (1.24) describes vibrational relaxation. Because the energy gap between vibrational levels is ten times greater than the energy gaps between appreciably populated rotational levels, differences in rotational energy are inconsequential during vibrational relaxation. As a result, relaxation out of the vibrational level as a whole describes vibrational relaxation out of individual rotational levels. Using Eq. (1.24) to express the time dependence of the population in vibrational level v where $N_{v,j,m}(t) = N_{j,m}(t) e^{-k_{loss}Mt}$, Eq. (2.1d) becomes

$$-\frac{1}{e^{-k_{loss}Mt}} \frac{8\pi}{A\lambda^2 L} \ln \left[\frac{I(t)}{I(0)} \right] = S(v,t) \sum_m \alpha_{j,j'}(m) N_{j,m}(t) \quad (2.2)$$

In Eq. (2.2), k_{loss} is the rate constant for losses out of $v = 2$ and M is the total CO number density.

Time-Dependent Velocity Distribution and Lineshape

At low gas pressures, the Doppler shift determines a molecule's frequency response. Eq. (2.3) gives CO's FWHM Doppler line width

$$\Delta v_D = \sqrt{\frac{8kT \ln 2}{m_{CO} c^2}} v_0 \quad (2.3)$$

where m_{CO} is a CO molecule's mass and v_0 is the line-center transition frequency. CO's Doppler width at room temperature and a pump wavelength of 2.35 microns is 300 MHz. Light with a bandwidth narrower than Δv_D excites molecules whose velocity projection on the y-axis is narrower than one would predict based on the Maxwell distribution. If the pump is also tuned off line-center resonance, the excited molecules' average velocity will be offset from $v_y = 0$. In the discussion that follows the pump is assumed to be on line center.

A pump with a sub-Doppler bandwidth complicates the rotational population measurement because the lineshape changes as the velocity directions relax to a Maxwell distribution. This is especially true if the probe laser also has a sub-Doppler bandwidth¹. Eq. (2.4) gives an expression for the lineshape that accounts for a time-dependent linewidth:

$$S(v, t) = \frac{1}{\Delta v(t)} \sqrt{\frac{4 \ln 2}{\pi}} e^{-\frac{-4 \ln 2 (v - v_0)^2}{\Delta v(t)^2}}. \quad (2.4)$$

While the molecules' lineshape is Gaussian once the gas reaches equilibrium, a Gaussian only approximates the excited-state line shape immediately after the pump. However given the noise in the lineshape measurement, Eq. (2.4) represents $S(v, t)$ as well as any other peaked function. Using Eq. (2.4), Eq. (2.2) becomes

$$-\frac{1}{e^{-k_{loss} M t}} \frac{1}{S(v, t)} \frac{8\pi}{A \lambda^2 L} \ln \left[\frac{I(t)}{I(0)} \right] = \sum_m \alpha_{J', J}(m) N_{J, m}(t) \quad (2.5)$$

leaving only $\alpha_{J', J}(m)$ to contend with.

Angular Momentum Reorientation

At thermal equilibrium, the magnetic sublevels are equally populated:

$$N_{J, m}(t) = \frac{N_J}{2J + 1}. \quad (2.6)$$

¹The manufacturer claims that the diode laser has a bandwidth of 30 MHz or less, including current jitter in the controller.

Inserting Eq. (2.6) into Eq. (2.5) yields

$$\sum_m \alpha_{J,J'}(m) N_{J,m}(t) = \frac{N_J(t)}{2J+1} \sum_m \alpha_{J,J'}(m) = \frac{2J'+1}{2J+1} N_J(t) \quad (2.7)$$

where the sum over the α factors yields the degeneracy of the upper state. The result is the more familiar form of Beer's law with degeneracy factors $g_u = 2J'+1$ and $g_l = 2J+1$:

$$-\frac{1}{e^{-k_{loss}M_t}} \frac{1}{S(v,t)} \frac{8\pi}{A\lambda^2 L} \ln \left[\frac{I(t)}{I(0)} \right] = \frac{g_u}{g_l} N_J(t). \quad (2.8)$$

Eq. (2.8) describes pump absorption because the molecules are evenly distributed among the magnetic sublevels. It also describes probe absorption after the excited molecules reach equilibrium. It does not describe probe absorption immediately after the pump. To do so, one must return to Eq. (2.5).

Eq. (2.5) applies when the population distribution among the magnetic sublevels is non-uniform. A simple way to create a non-uniform distribution is with linearly polarized light. The light's dipole field interacts with a molecule's dipole moment directed along the bond axis. When the bond axis and field polarization are in the same plane, the interaction is strongest. Since in diatomic molecules the bond axis is perpendicular to the angular momentum, this is equivalent to saying that molecules with no angular momentum projection along the quantization axis² ($m = 0$) are most likely to absorb the pump. Likewise molecules with projections of $m = \pm J$ are least likely to absorb the pump. Molecules respond to the linearly polarized probe in the same way. When the pump and probe polarizations are parallel, the pump fills the sublevels most likely to absorb the probe. When the polarizations are perpendicular, the pump fills the sublevels least likely to absorb the probe. At an angle between, one expects the sublevel populations and probe absorption probabilities to balance so that the excited molecules absorb the probe as if the pump had populated the sublevels uniformly.

²The field polarization direction defines the quantization axis.

These physical arguments can be stated mathematically using either the coupled or uncoupled angular momentum representation. Before absorption, the magnitudes of the molecule's and photon's angular momenta and their projections along the quantization axis are known, making the uncoupled representation most appropriate:

$$|j_1 m_1\rangle |j_2 m_2\rangle = |j_1 m_1, j_2 m_2\rangle. \quad (2.9)$$

In Eq. (2.9), $\{j_1 m_1\}$ and $\{j_2 m_2\}$ are the quantum numbers for the molecule and photon respectively. The coupled representation best describes the molecule-photon system after absorption

$$|j_1 j_2, j_3 m_3\rangle = |j_3 m_3\rangle \quad (2.10)$$

where $\{j_3 m_3\}$ describe the molecule's final state. By expressing the unknown state $\{j_3 m_3\}$ in terms of the known states $\{j_1 m_1\}$ and $\{j_2 m_2\}$, one can predict how the pump populates the excited-state sublevels. The identity operator \mathbf{I} links the two representations

$$\begin{aligned} |j_3 m_3\rangle &= \mathbf{I} |j_3 m_3\rangle = \left[\sum_{m_1, m_2} |j_1 m_1, j_2 m_2\rangle \langle j_1 m_1, j_2 m_2| \right] |j_3 m_3\rangle \\ &= \sum_{m_1, m_2} \langle j_1 m_1, j_2 m_2 | j_3 m_3 \rangle |j_1 m_1, j_2 m_2\rangle \end{aligned} \quad (2.11)$$

where $\langle j_1 m_1, j_2 m_2 | j_3 m_3 \rangle$ are Clebsch-Gordan coefficients whose square magnitudes are proportional to the probability that a ground state molecule in sublevel m_1 enters the excited state sublevel m_3 after absorbing a photon with orientation m_2 . For a linearly polarized dipole field whose polarization direction defines the z quantization axis, $j_2 = 1$ and $m_2 = 0$. Because Clebsch-Gordan coefficients equal zero when $m_1 + m_2 \neq m_3$, $m_2 = 0$ implies $m_1 = m_3$ resulting in the $\Delta m = 0$ selection rule for linearly polarized light. Expressions for the Clebsch-Gordan coefficients are readily available [46].

The α factor in Eq. (2.5) can be defined in terms of the Clebsch-Gordan coefficients:

$$\begin{aligned}\alpha_{//}^R(m_1) &= 3 \langle j_1 m_1, 10 | j_1 + 1 m_1 \rangle^2 = 3 \left[\frac{(j_1 + 1)^2 - m_1^2}{(j_1 + 1)(2j_1 + 1)} \right] \\ \alpha_{//}^P(m_1) &= 3 \langle j_1 m_1, 10 | j_1 - 1 m_1 \rangle^2 = 3 \left[\frac{j_1^2 - m_1^2}{j_1(2j_1 + 1)} \right]\end{aligned}\quad (2.12)$$

The R and P superscripts represent R and P transitions. The // subscript indicates the probe field polarization and quantization axis are parallel. Linearly polarized light whose polarization is perpendicular to the quantization axis must be described as the sum of left and right-circularly polarized fields. Circularly polarized dipole fields have j_2 and m_2 values of 1 and ± 1 respectively. Eq. (2.13) gives the α factors for probe light polarized perpendicular to the quantization axis.

$$\begin{aligned}\alpha_{\perp}^R(m_1) &= \left(\frac{3}{2} \right) \left[\langle j_1 m_1, 11 | j_1 + 1 m_1 - 1 \rangle^2 + \langle j_1 m_1, 1 - 1 | j_1 + 1 m_1 + 1 \rangle^2 \right] \\ &= \left(\frac{3}{2} \right) \left[\frac{(j_1 + m)(j_1 + m + 1)}{2(j_1 + 1)(2j_1 + 1)} + \frac{(j_1 - m)(j_1 - m + 1)}{2(j_1 + 1)(2j_1 + 1)} \right] \\ \alpha_{\perp}^P(m_1) &= \left(\frac{3}{2} \right) \left[\langle j_1 m_1, 11 | j_1 - 1 m_1 + 1 \rangle^2 + \langle j_1 m_1, 1 - 1 | j_1 - 1 m_1 - 1 \rangle^2 \right] \\ &= \left(\frac{3}{2} \right) \left[\frac{(j_1 - m)(j_1 - m - 1)}{2j_1(2j_1 + 1)} + \frac{(j_1 + m)(j_1 + m - 1)}{2j_1(2j_1 + 1)} \right]\end{aligned}\quad (2.13)$$

Figure 8 shows the predicted population fractions in each sublevel after an R6 pump based on the expressions in Eqs. (2.12) and (2.13). If the pump polarization makes

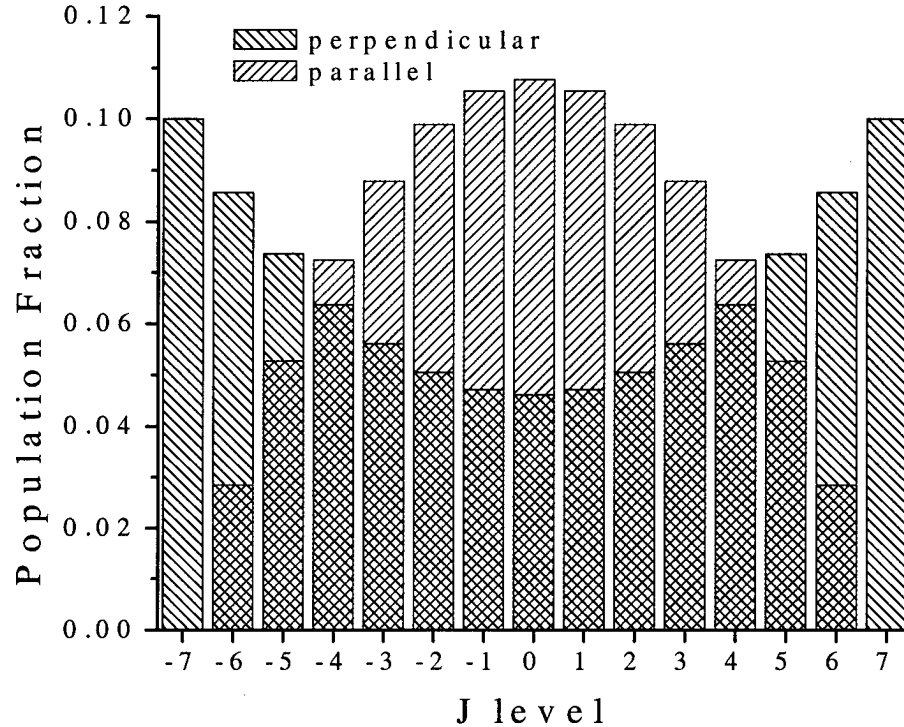


Figure 8. Post-pump sublevel populations. The figure shows the sublevels populated by an R6 pump when the pump polarization is perpendicular or parallel to the quantization axis.

an angle θ with the quantization axis, one can break the pump into parallel and perpendicular components using Eqs. (2.12) and (2.13) to define a θ -dependent α factor:

$$\alpha_{\theta}^{R,P}(m_1) = \alpha_{//}^{R,P}(m_1) \cos^2(\theta) + \alpha_{\perp}^{R,P}(m_1) \sin^2(\theta)$$

$$\alpha_{\theta}^R(m_1) = \frac{2j_1 + 3}{2j_1 + 1} + \frac{j_1^2 + j_1 - 3m_1^2}{(j_1 + 1)(2j_1 + 1)} \cdot \left[\frac{3\cos^2(\theta) - 1}{2} \right] \quad (2.14)$$

$$\alpha_{\theta}^P(m_1) = \frac{2j_1 - 1}{2j_1 + 1} + \frac{j_1^2 + j_1 - 3m_1^2}{j_1(2j_1 + 1)} \cdot \left[\frac{3\cos^2(\theta) - 1}{2} \right]$$

Eq. (2.14) shows that when $\theta = 57.4^\circ$ the m-dependence of the α factors disappears. From the probe's perspective, the linearly polarized pump populates the sublevels equally. The angle 57.4° is called the magic angle. Zare derives the magic angle in terms of rotation operators and spherical harmonics in application five of his text [46]. Setting the pump and probe polarizations at the magic angle avoids the probe's sensitivity to the aligned m-sublevel distribution created by the linearly polarized pump. For the magic angle case, Eq. (2.8) accurately describes probe absorption and the time-dependent J level population is given by

$$N_J(t) = \frac{1}{e^{-k_{loss}Mt}} \frac{1}{S(v,t)} \frac{8\pi}{A\lambda^2 L} \frac{g_J}{g_u} \ln \left[\frac{I(0)}{I(t)} \right]. \quad (2.15)$$

ROTATIONAL POPULATIONS: THEORETICAL

Eq. (1.22) describes how the rotational levels change with time. No mention of vibrational level is made in Eq. (1.22) because CO's rotational relaxation rate constants vary little with vibrational energy [36]. Eq. (1.22) also omits the internal energy states of the collision partner M. This is equivalent to assuming M represents an atomic rather than a molecular collision partner. In a pure CO sample, all collisions are between molecules and one might expect Eq. (1.22) to inadequately describe rotational relaxation. However, the literature states molecule-molecule collisions in CO are sufficiently accounted for by the simpler molecule-atom theory [39].

In room-temperature CO, more than fifteen rotational levels are significantly populated. With so many levels to track, Eq. (1.22) must be solved numerically. The adjustable parameters in Eq. (1.22) specific to CO are the rate constants. Unfortunately, associated with n rotational levels are $n(n-1)$ rate constants. The number of rate constants can be halved by invoking detailed balance. According to detailed balance the forward and reverse rate constants are related:

$$k_{ji} = \frac{g_i}{g_j} e^{-(E_i - E_j)/kT} k_{ij} \quad (2.16)$$

In Eq. (2.16), k_{ij} is the rate constant for molecules leaving i and entering j , and g_{ij} and E_{ij} are the degeneracy and energy values of levels i and j respectively. Modeling room-temperature CO requires tracking at least the first 15 rotational levels which, even after detailed balance, leaves 105 rate constants. Collecting enough data to justify a model with 105 variable parameters is difficult. Instead the more common approach is to construct a model for the rate constants with only a few parameters.

Rate Constant Models

Rate constant models originate in theoretical calculations, theory-based scaling laws, or empirical fits to data. Theoretical calculations based on intermolecular potentials have been made for CO-He, CO-H, and CO-H₂ systems [10][47]. While first-principle calculations provide a means for testing the underlying physics, they do not predict measured values well [48]. Simpler models called scaling laws maintain a basis in theory while using fits to data.

By assuming a collision occurs instantaneously so that a colliding molecule does not rotate during the collision, the Schrödinger equation can be solved approximately to derive a rate constant expression known as the infinite-order-sudden (IOS) scaling law [48]. Corrections to the IOS law allowing for rotation during the collision result in the energy-corrected-sudden (ECS) scaling law. Though strictly applicable only to molecule-atom collisions, the ECS law has been applied to CO-CO collisions with some success [39]. Eq. (2.17) gives the ECS rate constant with the condition that $i < j$:

$$k_{ij}^{ECS} = (2j+1) e^{(E_i - E_j)/kT} \Omega_j^2 \times \sum_{l=|i-j|}^{i+j} \begin{pmatrix} i & j & l \\ 0 & 0 & 0 \end{pmatrix}^2 (2l+1) \frac{k_{0l}}{\Omega_l^2}. \quad (2.17a)$$

In Eq. (2.17a) Ω_j is the adiabatic factor given by

$$\Omega_j = \left(1 + \frac{\omega_{j,j-1}^2 l_c^2}{24u^2} \right)^{-1}, \quad \omega_{j,j-1} = \frac{E_j - E_{j-1}}{\hbar} \quad (2.17b)$$

where l_c is the characteristic interaction length and u is the average relative velocity given by

$$u = \sqrt{\frac{8kT}{(m/2)\pi}}. \quad (2.17c)$$

The adiabatic factor Ω_j corrects the IOS law by allowing for the molecule to rotate during the interaction. The variable parameter within Ω_j is the interaction length l_c . The larger the interaction length, the more time the molecule has to rotate during the collision. When $l_c = 0$ there is no time for rotation and the IOS law is recovered. The value of l_c is small for molecules that interact only through short-range forces and larger for molecules that interact through long-range forces.

The $(\cdot \cdot \cdot)$ term in Eq. (2.17a) is a 3-j symbol used to ensure the conservation of angular momentum. The bottom row of zeros in the 3-j symbol implies that collisions which change a molecule's angular momentum occur in the molecule's plane of rotation.

The final terms in Eq. (2.17a) are the basis rate constant k_{0l} . A common formula for the basis rate constants is given in Eq. (2.17d)

$$k_{0l} = \frac{a}{[l(l+1)]^c} e^{-bE_l/kT} \quad (2.17d)$$

where l is an integer corresponding to a possible J value of the molecule's final state. With the expression in Eq. (2.17d), the model in Eq. (2.17a) is called the ECS-EP law. The variable parameters in the ECS-EP law are (a, b, c, l_c) .

While the ECS law is based on assumptions about the dynamics of a collision, other rate constant models are based on statistical considerations related to the exchange of energy between rotational and translational degrees of freedom. Eq. (2.18) gives the general form for the statistically-based fitting laws.

$$k_{ij} = F(\Delta E) R(\Delta E) N_\lambda(j_i, j_f) H(\Delta E) \quad (2.18)$$

In Eq. (2.18), ΔE is the energy gap between level i and j ; $F(\Delta E)$ is functional form of the rate constant's energy dependence; $R(\Delta E)$ is the translational phase space factor [48]; N_λ is the statistical factor; and H is the homonuclear propensity factor.

The fitting laws differ mainly in how they treat the energy gap ΔE between rotational levels. Table 5 shows the form of $F(\Delta E)$ for the statistical power gap (SPG), modified exponential gap (MEG), and statistical power-exponential gap (SPEG) laws. The translational phase space factor $R(\Delta E)$ accounts for the change in the density of translational states caused by the gain or loss of kinetic energy during rotational relaxation [42]. At room temperature, the change in the kinetic energy during a collision is small compared with the total kinetic energy, making it reasonable to set $R(\Delta E)$ equal to one [49]. The value of the statistical factor N_λ depends on whether collisions transferring rotational energy preserve or re-orient a molecule's magnetic sublevel m . Eq. (2.19) gives a general expression for N_λ

$$N_\lambda(j_i, j_f) = \frac{(2n_2 + 1)(2n_3 + 1) - \alpha(\alpha + 1)}{2j_i + 1} , \quad \alpha = 0 \text{ or } n_2 + n_3 - n_1. \quad (2.19)$$

where of the three values (j_i, j_f, λ) , n_1 is the largest, n_3 is the smallest, and n_2 is the middle value. The variable α is the greater of zero or $n_2 + n_3 - n_1$. Setting $\lambda = \infty$ assumes the

Table 5. Fitting laws. The table shows the energy dependence of the fitting laws.

Model	Parameters	$F(\Delta E)$	Comments
SPG	a,b	$a \cdot \left \frac{\Delta E}{B_v} \right ^{-b}$	$B_v = B_2$ the rotational constant. See Eq. (1.10)
MEG	a,b,c	$a \cdot \left(\frac{1 + \frac{AE_i}{kT} \cdot b}{1 + \frac{AE_i}{kT}} \right)^2 e^{-c \frac{\Delta E}{kT}}$	$A = 2$ [38],[51] E_i = Energy in initial state
SPEG	a,b,c	$a \cdot \left \frac{\Delta E}{B_v} \right ^{-b} \cdot e^{-c \frac{\Delta E}{kT}}$	$B_v = B_2$ the rotational constant. See Eq. (1.10)

collisions randomize m , while setting $\lambda = 0$ assumes the collisions preserve m . Intermediate values of λ allow for varying degrees of m preservation. Using Eq. (2.16) to define the reverse rate constants, the terms in Eq. (2.19) are limited to cases where j_i is less than j_f so that $N_\lambda = 1$ for $\lambda = 0$ and $2j_f + 1$ for $\lambda = \infty$. Because the data showed RET events tended to preserve the molecules' orientation (see Fig. 47), λ was set to zero during the model fitting detailed in Chapter 4.

The factor H in Eq. (2.18) accounts for the propensity of near-homonuclear molecules to undergo even- ΔJ transitions more often than odd- ΔJ transitions [50]. A tendency toward even- ΔJ transitions is related to the selection rule in homonuclear molecules restricting transitions to even values of ΔJ . The restriction originates from symmetry in the intermolecular potential $V(r, \theta)$ of homonuclear molecules where r and θ are defined in Figure 9. In terms of a Legendre polynomial expansion, $V(r, \theta)$ becomes

$$V(r, \theta) = \sum_s V_s(r) P_s(\cos\theta) \quad (2.20)$$

where $V_s(r)$ are functions of r only and $P_s(\cos\theta)$ are the Legendre polynomials. With a diatomic molecule composed of identical atoms, the potential must be symmetric about $\theta = \pi/2$, restricting the expansion to even s values. Without odd terms in the potential odd ΔJ transfer events cannot occur. At large r values, the distinction between a nearly-homonuclear molecule's atoms blurs and one expects the molecule to behave much like homonuclear molecule. For short-range interactions the difference between atoms is more apparent and the potential becomes much less symmetric so that homonuclear

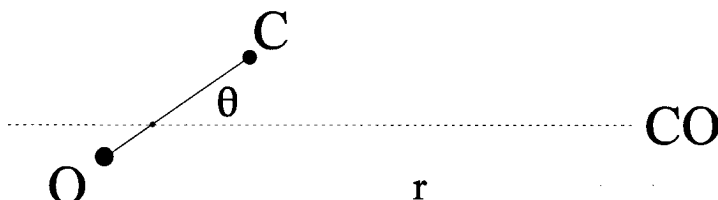


Figure 9. Intermolecular potential variables. The variables describing the intermolecular potential $V(R, \theta)$.

propensity disappears. Homonuclear propensity has been discussed in the CO literature [51] but never directly observed. Hints of it are evident in Bréchignac's CO double resonance experiments [45, Table 6], and Looney et. al. [38] found that restricting the rate constant models to even transitions in ΔJ gave the best fit to their linewidth data.

An empirical expression for H is given in Eq. (2.21)

$$H = 1 - \frac{d}{2} \sqrt{\frac{B_v}{\Delta E}} [1 - (-1)^{j_i + j_r}] \quad (2.21)$$

where d is a variable parameter and B_v is the rotational energy constant [52]. Without the square-root term in Eq. (2.21), H reduces the odd- ΔJ rate constants by a factor of $(1-d)$. The square-root term lessens the effect of homonuclear propensity with increasing transition energy gap increases, a trend visible in the data.

CHAPTER 3: EQUIPMENT AND PROCEDURES

This chapter describes the equipment used during the pump-probe experiment. It also presents the results of the tests done to ensure the equipment was operating properly. Figure 10 identifies the experiment's major components: the pump and probe lasers. The pump is a pulsed, narrowband, tuneable optical parametric oscillator (OPO) and the probe is a cw, narrowband, tuneable lead-salt diode laser.

THE OPO

The OPO was built under contract with the USAF by Dr. Andrew W. J. Brown of the Seattle-based Aculight Corporation. It provided 6-ns, 4-mJ pulses tuneable between 2.29 and 2.44 microns. For detailed information about the OPO, see Appendix D. Figure 11 depicts the OPO's components.

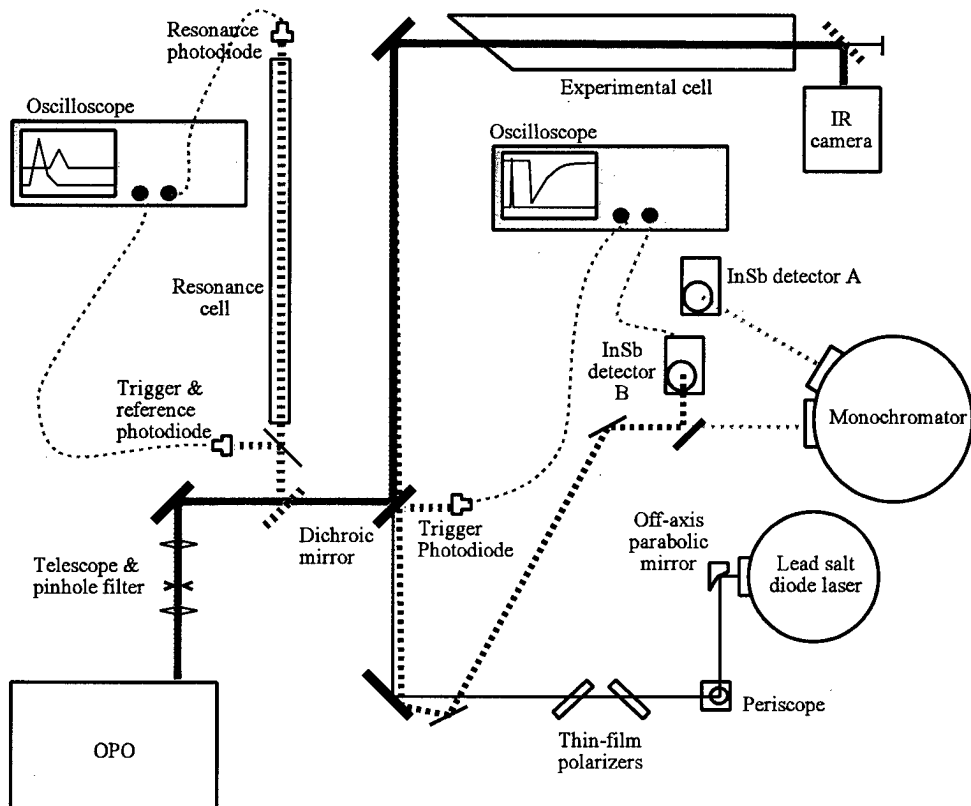


Figure 10. The experiments major components. The red line is the $2.3 \mu\text{m}$ pump. The blue line is the outgoing $4.7 \mu\text{m}$ probe. The dotted blue line is the returning probe beam.

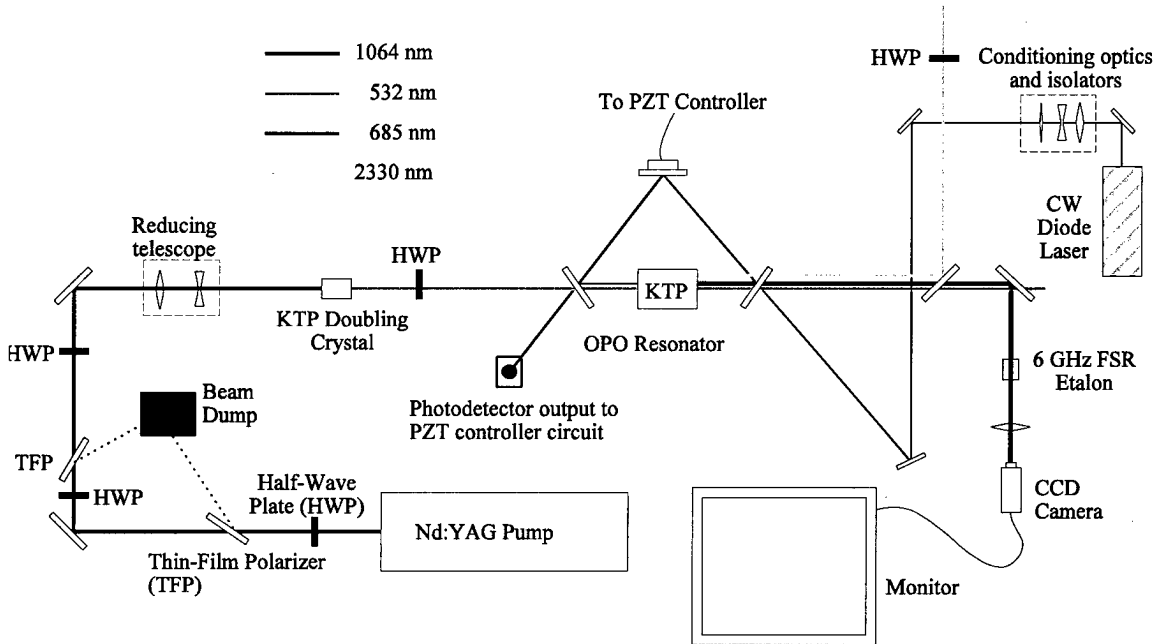


Figure 11. The Optical Parametric Oscillator (OPO).

Nd:YAG Laser

The energy source for the OPO is a Q-switched, injection-seeded Nd:YAG laser (Spectra-Physics Model GCR 170-10) that emits 700-mJ pulses at 10 Hz at a fixed wavelength of 1064 nm. Injection seeding forces the laser to operate on a single longitudinal cavity mode resulting in beat-free pulses with a 6-ns FWHM temporal width. A gaussian-mirror outcoupler gives the pulses a uniform transverse intensity profile. The laser runs at full power for optimum pulse-to-pulse stability and to extend the life of the Nd:YAG rods.

Horizontally polarized¹ pulses exit the laser and pass through two attenuators that keep the pulses from damaging the OPO's crystals and mirror coatings. Each attenuator is made up of a half-wave plate and thin-film polarizer. The wave plate rotates the polarization angle and the polarizer transmits the horizontally polarized component. The vertical component is reflected into a beam dump. The first attenuator removes 70% of the pump energy and the second attenuator regulates the remaining 30% (190 mJ).

¹Horizontally polarized mean polarized in a plane parallel to the plane of the optical table.

After the attenuators, a third half-wave plate rotates the polarization to vertical and a reducing telescope shrinks the pulse diameter to 4.2 mm. The pulses then pass through a 7 x 7 x 5 mm thick Potassium Titanyl Phosphate (KTP) doubling crystal. The 115-mJ, horizontally-polarized 532-nm pulses emerging from the crystal pass through another half-wave plate—switching the polarization back to vertical—before entering the OPO cavity. When it enters the resonator, the 532-nm light has a 3.4 mm diameter.

CW Diode Laser

A single-mode diode laser (New Focus Model 6203) tuneable between 680 and 693 nm controls the OPO's output wavelength. The diode produces a narrowband (<5 MHz) horizontally-polarized 5-mW cw beam. An anamorphic prism pair and expansion telescope collimate the diode beam, giving it a 3.4 mm diameter before it enters the OPO cavity. The single-mode nature of the diode beam is evident from the well-separated rings it forms after passing through a fixed-length 6-GHz free-spectral-range Fabry-Perot etalon. A lens focuses the rings into a CCD camera (Sanyo Model VCB-3512T) whose output is displayed on a television monitor.

The red light from the diode and the green light from the pump mix inside a nonlinear crystal housed within the OPO cavity and create an infrared difference frequency. To ensure the infrared frequency is close to resonance with the target CO absorption line, the diode's wavelength is set with a wavemeter (Burleigh Model WA-20). Table 6 shows the diode laser wavelengths (given in wavenumbers) required to induce the accompanying R or P overtone transition. After setting the diode's wavelength with the wavemeter, a few minor adjustments to the diode drive current bring the OPO's infrared output into resonance with the CO. The diode settings must be adjusted several times during the day to compensate for changes in room temperature.

OPO Cavity

Three flat mirrors arranged in a triangular ring make up the singly-resonant OPO cavity (see Fig. 12). The ring cavity prevents losses associated with a backward

Table 6. OPO diode wavenumbers. These are the values in cm^{-1} required to produce the corresponding R or P transition in CO from $v = 0$ to $v = 2$.

R(0)	14525.42	R(7)	14500.97	R(14)	14480.01	P(1)	14533.05
R(1)	14521.72	R(8)	14497.76	R(15)	14477.30	The wavenumber for the doubled Nd:YAG is 18789.26 cm^{-1} .	
R(2)	14518.08	R(9)	14494.62	R(16)	14474.66		
R(3)	14514.52	R(10)	14491.56	R(17)	14472.10		
R(4)	14511.03	R(11)	14488.56	R(18)	14469.61		
R(5)	14507.60	R(12)	14485.64	R(19)	14467.19		
R(6)	14504.25	R(13)	14482.79	R(20)	14464.85		

traveling signal or idler beam. The lower left mirror transmits 532-nm and 2.35- μm light while fully reflecting the red light from the diode. The lower right mirror transmits 532-nm and 2.35 μm light while reflecting 60% of the red light. Incident angles on the left and right mirrors are 22.5° . The top mirror fully reflects red light at a 45° incident angle. The mirrors are placed close together—a round trip cavity length of 12 cm—to reduce the build-up time of the 2.3 μm idler pulse. A piezo-electric (PZT) driver attached to the top mirror's mount fine tunes the round-trip cavity length by adjusting the mirror in and out.

The resonant frequencies of the ring cavity do not normally overlap with the frequency of the diode laser. To match the two frequencies, a feedback circuit described in Appendix E monitors the red light escaping from the cavity and maximizes it by adjusting the top mirror's position. The circuit maintains resonance despite unavoidable cavity length fluctuations caused by temperature changes, table vibrations, and air currents. If the top mirror is driven through full spectral range of the ring cavity, two transmission maxima appear. The strongest maximum, visible as a single bright spot on the top mirror, occurs when the round-trip cavity length matches an integral number of diode laser wavelengths. A weaker maximum, visible as two closely spaced bright spots, occurs when two round-trip cavity lengths meet the resonance condition. The stronger resonance yields the greatest output energy.

The OPO will not work below a threshold pump energy which depends on the alignment of the 532-nm pump beam through the cavity KTP crystal and on the alignment

of the cavity mirrors. The pump threshold energy indicates how well the OPO components are aligned. With the red beam present, the 532-nm threshold energy is 30 mJ. Without the diode beam the threshold energy is 40 mJ. When the diode beam is absent, the OPO amplifies parametric fluorescence, decreasing the output energy and creating undesirable broadband output. Broadband output is visible on the CCD camera as a multitude of rapidly shifting rings flashing on and off with every YAG pulse. When the diode beam is present, the amplified seed light saturates the gain in the OPO before fluorescence can build up, forcing the OPO to operate at a single idler frequency. Single mode output is visible on the CCD camera as an intense 10-Hz brightening of the already-present diode laser rings.

OPO Pulse Characteristics

While individual pulse energies vary by up to 30 percent, the OPO generates a stable average pulse energy of 4 and 14 mJ at 2.3 μ m and 690 nm respectively, leaving more than 90 mJ at 532 nm unused. Two Faraday optical isolators protect the diode laser from the amplified red pulses. Downstream from the cavity, a dichroic beam splitter separates the infrared light from the green and red light. Colored glass filters remove any visible light remaining in the infrared beam.

When emitted from the cavity, the 2.3- μ m pulses are vertically polarized. A half-wave plate downstream from the cavity can switch the polarization to horizontal or any angle between. During most of the rotational relaxation experiments, the waveplate set the 2.3- μ m polarization angle at 57.9° from the horizontal.

Figure 12 shows the measured temporal profile of the 2.3- μ m pump pulses. A Gaussian curve fit to the profile has a 5.7-ns FWHM width and a transform-limited FWHM spectral bandwidth of 109 MHz. A Gaussian fit to the pulse's Fourier transform suggests a spectral bandwidth of 150 MHz. An indirect measure of the 2.3- μ m pump bandwidth based on probe absorption suggests the 2.3- μ m pump has a bandwidth of 165 MHz.

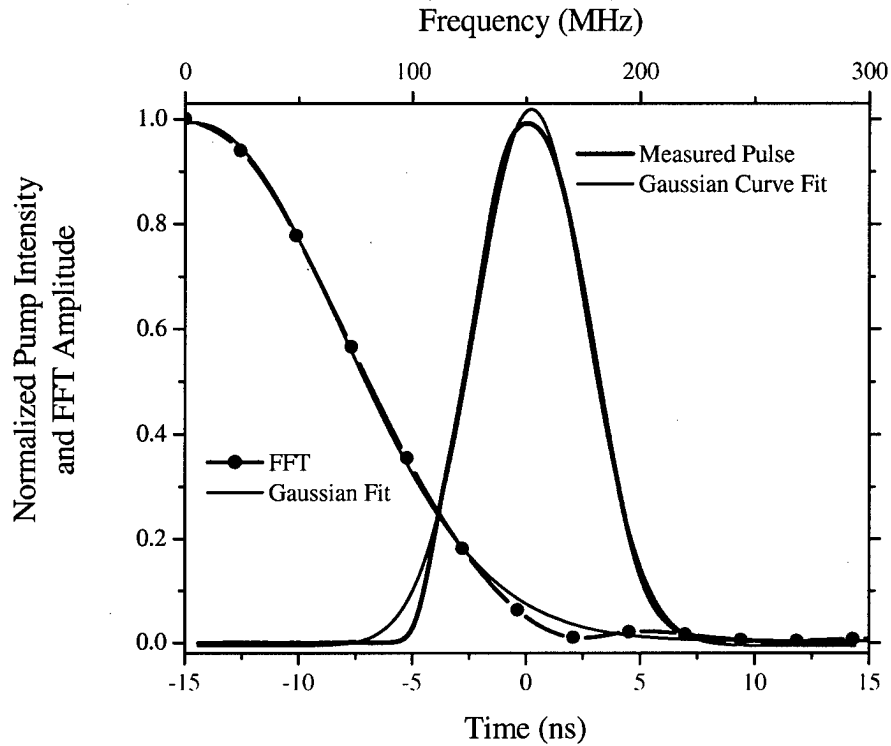


Figure 12. OPO pulse profile and bandwidth. The black curve shows the 2.3 micron OPO pulse intensity measured by a Boston Electronics PEM-L-3 photodetector. The red curve is a Gaussian fit. The green curve is a Fourier transform of the measured pulse and the accompanying blue curve is a Gaussian fit.

The infrared pulses emerging from the OPO have a poor transverse intensity profile. A pinhole spatial filter—a penny with a 0.025" hole drilled through the center—improves the profile as shown in Figure 13. The pinhole cuts the average 2.3- μ m pulse energy from 4 to 0.4 mJ which is still enough energy to cause ASE. To avoid ASE, a Keplarean telescope made with calcium fluoride lenses expands the 2.3- μ m pump diameter². The diameter required to avoid ASE depends on how much energy the CO

² By placing the pinhole downstream of the first telescope lens's focus, one can spatially filter the beam without the pulses damaging the pinhole.

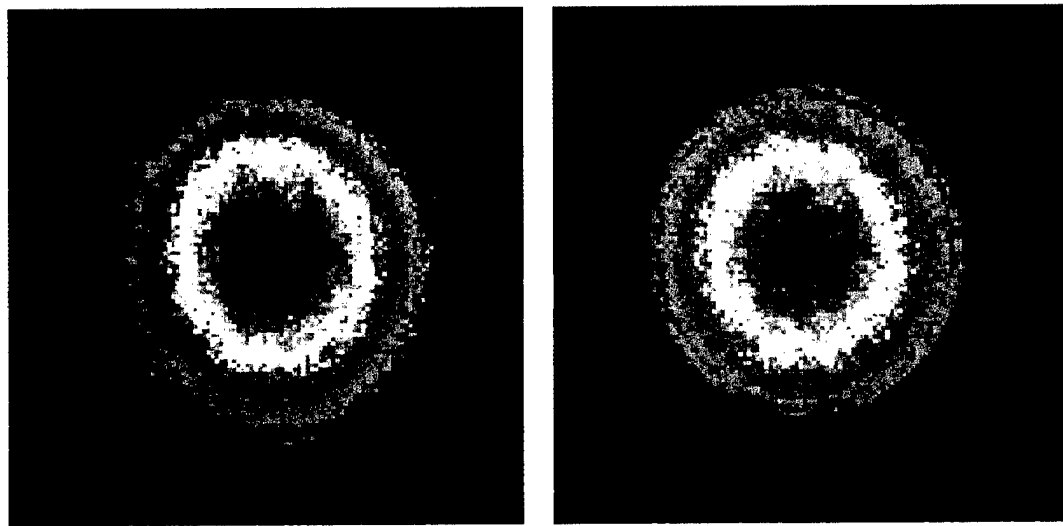


Figure 13. OPO spatial profile. The images show the intensity profile of the $2.3\text{ }\mu\text{m}$ pump pulses after the pulses pass through the spatial filter. A 1.8-cm diameter aperture has been closed around the image on the right to show the beam size.

absorbs. With a P(1) pump, the CO absorbs little of the pump energy and a 1.8-cm diameter suppresses ASE. With an R(6) pump, a 2.6-cm diameter is required.

An infrared camera (Spirocon Pyrocam I) displays the pump's spatial profile after it passes through the CO cell. With the camera, the operator can center the pump through the CO cell, optimally position the pinhole, and measure the pump pulse diameter.

CO Resonance

After the second telescope lens re-collimates the beam, a removable mirror directs the pulses through a 93-cm-long stainless-steel cell fill with 30 torr of CO.

Photodetectors (Boston Electronics Model PEM-L-3) monitor the pump intensity at the cell's entrance and exit. Tuning the OPO onto resonance with the desired CO absorption line requires adjusting the diode laser controller's drive current until the intensity at the cell exit drops sharply. The intensity is displayed on a digitizing oscilloscope (Tektronix Model 640 TDS). Pump absorption experiments show the minimum change in wavelength made by the controller is large enough to miss or step over line-center,

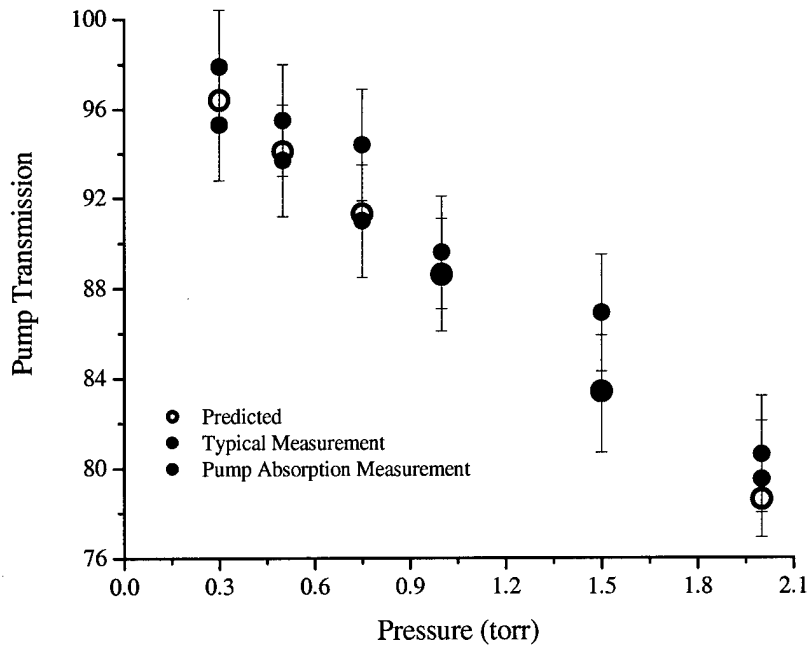


Figure 14. Pump transmission vs. pressure. The plot shows pump transmission vs. pressure on the P1 overtone between $v = 0$ and $v = 2$. The open black circles show predicted absorption. The red circles indicate measured transmission when the OPO is tuned to resonance using the oscilloscope-based procedure. The blue circles show absorption when the OPO is scanned many times over the absorption feature to find line center resonance.

therefore observing a minimum intensity on the oscilloscope does not guarantee ideal resonance. Figure 14 shows the transmission of a P(1) pump through CO as a function of CO pressure when using the oscilloscope trace as a guide and when scanning the pump repeatedly back and forth over the transition. The oscilloscope-based data is consistently less resonant than the best case from the scanned data. Fortunately the discrepancy is small given the measurement error.

Gentec Model ED-200L and ED-100A energy meters measured pump energy. The meters have a published single-shot accuracy of $\pm 5\%$ of the energy reading. The ED-200L meter measured pump energy at the CO cell's exit while the ED-100A measured the reflected energy from the Brewster window at the cell's entrance. The

pump polarization was switched to vertical during the absorption experiments so the Brewster window could reflect a detectable amount of energy. Gentec EDX-1 amplifiers boosted each meter's signal by a factor of ten before sending it to a Gentec Duo readout. The Duo displayed the pulse energy and transmitted a DC voltage representing pulse energy to a National Instruments Model BNC-2110 breakout box and Model PCI-6111DAQ card. The lamp trigger from the Nd:YAG laser controlled the DAQ card acquisition rate. A program written with National Instrument's Labview retrieved the data from the DAQ card, averaged the pulse energy, and saved the data as a text file on a computer hard drive. The CO pressure and temperature did not change significantly with time and were recorded manually in a laboratory notebook.

Because theory predicted the transmitted pump energy to within a few percent, the absorbed pump energy was calculated using the measured transmitted energy and the known optical losses caused by windows and mirrors between the CO and the Gentec meter.

OPO Operating Procedures

The Nd:YAG flashlamps and red diode laser warmed up for one hour before the OPO was turned on. Overnight changes in the laboratory temperature misaligned the OPO cavity requiring the operator to vertically adjust the lower left OPO cavity mirror. Once the Nd:YAG laser was firing, the alignment of the 532-nm pulses through the cavity could be verified. Because the 532-nm pulses heated the KTP crystal, the cavity's vertical alignment had to be re-optimized after the crystal reached thermal steady-state. A horizontal correction to the 532-nm steering mirror immediately upstream of the resonator was often required to fully suppress broadband lasing, evident as intermittent flashing rings between the intense single mode rings on the CCD camera monitor. With the OPO operating, the 2.3- μ m beam was aligned through the pinhole spatial filter, expansion telescope, and experimental cell using the IR camera. Small corrections to the

pinhole filter position were necessary about once every hour to maintain the maximum average pulse energy.

Operating the OPO on a different CO absorption line required tuning the diode to the correct wavelength and rotating the OPO cavity crystal until phase-matching conditions were met and bright single-mode flashing rings appeared on the CCD camera. Remarkably, the downstream alignment remained intact during this procedure.

Injection seeding was disabled when shutting down the Nd:YAG laser. If the Nd:YAG was turned back on without reactivating the seed, the OPO did not run single mode. An inactive seed also caused a lower-than-expected threshold energy for broadband OPO output. The seed prevented the YAG from operating on different lines at the cost of efficiently accessing the available gain on those lines. The result was a 10 percent drop in output energy when the YAG was seeded. Because the YAG output was greater when unseeded, more energy passed through the volume-control waveplate than expected, reducing the broadband threshold. Figure 15 shows the temporal profile of seeded and unseeded YAG output.

Experimental Cell

The stainless-steel cell containing the CO during the experiment was 71-cm long with a 6-cm clear-aperture diameter. A large aperture allowed the expanded pump beam to pass through the CO unobstructed. Uncoated and wedged CaF₂ windows at both ends of the cell transmitted the pump and probe beams. The upstream window was mounted at Brewster's angle while the exit window was set perpendicular to the cell axis. The Brewster and exit windows were wedged to eliminate interference fringes visible on the IR camera. Buna O-rings formed the vacuum seal between the stainless steel cell and the windows. A K-type thermocouple inside the cell but outside the beam path monitored gas temperature. Over several hours, changes in room temperature could alter the measured

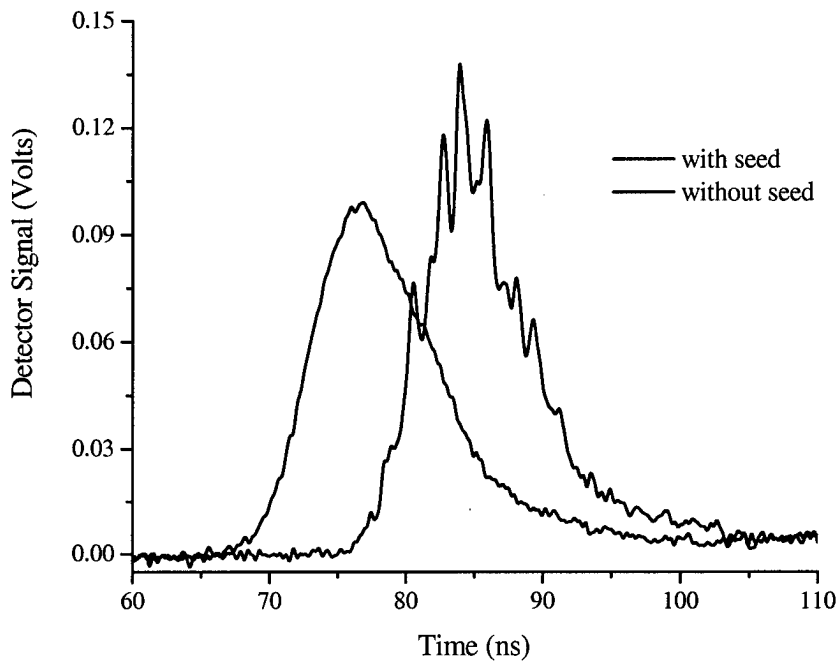


Figure 15. Seeded and unseeded YAG pulse. The curves show the profiles of the YAG pulse with and without the injection seed activated. The unseeded pulse shows multimode structure. The laser pulse forms earlier after the Q-switch when the seed is active.

gas temperature by up to 4 K. MKS Baratron 1-torr and 2-torr capacitance manometers (Models 622A01TBE and 622A02TBE) connected to the cell measured the CO pressure. According to the manufacturer, the manometers were accurate to within 0.25% of their reading. Both manometers were purchased new for the experiment, and both gave nearly identical readings when exposed to the same pressure. A Welch Duo-Seal roughing pump and a diffusion pump evacuated the cell to 6 mtorr, after which the cell was filled with at least 10 torr of CO and evacuated again to purge unwanted residual air. The cell was filled a second time with the desired amount of CO and isolated with a valve. The cell had a cell leak rate of 20 mtorr per hour and was refilled with CO whenever the pressure rose by more than a percent above the desired value.

When the pressure in the cell was above 10 torr, the CaF_2 windows flexed and mechanically steered the probe beam out of optimal alignment with the detectors. Since pressure during the rotational relaxation experiments remained below 2 torr, beam steering never became a problem.

PROBE LASER (LEAD SALT DIODE LASER)

The probe laser was a Müetek Laser Systems GMBH Model OLS-150 lead salt diode laser purchased through Boston Electronics, Inc. The laser diode itself was manufactured by Laser Components GMBH and was continuously tunable from 4.6 to 5.0 μm with an average multimode output power of 1.0 mW. According to manufacturer specifications, individual modes were less than 30-MHz wide, including current jitter from the diode controller. A controller (Müetek TLS-150) set the diode's temperature and current either through computer commands over a GPIB interface or manually from the controller's front panel. Computer commands adjusted the current in 5- μA steps (or smaller) while the front panel allowed steps of 100 μA . Because of jitter in the current, the manufacturer recommended a 15- μA minimum step size. With oscilloscope averaging, step sizes as small as 5- μA produced discernable changes in CO probe absorption. Attempts to find a fixed current-to-frequency calibration factor by measuring known CO linewidths showed that the factor ranged in value from 0.5 to 1.0 MHz per μA depending on the diode temperature and age. The diode temperature could be set with an accuracy of 0.01 K.

Liquid nitrogen cooled the diode to its operating temperature of between 90 and 130 K. A Varian Model VA-20-DD/0 20-liter-per-second ion pump and a Terranova Model 741 controller (both purchased from the Duniway Stockroom company) continuously maintained a vacuum of less than 1 μtorr at the laser head, preventing water from condensing on and destroying the diode. The continuous vacuum compensated for a slow leak in the laser head.

Wavelength Tuning

The diode laser wavelength is tuned by adjusting the diode's temperature and current. Before conducting the experiment, the temperature and current settings that produced the desired $v = 2$ -to- 3 probe wavelengths had to be found. The probe was initially sent through a 119-cm long, 1.5-cm clear-aperture diameter stainless steel CO cell heated to 700 °C. Four Watlow ceramic fiber heaters formed an oven that housed the cell. An Omega CN9000S PID controller maintained the set-point temperature by monitoring a K-type thermocouple in contact with the outside wall of the cell. The probe beam passed through CaF₂ wedged windows mounted at both ends of the cell. Hollow, silver o-rings (Grotenrath Rubber Products Co. Inc. Part # 1000-094X010-321Ag) provided the high temperature vacuum seal between the windows and stainless steel. The cell was filled with 30 torr of CO at room temperature and isolated. An MKS 100-torr capacitance manometer measured cell pressure. Without a thermocouple inside the cell, gas temperature was estimated using the cell pressure and the ideal gas law. With the PID controller set to maintain 700 °C, the gas pressure in the cell rose from 30 to 74 torr, corresponding to a final gas temperature of 728 K. From that point the pressure inside the cell decreased slowly with time revealing a CO leak from the cell. When the oven was turned off and allowed to cool, the final cell pressure was less than the initial 30 torr, confirming that CO was escaping. With the atmospheric pressure in the room at 625 torr, the CO was not escaping out of the cell windows. Replacing the valve isolating the cell from the vacuum system did not prevent the loss. The valve was attached fifteen inches up a quarter-inch-diameter stainless-steel tube welded to the cell. The pressure transducer was thirteen inches up the tube. Both were cool to the touch when the oven was operating.

With the heated cell, all transitions ($v = 0$ -to- 1 , $v = 1$ -to- 2 , and $v = 2$ -to- 3) absorbed the probe, making it impossible to distinguish between the different Δv transitions without a monochromator. In addition, the heat and pressure-broadened line shapes overlapped when the diode was tuned across two lines with similar wavelengths.

A less ambiguous method for identifying the correct probe laser settings used the OPO to create the excited state population.

The OPO excited large populations into the individual J levels of $v = 2$, allowing one to distinguish easily between $v = 0$ -to-1, 1-to-2, and 2-to-3 transitions on the oscilloscope. When the diode was tuned across a $v = 0$ -to-1 transition, the CO absorbed the pump beam across the entire oscilloscope trace. When the diode was tuned across a $v = 1$ -to-2 transition, the CO amplified the probe but only in the trace region after the trigger. When the diode was tuned across a $v = 2$ -to-3 transition, the CO absorbed the probe but only in the trace region after the trigger. After setting the OPO to populate the $v = 2$, $J = 8$ level, the diode laser was manually scanned across its entire current range at many different temperatures. Upon finding a $v = 1$ -to-2 or 2-to-3 transition, the probe beam was passed through a 0.3-meter McPherson Model 218 monochromator (150-groove-per-millimeter grating blazed at 17° for 4 microns) to identify the wavelength of the mode being absorbed or amplified. The diode's power weakened at higher temperatures where the laser operated at shorter wavelengths, giving a poor signal-to-noise ratio on high-valued R transitions. Because the diode power was concentrated into fewer modes at low temperatures and longer wavelengths, P transitions gave a better signal-to-noise ratio when probing high J levels despite their weaker absorption cross sections. Table 7 shows the diode controller's temperature and current settings that resulted in the desired transition. An R(15) or P(15) probe was never found while P(19) and greater transitions were too weak to be useful. The set points corresponding to a given transition change as the diode ages and settings that worked once may not work a few weeks later.

The diode laser occasionally mode hopped. This was troublesome when scanning the diode across an absorption lineshape. Figure 16 shows an example of mode hopping on the R(0) line of a $v = 2$ -to-3 transition.

Table 7. Probe laser settings. The settings give the designated R or P transition from $v = 2$ to 3.

Trans	T(K)	I (mA)	Trans	T(K)	I (mA)
R(0)	111.50	423.9	P(10)	101.50	424.1
R(1)	112.40	567.6	P(11)	101.00	416.6
R(2)	113.00	568.3	P(12)	99.50	411.9
R(3)	113.75	558.0	R(13)	118.50	569.4
R(4)	112.50	554.6	P(14)	97.50	403.2
R(5)	113.00	559.4	P(15)		
R(6)	114.00	544.8	P(16)	96.75	344.7
R(7)	114.50	544.3	P(17)	95.00	358.5
P(8)	103.00	445.6	P(18)	93.75	351.9
P(9)	102.00	443.1	P(19)		

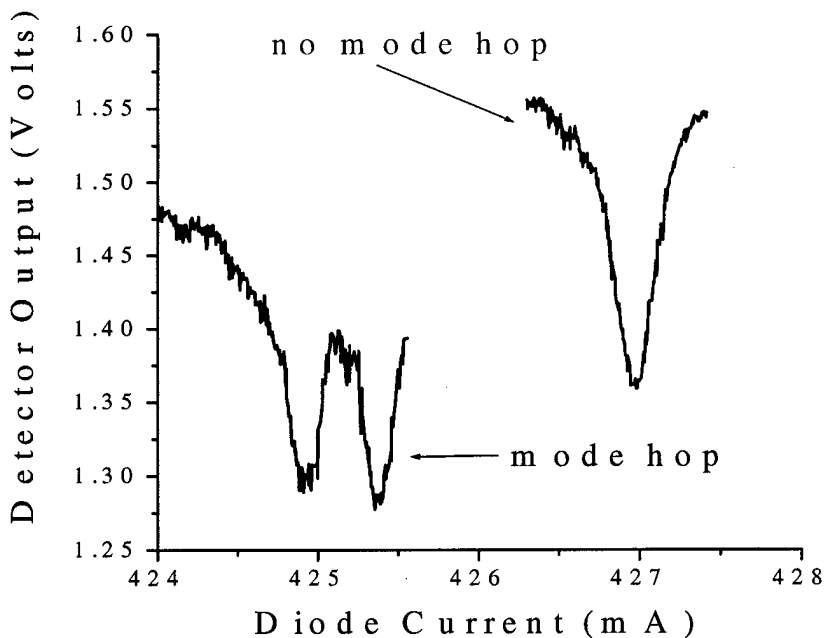


Figure 16. Diode laser mode hop. The black line shows probe transmission as a function of current when a mode hop occurs during a scan. The blue line shows the same transition scanned later in the day when a mode hop did not occur. The difference in the absolute detector voltage shows the trend, generally observed, of greater output power with increasing diode current.

Probe Polarization

According to the manufacturer, light from the diode is 80% vertically polarized. A horizontal polarization was desirable to reduce optical losses. After a gold-coated off-axis parabolic mirror collimated the diode laser's divergent output, a periscope switched the polarization from vertical to horizontal. Beyond the periscope, the beam passed through two thin-film polarizers. The polarizers, built by Rocky Mountain Optics on CaF₂ substrates, were effective at wavelengths between 4.6 and 5.1 microns. Gold-coated mirrors steered the beam twice through the experimental cell before sending it to an InSb detector or through the monochromator. The combination of thin film polarizers and two passes through the cell's Brewster window resulted in a beam more than 99% horizontally polarized when it reached the final detector.

Probe Beam Path

Because boosting the pump energy to create a larger excited-state population would have caused ASE, the probe was instead passed twice through the CO. Optical losses were minimized to maintain the already weak probe power. A gold-coated mirror with an 8-meter radius of curvature prevented clipping by re-collimating the probe on its return trip through the CO. Once the beam was aligned through the cell and into the detectors, the off-axis parabolic mirror governing the probe's divergence was adjusted to maximize the signal. Maximizing the signal came at the cost of controlling the diameter of the probe beam inside the cell which ended up being 0.7 cm at the curved mirror. The probe diameter was measured by closing a circular aperture around the beam until 86% of the initial power remained. A drawback to reflecting the probe back through the cell was that on the return trip the beam traveled at a small angle to the axis established by the pump beam. Because the pump intensity was not uniform, the return probe passed through regions where the number density of excited molecules was not as high as in the pump beam's center.

Because CO pressures were kept below 2 torr, the CO absorbed no more than 70 percent of the incident pump energy, making it reasonable to expect a uniform energy

distribution in the CO. At higher pressures, the CO at the cell entrance absorbs most of the pump energy, making the path length of the probe laser through the excited molecules uncertain.

INSB DETECTOR

The probe laser had an average multimode power output of 1 mW. The power expected to reach the detector from a single resonant mode after optical losses and being absorbed by CO was less than 100 microwatts. Calculations predicted the excited CO would absorb less than 1% of the incident power on weak transitions under conditions of rotational equilibrium. And the change in absorption caused by rotational relaxation would only last a few hundred nanoseconds. Such stringent conditions required a fast and sensitive detector. The detector purchased for the experiment was a liquid-nitrogen-cooled Kolmar Technologies Model KISDP-0.5-J1 InSb detector with integrated amplifier. The detector had a 12kV/W sensitivity, a 10-ns rise time, and a $0.5 \times 0.5 \text{ mm}^2$ area.

To maximize the signal from the detector, a CaF_2 lens focused incoming light onto the detector surface. To test whether the focused diode beam could overdrive the detector, the full multimode power of the diode laser was focused into the detector while overhead transparency sheets were placed sequentially in the beam path. The measured loss for each successive sheet was constant, showing the detector's response remained linear. The detector was sensitive to the $2.3\text{-}\mu\text{m}$ light from the pump as well as to the 4.6 to $5.0 \mu\text{m}$ light from the diode. An OCLI Model L03372-9 long-pass filter with a cut-on wavelength of $3.5 \mu\text{m}$ was placed over the detector's face to prevent scattered pump light from distorting the probe laser signal.

To experimentally verify the InSb detector's response time, the detector was used to measure the temporal profile of the OPO pump pulses. The profile measured by the InSb detector was compared with one measured by the faster PEM photodetectors whose response time was less than 200 ps. Figure 17 displays the profiles measured by both detectors. The center of both pulses was aligned to simplify the comparison.

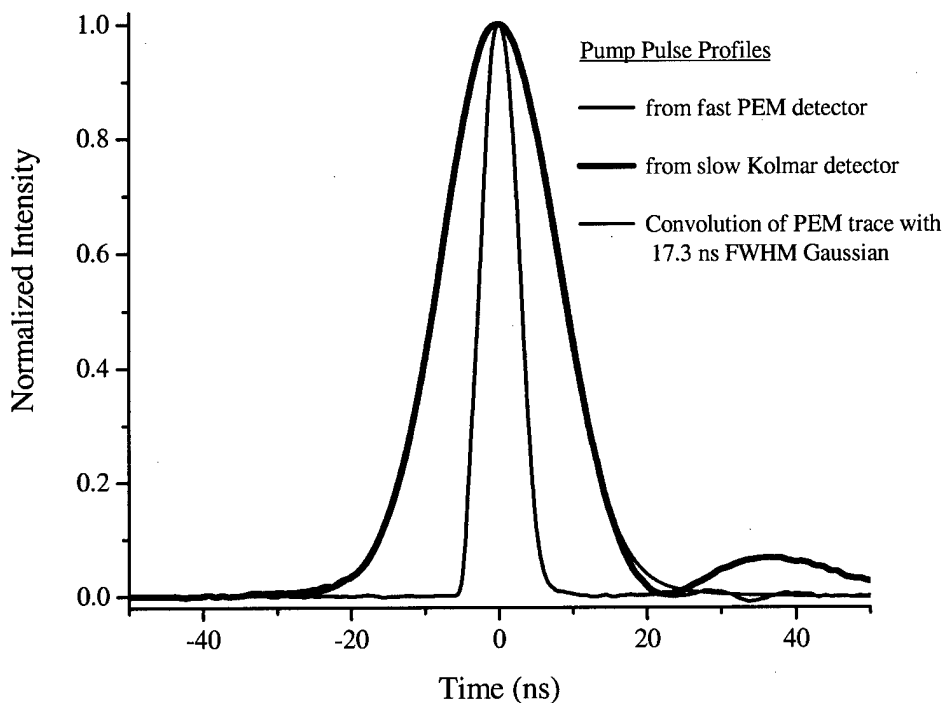


Figure 17. InSb detector response function. The curves show the $2.3\text{ }\mu\text{m}$ pump pulse measured by a PEM detector (< 200 ps rise time) and the slower InSb Kolmar detector. The red line shows the convolution of the PEM pulse with a 17.3-ns FWHM gaussian response function.

Assuming the PEM profile represents the true pulse, the PEM trace was convolved with a Gaussian response function until, at a FWHM response function width of 17.3 ns, the convolved curve matched the curve from the InSb detector. As seen in Figure 17, the fit between measured and convolved profiles is good. The second signal rise in the Kolmar detector output came from ringing in the electronics of the InSb detector. When the detector was originally purchased, the ringing—which occurs only when measuring intense, rapidly changing signals—was much worse. The ringing pulse in Fig. 17 is small because a warranty adjustment was made by Kolmar. Since ringing occurred only when probing the pumped level and since reducing the CO pressure reduced the ringing, the detector was used as configured.

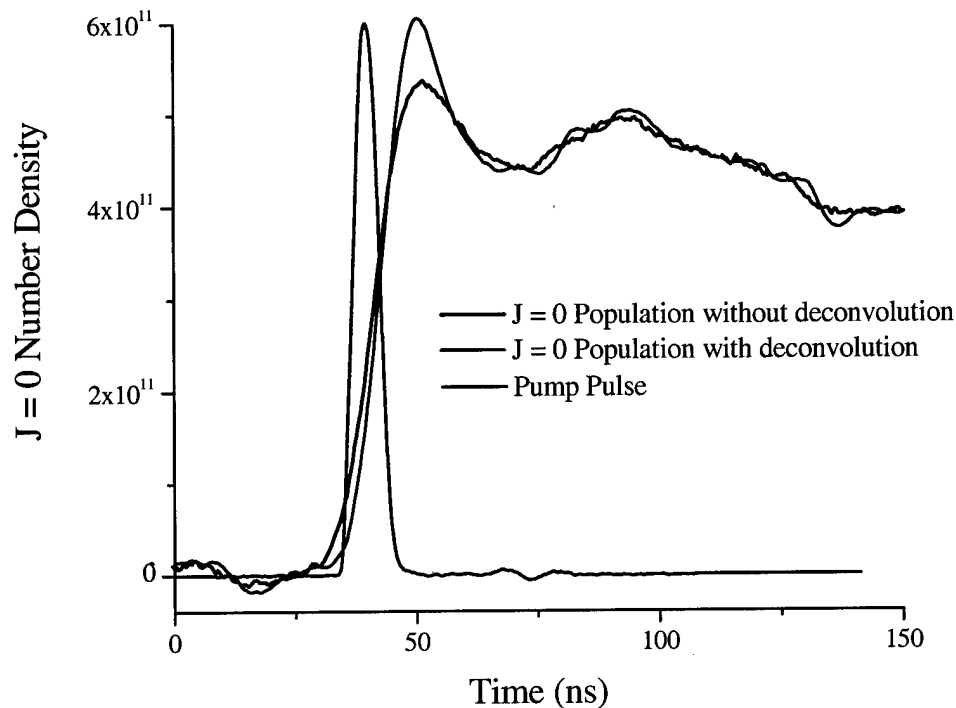


Figure 18. Deconvolution of the pumped level. The black curve shows the $J = 0$ population calculated without deconvolving the data to account for the response time of the InSb detector. The red curve shows the effect of deconvolution. The drop in population immediately after the peak is a spurious effect caused by detector ringing. The CO cell pressure was 0.3 torr.

Deconvolving the detector's response function out of the measured signal gives data that more accurately reflects the population changes. Figure 18 shows the population created in the $J = 0$ rotational level by a P1 pump with and without accounting for the response function. The deconvolution was performed using Microcal Software corporation's Origin program. Figure 18 shows the detector's response time affects only the initial pumped population and that the detector accurately tracks the molecules leaving the pumped level. Deconvolution was eventually abandoned because the noise it added to the data was as large any improvements it made. Deconvolving signals from probes of adjacent levels showed no change from the signal as it originally came from the detector.

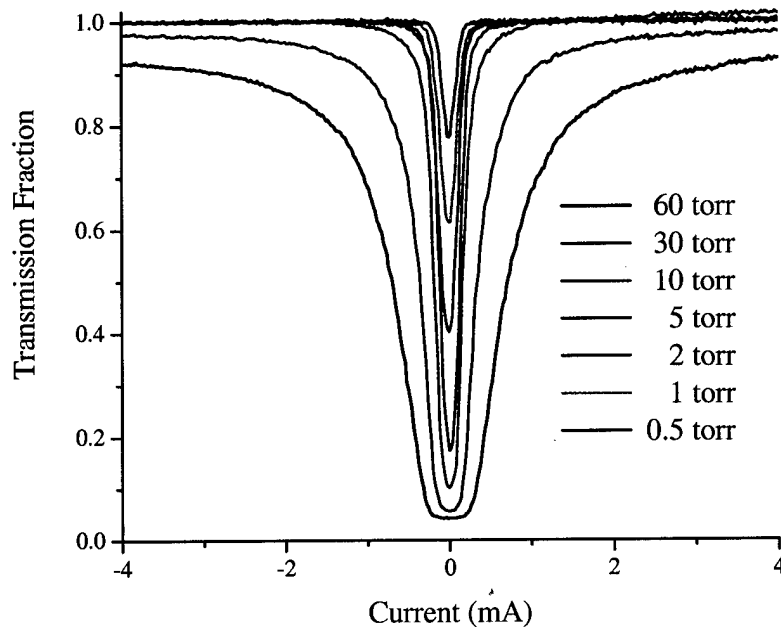


Figure 19. P29 probe transmission vs. pressure ($v = 0$ to 1). Probe transmission on the P29 transition between $v = 0$ and $v = 1$ at various pressures. The probe beam passed through the monochromator before reaching the detector. That the high pressure signal did not drop to zero at line center indicates the presence of non-resonant modes. The loss of intensity in the wings at high pressure is caused by the cell windows mechanically steering the probe beam.

Probe, Detector, and Monochromator Operation

To verify that Beer's Law accurately predicted probe absorption, the probe was tuned to three $v = 0$ -to-1 transitions. The tests were conducted on the P24, P25, and P29 lines, allowing for a wide range of absorption values between pressures of 0.3 and 2.0 torr. Figure 19 shows the transmission of the P29 line as a function of diode current (equivalent to wavelength) for a range of pressures. After passing twice through the experimental cell, the probe beam entered the monochromator. With its slits narrowed, the monochromator had a FWHM transmission window of ~ 20 GHz that completely suppressed adjacent longitudinal modes whose spacing was greater than 40 GHz. Despite the monochromator acting as a filter, light from the diode laser still reached the detector even when, at 30 and 60 torr, the CO absorbed all resonant light as indicated by

the flattened high-pressure transmission curves at line center. To ensure room light, scatter off an optic, or electrical noise did not cause the DC signal, the beam was blocked at the curved mirror reflecting the probe beam back through the CO cell. With the beam blocked, the detector signal dropped to zero, showing that the DC signal came from probe laser light that passed twice through the CO but remained unabsorbed.

Figure 20 shows a similar experiment on the P24 and P25 transitions where the diode was tuned across the entire transmission range of the monochromator at a CO pressure of 2 torr. At 2 torr and line center, the CO should have completely absorbed all incident light. In the P25 case the transmission fails to reach zero suggesting that other modes transmitted by the monochromator but not resonant with the CO are present. The P24 case reveals those modes as they are tuned across the absorption feature. That the non-resonant modes did not cross the absorption feature in the P25 case was expected.

During the initial mapping of the $v = 2$ -to-3 and 1-to-2 transitions, the monochromator setting was recorded with each new transition. With the monochromator set to pass the desired wavelength, the diode laser temperature and current were scanned to find the modes with the strongest transmission through the monochromator. When these modes were later passed through CO to verify resonance, the CO often failed to absorb them, even after scanning the diode across the monochromator's 20 GHz FWHM transmission window. This indicated that tuning the current created modes that appeared, shifted, and disappeared without crossing the resonant wavelength.

The monochromator passed modes with frequencies within ~ 10 GHz of the resonant mode, leaving the fractional contribution of the resonant mode to the detector output unknown. To reduce losses to the resonant mode, the monochromator was removed from the beam path during rotational relaxation experiments. The monochromator was still necessary to the experiment as it was the only way to confirm the wavelengths of resonant modes. For example, at a diode temperature of 112.5 K, resonant modes appeared at current settings of 563.3 mA ($J = 4$ probe at 4.767 μm) and 566.3 mA ($J = 1$ probe at 4.742 μm). The monochromator easily filtered such disparate wavelengths, verifying $J = 1$ as the probe or vice versa.

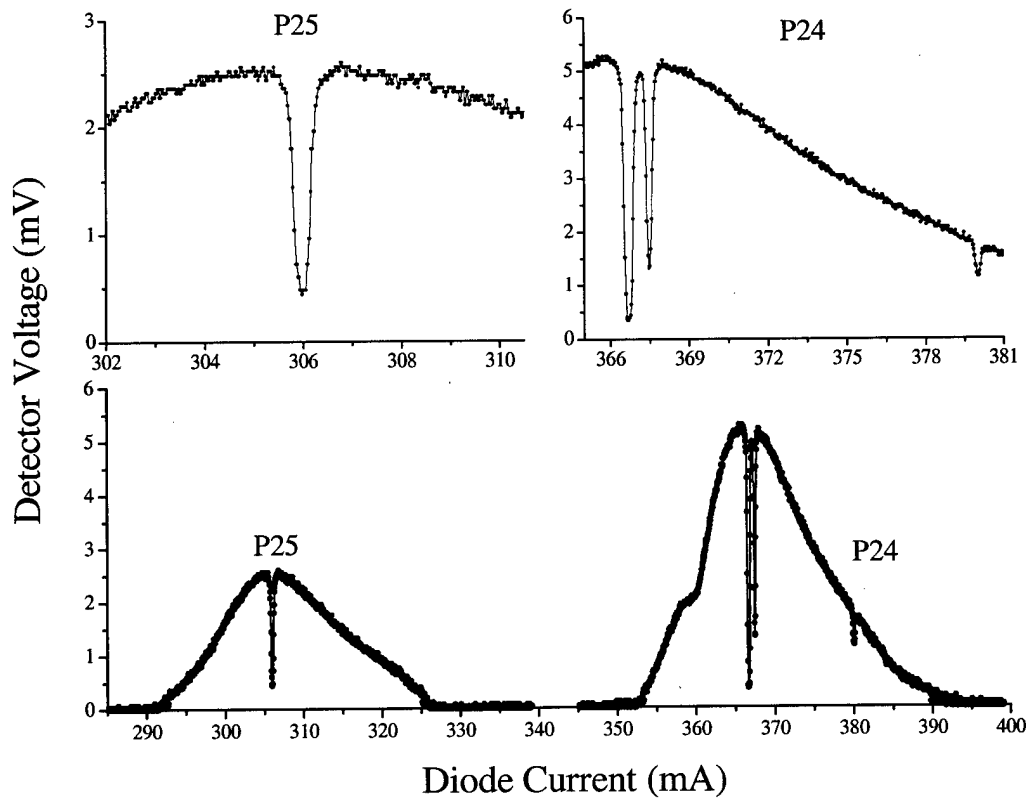


Figure 20. Evidence for non-resonant modes. These curves show the transmission of the probe beam through both the CO cell and the monochromator as a function of diode current. The CO pressure was two torr. The bottom graphs show the monochromator's full 20-GHz transmission width. The upper graphs show a more detailed view of the interesting features in the lower graphs. The P transitions indicated are $v = 0$ -to-1 transitions.

Additional modes were not a serious problem on $v = 0$ -to-1 transitions since the full intensity of the resonant mode could always be measured by increasing the pressure until the CO absorbed 100% of the resonant signal. Finding the contribution of non-resonant modes when measuring excited-state populations was not so simple. Eq. (3.2) gives Beer's law when a non-resonant signal is present

$$I(t) = I_0 e^{-\frac{A\lambda^2}{8\pi} S(v,t) L \frac{g_u}{g_l} N_j(t)} + I_{DC} \quad (3.2)$$

where I_0 is the resonant signal, I_{DC} is the non-resonant signal, and $I(t)$ is the measured signal. The other variables are defined in Eqs. (1.22) and (1.23). Solving Eq. (3.2) for $N_J(t)$ and noting that $N_J(0) = 0$ leads to

$$N_J(t) = -\frac{8\pi}{A\lambda^2 L} \frac{g_J}{g_u} \frac{1}{S(v, t)} \ln \left[\frac{I(t) - I_{DC}}{I(0) - I_{DC}} \right] \quad (3.3)$$

Since the values of $I(0)$ and $I(t)$ are measured, one needs I_{DC} to calculate $N_J(t)$. Eq. (3.4) gives the fraction of uncertainty in $N_J(t)$ associated with an uncertainty in I_{DC} :

$$\frac{dN_J(t)}{N_J(t)} = \frac{\left[\frac{1}{I(0) - I_{DC}} - \frac{1}{I(t) - I_{DC}} \right]}{\ln \left[\frac{I(t) - I_{DC}}{I(0) - I_{DC}} \right]} dI_{DC} \quad (3.4)$$

Once the excited CO reaches rotational equilibrium, Eq. (3.2) can be solved for I_{DC} using the absorbed pump energy E_{abs} given by Eq. (3.1) to estimate $N_J(t_{eq})$ where t_{eq} refers to any time after rotational equilibrium is reached:

$$I_{DC} = \frac{I(t_{eq}) - I(0) e^{-\frac{A\lambda^2}{8\pi} S(v, t_{eq}) L \frac{g_u}{g_J} N_J(t_{eq})}}{1 - e^{-\frac{A\lambda^2}{8\pi} S(v, t_{eq}) L \frac{g_u}{g_J} N_J(t_{eq})}} \quad (3.5)$$

$$N_J(t_{eq}) = \frac{E_{abs}}{(hc/\lambda_{pump})} \cdot \frac{1}{\pi(d/2)^2 L_b} \cdot e^{-k_v M t_{eq}} \cdot \text{Pr}(J)$$

In Eq. (3.5), E_{abs} is the absorbed pump energy, λ_{pump} is the pump wavelength, d is the pump beam diameter, L_b is the probe beam's path length through the excited CO, k_v is the rate constant for vibrational loss out of $v = 2$, M is the gas number density, and $\text{Pr}(J)$ is the equilibrium fraction of molecules in the J level given by Eq. (1.17). An expression for dI_{DC} can be obtained by taking the derivative of Eq. (3.5) with respect to E_{abs} . While

the uncertainty in the absorbed energy for a single shot is $\pm 5\%$, the uncertainty associated with the average of 100 shots should be less. Using Fig. 14 as a guide, the assumed uncertainty in absorbed energy was $\pm 2\%$. Pump absorption measurements showed that I_{DC} made up 40% of the total signal depending on the particular transition. In the worst case I_{DC} made up 65% of the signal, and in the best case only 10%. The uncertainty in population caused by I_{DC} ranged between 4 and 5 percent.

Probe Absorption and Beer's Law

After accounting for I_{DC} , the $v = 0$ -to-1 absorption data was compared with theory. Figure 21 shows the predicted and measured transmission on the P24, P25, and P29 lines. The top left graph shows a linear plot of transmission vs. pressure while the top right graph shows the same data plotted against a natural logarithmic scale. Though theory and experiment follow the same trend, the theoretical predictions lie outside the error band of the experiment. Comparing this author's theoretical calculations with the predictions made by the Hitran 92 database showed both forecast the same transmission values given an infinitely narrow probe bandwidth. After accounting for the 30-MHz probe bandwidth, this author's theory predicts transmission slightly greater than the Hitran code predicts. One possible cause for the mismatch between measurement and theory was that the spectrally narrow probe beam saturated the transition. But modeling made it clear the diode laser was too weak and the beam diameter too large for the probe to saturate the transition. Being unable to find theoretical problems, the experiment was repeated only to give the same results. Other researchers investigating CO experienced similar problems [53]. In a recent diode laser experiment, researchers directly measured CO absorption on the $v = 0$ -to-2 overtone transitions and found their measured line strengths to be 4 - 15 percent less than those given in the Hitran database. Assuming a comparable discrepancy in the $v = 0$ -to-1 line strengths, inserting 0.84 into the P24, P25, and P29 line strength variables improves the match between theory and data as shown in the lower two graphs of Fig. 21. That the 0.84 factor corrects all three transitions suggests a systematic error in the

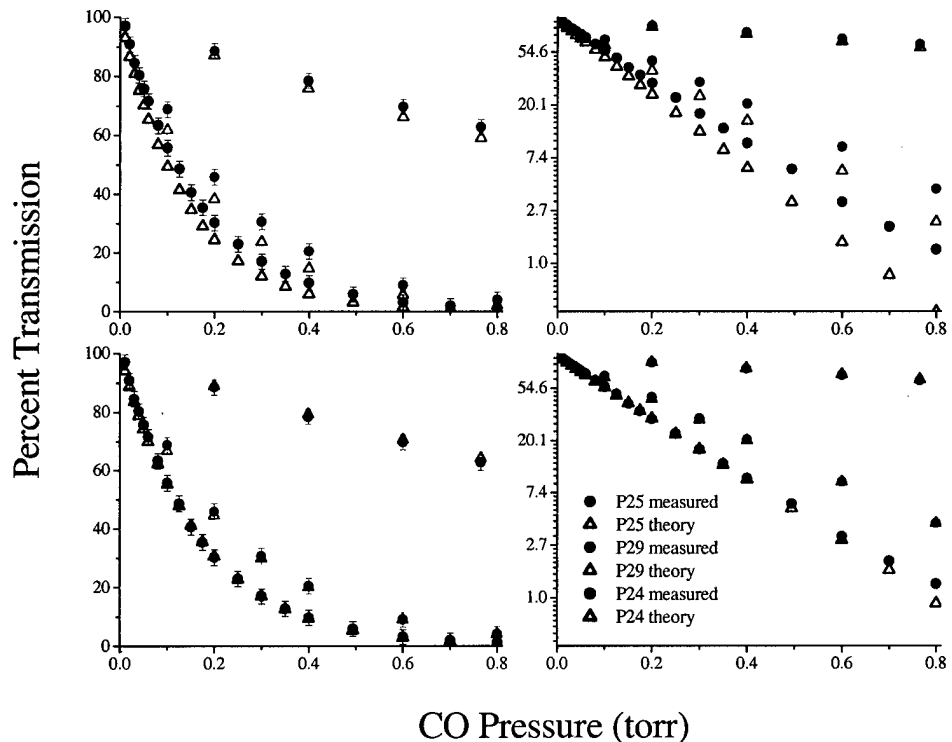


Figure 21. Testing Beer's Law with the diode. The graphs compare the measured and theoretical transmission values for the P24, P25, and P29 $v = 0$ -to-1 transitions. The upper and lower graphs show the match between experiment and theory without and with the 0.84 correction factor respectively. The right-hand graphs show the data plotted on a natural logarithmic scale.

absorption cross section. Fortunately constant factors multiplying the line strength do not affect the accuracy of the rate constant measurements as explained in the data scaling discussion at the end of the chapter.

With the absorbed pump energy, the number of molecules initially excited into the upper level and the final equilibrium populations in all J levels can be calculated. Figure 22 compares the final populations measured by the probe with the populations calculated from the absorbed pump energy. The 0.84 correction factor was used in calculating the predicted transmission. Fig. 22 shows that theory and measurement agree within the experimental

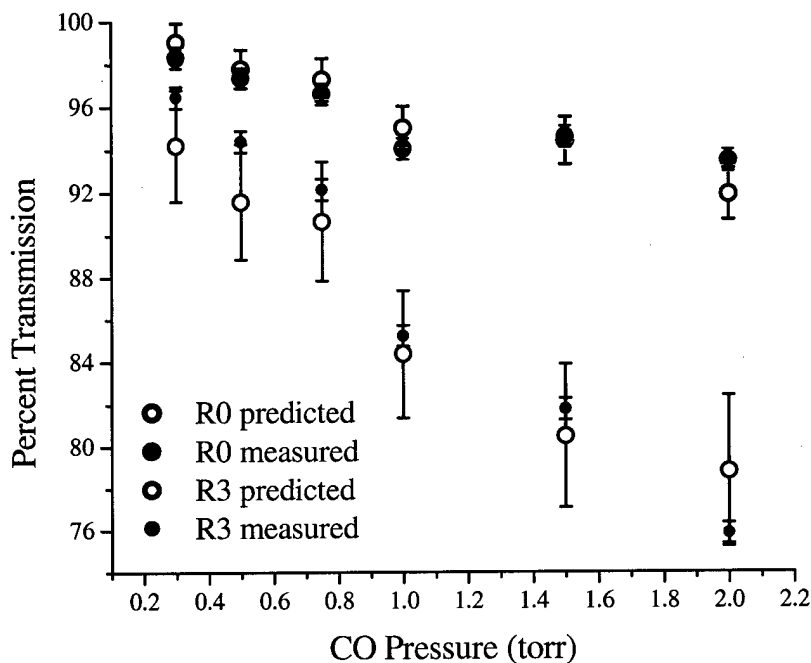


Figure 22. Independent population predictions. The graph displays the results of an experiment investigating whether the measured probe transmission on the R0 and R3 lines under rotational equilibrium conditions matched the predicted probe transmission based on the amount of P1 pump energy absorbed.

error. The large error bars on the predicted values are linked to the error associated with measuring the absorbed pump energy.

DATA ACQUISITION: THE OSCILLOSCOPE

Because the excited molecules reached rotational equilibrium after a few hundred nanoseconds, a fast digitizing oscilloscope (Tektronix Model TDS 680B) acquired the signal from the InSb detector. The TDS 680B had a 5 Gs/sec maximum sampling rate and a 1 GHz bandwidth. A PEM photodetector placed behind a dichroic turning mirror 120-cm upstream of the experimental cell detected bleed-through pump energy and triggered the oscilloscope (see Figure 10). Because the PEM voltage's rising edge triggered the oscilloscope, the time between the trigger point and the peak of the PEM

pulse varied by one to two nanoseconds depending on the trigger's sensitivity setting and the energy of each pulse.

The oscilloscope performed three important signal conditioning tasks before passing the data to a storage computer over a GPIB bus. It removed a large DC vertical offset voltage from the detector signal so that one could amplify the comparatively small transient signals with maximum oscilloscope gain. It removed random noise and shot-to-shot variations by taking a running average over a user-selectable number of shots. It also subtracted a noise trace stored in memory from the acquired waveforms.

To amplify the weaker transient rotational relaxation signal without amplifying the DC component contributed by non-resonant modes, the oscilloscope added a negative DC offset to the voltage coming from the detector. The DC value of the resultant waveform displayed on the oscilloscope was near zero volts. This permitted the operator to expand the oscilloscope gain and zoom in on the transient absorption feature. In Figure 23, the top black curve shows a single relaxation trace with the full signal from the InSb detector. The black curve in the lower graph shows a similar trace, but with most of the DC component removed and the oscilloscope gain increased. The red curves show data taken under similar circumstances but with the scope averaging turned on (100 shot average).

Oscilloscope averaging was crucial to the experiment. As illustrated in Fig. 23, averaging removed random noise that, if looked at from shot-to-shot, obscured the signal contribution made by population changes. When acquiring rotational relaxation data, the oscilloscope took a running average of 100 waveforms. With the Nd:YAG operating at 10 Hz, this took 10 seconds. Increasing the number of waveforms in the average beyond 100 would have increased the possibility of the probe wavelength drifting off line center during the acquisition cycle.

Much of the noise in Fig. 23 is electrical, most of it coming from the YAG's flash lamps. Experiment showed that the flash lamp noise retained a consistent temporal profile. After tuning the probe laser off resonance, the noise profile was saved in the computer's memory. Since the noise did not depend on the probe laser's wavelength or

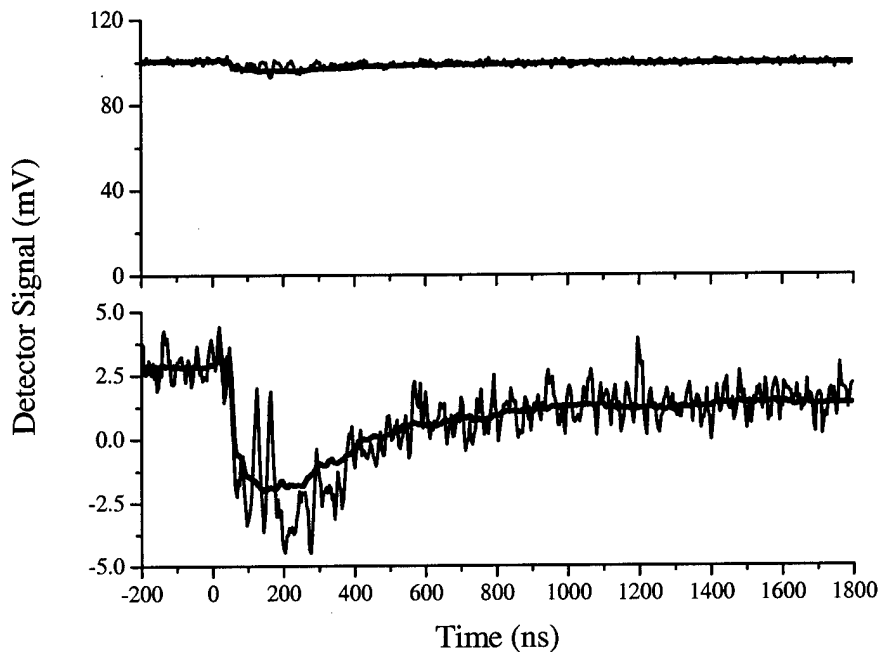


Figure 23. Oscilloscope averaging and offset abilities. The upper graph shows the full signal from the InSb detector. The lower graph shows a similar signal when the DC content is removed and gain is increased. The red curves show the oscilloscope trace when the scope averages 100 traces.

intensity, its profile did not change when the probe was tuned back onto resonance. Subtracting the noise pattern stored in the oscilloscope's memory from the traces displayed on the screen removed the noise contributed by the flash lamps. Figure 24 shows the effect of removing the electrical noise from the data.

Another source of noise was the 30% variation in the OPO pulse energy. To investigate whether averaging distorted the data, a model simulated a changing pump energy by randomly varying the excited state population up to $\pm 40\%$ about an average value. The predicted change in probe absorption was then tracked. Figure 25 shows the predicted transmission for the $J = 1, 4$, and 7 probes as a function of time when the $J = 4$ level is pumped. The black curve represents the intensity change associated with a single pulse of average energy. The red curve represents the average of 100 waveforms caused by 100 random-energy pulses (the average energy of the red curve's 100 random-energy

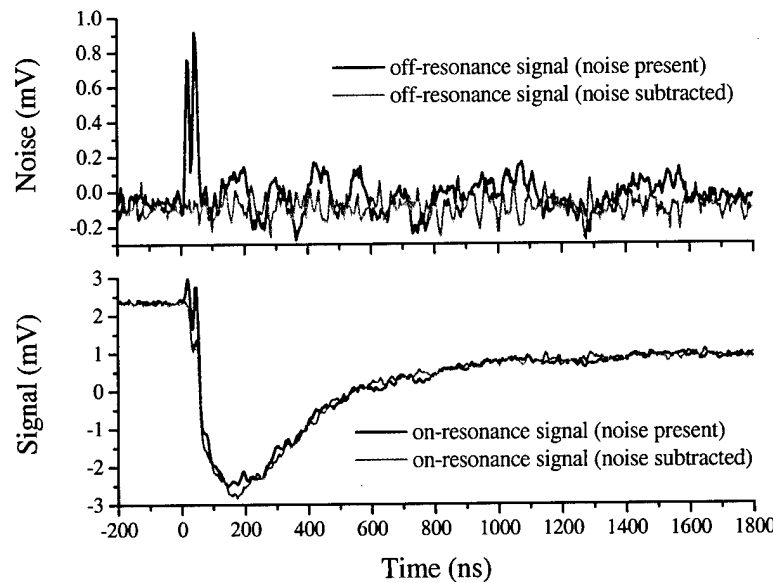


Figure 24. Oscilloscope noise subtraction. The top graph shows persistent electrical noise present when the diode is tuned off resonance. The systematic background noise is saved in the scope's memory. The lower graph shows the signal when the diode is tuned onto resonance with the noise still present. The orange curves in both cases show the effect of subtracting the noise saved in memory.

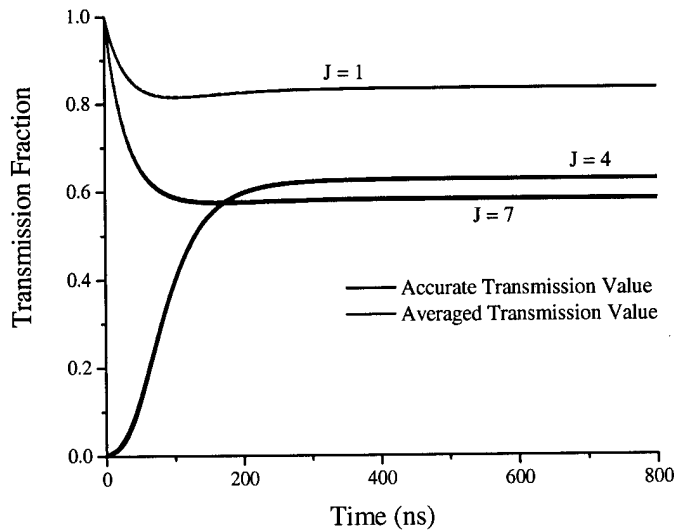


Figure 25. Legitimacy of averaging. A comparison between the predicted transmission of a single pump pulse with average energy and the average of 100 waveforms caused by 100 random energy pulses. The match is good, making it reasonable to use the averaged waveform on the oscilloscope.

pulses equals the energy of the black curve's single pulse). Such a good match shows that averaging is acceptable. A potentially better method of eliminating noise caused by pump energy fluctuations employs a special type of oscilloscope trigger called a runt. With runt triggering, the scope acquires data only when the peak detector voltage falls within a narrow window, effectively limiting data acquisition to OPO pulses with a constant energy. Runt triggering proved inadequate because the diode laser drifted off resonance during the time it took to collect enough oscilloscope traces.

Data Acquisition: Procedure

The first step in taking the data was to ensure the OPO was stable, optimally aligned through the pinhole, tuned onto resonance, and that the probe was directed into the InSb detectors. After the cell was filled with CO, the diode current was tuned until the oscilloscope waveforms showed excited-state CO absorbing the probe beam. Transmission through the monochromator verified that the probe was tuned to the J level of interest. With a transient absorption signal visible on the oscilloscope, the oscilloscope time base was set so the excited state population reached rotational equilibrium before the trace ended. After removing the DC component of the signal with a vertical offset voltage, maximizing vertical gain, and recording the noise waveform, the diode was tuned back onto resonance and the acquisition program started. Probe laser resonance was maintained by periodically adjusting the diode current in 15-microamp steps and watching for an improvement in probe absorption. Despite the 100-pulse averaging, a misstep in probe current was easily discernable. With the optimal current setting verified, the computer was manually triggered to retrieve and store the 5000-point oscilloscope trace. Acquisition was repeated until 16 waveforms were saved. Once the line center resonance measurements were complete, the probe wavelength was scanned across the absorption feature five times to measure the change in the excited-state absorption lineshape with time. Pressure, temperature, and transmitted energy were recorded manually since they did not change significantly during acquisition.

The CO pressure in the cell was typically kept around one torr. But when probing the pumped J level, the CO pressure was reduced to 0.15 torr to avoid ringing. The CO pressure was raised to 2 torr when probing J levels with low equilibrium population fractions to increase the excited state population at rotational equilibrium.

DATA ACQUISITION: DATA MANIPULATION

In an ideal experiment, the population changes in all the $v = 2$ rotational levels would be simultaneously measured. Since this is not possible with the equipment available, the J-level populations were measured individually and gathered at the end. This introduces two problems: adequately measuring the pumped and thermally improbable J levels requires varying the CO pressure which changes the relaxation rates; and taking data at different times means accounting for changes in the OPO's average pulse energy which fluctuated hour-to-hour.

Different Pressures

The best way to reduce detector ringing when probing the pumped J level was to reduce the CO pressure. Reducing the pressure lessened the depth of the step-like drop in probe intensity at the detector and slowed relaxation so the ringing damped out before many molecules left the pumped level. On the other hand, the CO pressure was increased to create a detectable population density when probing a J level sparsely populated at room temperature. Increasing or decreasing the pressure changes the collision rate. Fortunately it does not change the rate constants. Just as rolling a die more often does not change the odds of rolling a two on any particular roll, varying the pressure to increase or decrease the number of collisions a molecule undergoes does not alter the probability that the molecule makes a rotational energy change during any single collision. To relate data taken at the same temperature but at different pressures, the time scale was converted to a collision scale so that the populations became a function of collision number instead of time. Dividing the experimental time by the mean time between collisions (as given by

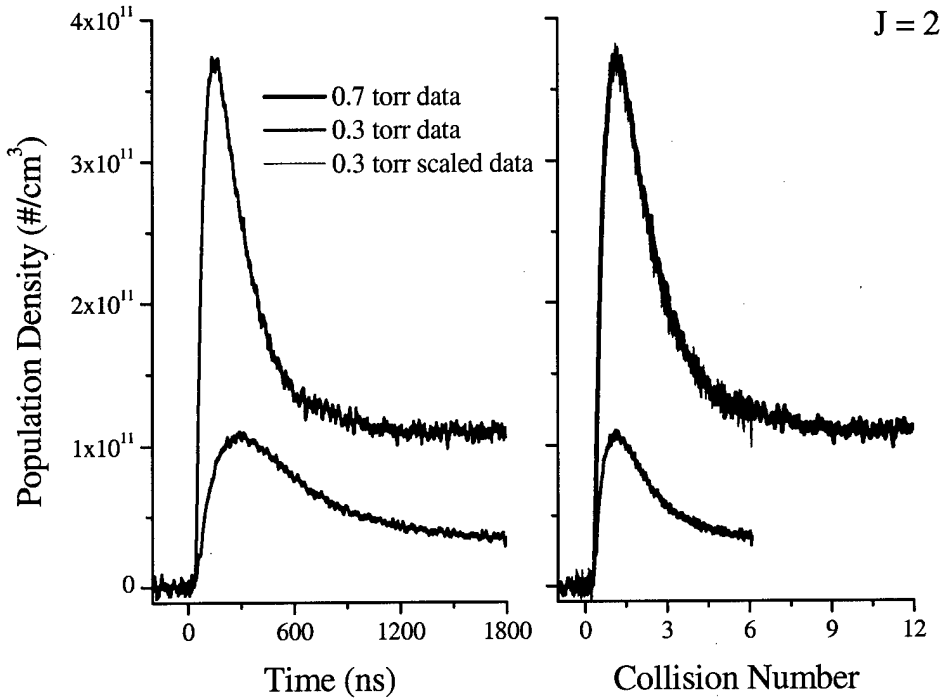


Figure 26. Scaling data taken at different pressures The data on the left shows the population change in $J = 2$ at two different pressures after a $J = 0$ pump. The same data is plotted on the right as a function of collision number. The green curve is the 0.3 torr data multiplied by 3.45.

the inverse of the collision frequency) converts the time scale into a collision scale. Copeland and Crim used this technique when tracking rotational level population changes in HF and DF at different pressures [42].

Figure 26 shows the population change in $J = 2$ after a $J = 0$ pump at two different pressures. Both sets of data were taken with the same oscilloscope time base and sample frequency. As the left side of Fig. 26 illustrates, changing the CO pressure changes both the rate of rotational relaxation and the number molecules excited into $v = 2$. The right side shows the same data on a hard-sphere collision number scale. To compare the two curves further, the discrepancy in absorbed pump energy caused by changing the CO pressure must be taken into account.

Pump Energy Fluctuations

Multiplying the blue 0.3 torr data on the right-hand side of Fig. 26 by a factor of 3.45 gives the overlapping green curve. The question is whether multiplying a measured number density by a constant factor to simulate a greater excited state number density preserves the true rate of rotational relaxation. The answer—hinted at by the near-perfect fit of the 0.3 torr data to the 0.7 torr data—is yes. Multiplying the 0.3 torr number density by 3.45 is equivalent to increasing the pump energy to raise the excited-state number density. Provided ground state CO remains the dominant collision partner³, increasing the number of excited molecules does not alter the probability that an individual molecule makes a rotational energy change when undergoing a collision. Returning to the dice-rolling analogy, just as rolling four dice at a time instead of one does not change the probability that an individual die comes up showing a two, increasing or decreasing the excited-state number density by increasing or decreasing the pump energy does not change the rate of rotational relaxation. The match between the scaled 0.3 torr data and the 0.7 torr data shows that scaling the population density by a constant factor allows one to account for different absorbed energies without skewing the rate constant information. It also shows that 0.84 systematic error mentioned earlier does not affect the relaxation measurements.

After collecting a full manifold of J-level probe data for a given pumped J-level, the experimenter must scale the data so that it resembles what one would have acquired if all J-levels were probed simultaneously. Correct scale factors are found by applying Eq. (1.17) once the excited molecules reach rotational equilibrium. A prescription for finding the scale factors follows:

- 1) Choose the J level with the best signal-to-noise ratio. For example, J = 7.
- 2) Find the J = 7 population density when the CO has reached rotational equilibrium.

³Typical ground and excited state number densities are 10^{16} and 10^{12} molecules/cm³ respectively.

- 3) Use Eq. 1.17 to find the total excited state population density N_T based on the $J = 7$ equilibrium density.
- 4) Find the population density of all the other J levels under conditions of rotational equilibrium.
- 5) Divide the product of N_T and the J level's equilibrium probability by that J -level's measured equilibrium population value to get the scale factor.

EXPERIMENTAL IMPROVEMENTS

While the equipment performed well during the experiment, improvements could be made. The problems which affected the data most were drift in the OPO wavelength and multimode output from the probe laser.

The simplest way to improve the stability of the OPO wavelength is to replace the laboratory air-conditioning unit as the diode laser controlling the OPO wavelength is sensitive to the laboratory temperature. When the air conditioning turns on or off, the changing temperature drives the diode off resonance, making wavelength adjustments necessary every few minutes. To make line center resonance more recognizable, a vacuum and CO supply should be attached to the resonance cell so pressure can be lowered or raised according to the strength of the pump transition. If possible, the size of the wavelength step made by the diode controller should be decreased to keep the subsequent change in the OPO's wavelength from stepping over peak resonance. Finally, a locking circuit could be attached to the diode controller if a Lamb dip can be produced at line center [54]. By bypassing the pinhole filter and sending high-energy, saturating pulses through a heated CO cell it may be possible to produce a Lamb dip narrower than the lineshape's peak.

The most troublesome problem associated with the probe was the near-resonant multi-mode output which added the unwanted I_{DC} signal. A confocal Fabry-Perot etalon with a 1.5 GHz FSR and a finesse of 30 would reveal the relative intensity of the non-resonant modes not filtered by the monochromator. One could also measure I_{DC} directly by absorbing the resonant portion of the beam. Complete or near-complete absorption

calls for using a multi-pass cell (a Herriott cell or White cell) to increase the path length of the probe through the excited CO. With an excited-state number density of 10^{11} molec/cm³ at equilibrium (the pump creates a number density of $\sim 3 \times 10^{12}$ molec/cm³), a 100-m path length is needed to absorb 95% of the incident probe beam. Considering the reflection losses and the difficulty associated with aligning a highly divergent, weak, invisible beam, the Fabry-Perot etalon is the best method for measuring I_{DC} . It would be worthwhile replacing the CO cell with a conservative 10-meter-path-length multi-pass cell to improve the signal-to-noise ratio on weak transitions. Reflecting the pump beam back through the multi-pass cell would increase the excited-state number density provided one could still avoid ASE.

To make the probe easier to align through the system, an alignment kit should be purchased from the probe manufacturer. The kit co-aligns the output of a visible diode laser with the output of the lead-salt diode. A more sensitive IR camera would also simplify the alignment.

Though the probe laser is tunable from 4.6 to 5.0 microns, output at either extreme is often weak and unstable. Diodes with greater output and narrower range can be purchased for less than \$2k. Purchasing several of these diodes would allow additional CO levels or other molecules to be investigated.

CHAPTER 4: EXPERIMENTAL RESULTS

Before rotational populations could be extracted from the probe absorption data, the effect of vibrational loss and lineshape relaxation on absorption had to be measured. This chapter gives the details and results of experiments measuring vibrational, lineshape, and rotational relaxation. It also shows the model fits to the data.

VIBRATIONAL LOSS FROM $V = 2$

While vibrational loss is slow compared with the rate of rotational relaxation, it is fast enough to affect the rotational populations. The red curve in Fig. 27 shows the population in $J = 2$ after an R13 pump. Steady population loss after ten hard-sphere

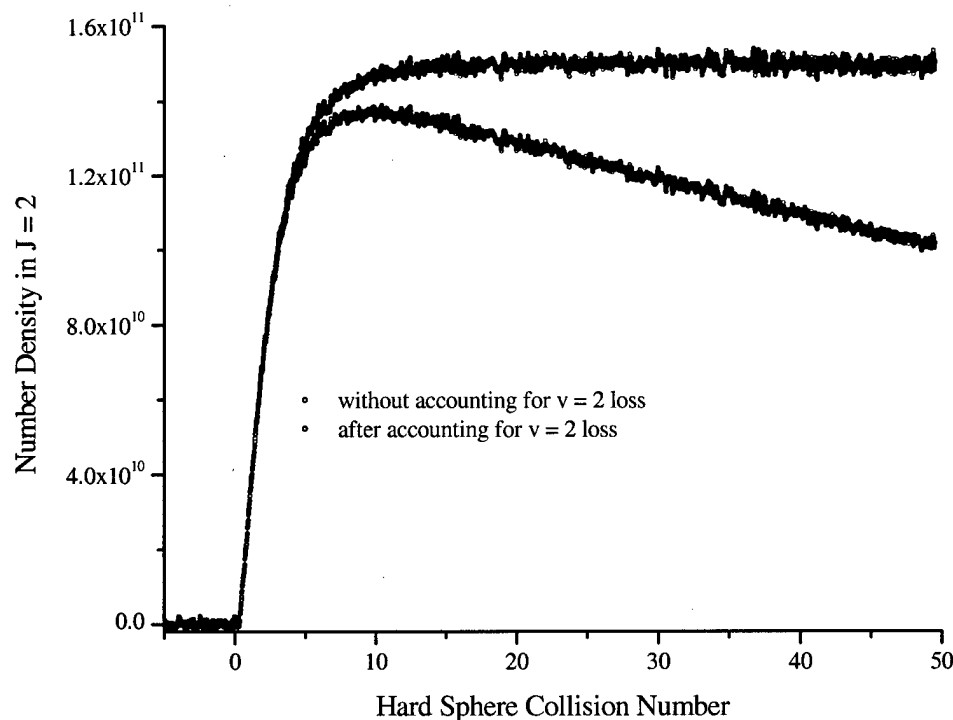


Figure 27. Vibrational relaxation. This data shows the effect of vibrational relaxation. Loss from $v = 2$ causes the downward slope in the red curve. The blue curve shows the data after accounting for the $v = 2$ loss.

collisions is caused by vibrational relaxation. The blue curve shows the same data when vibrational relaxation is removed using Eq. (2.2). In Eq. (2.2), the rate constant k_{loss} governs vibrational loss:

$$-\frac{1}{e^{-k_{\text{loss}}Mt}} \frac{8\pi}{A\lambda^2 L} \ln \left[\frac{I(t)}{I(0)} \right] = S(v, t) \sum_m \alpha_{j,j'}(m) N_{j,m}(t). \quad (2.2)$$

With the ratio of ground state and excited molecules at 10^4 to one, the dominant collision partner for the excited $\text{CO}(v=2)$ was $\text{CO}(v=0)$, making the expression in Eq. (4.1) the primary pathway for vibrational energy loss:

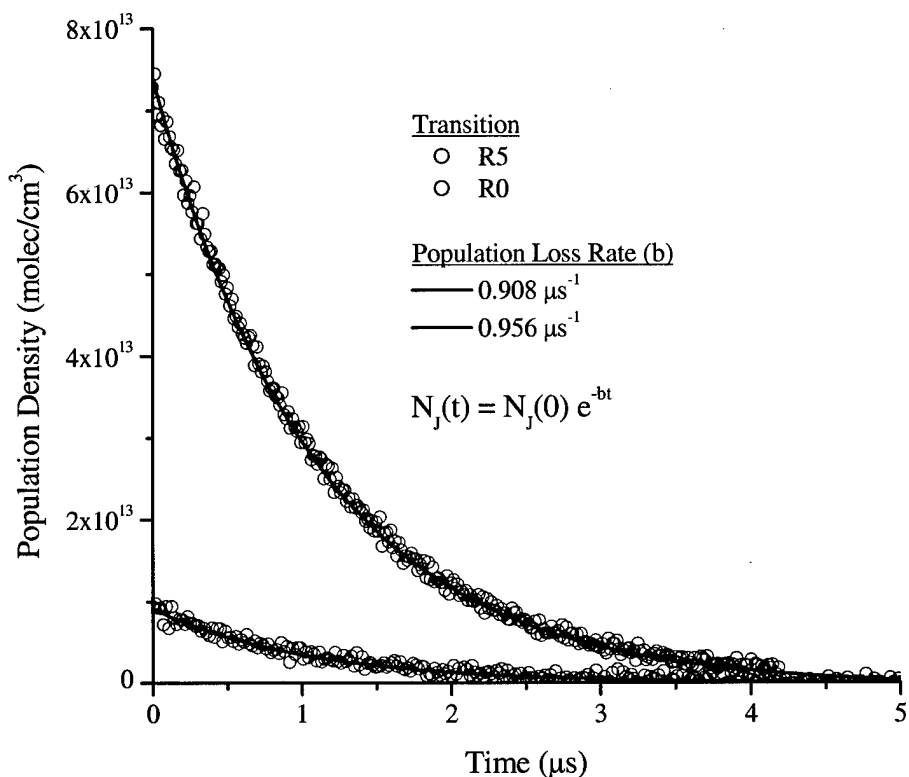
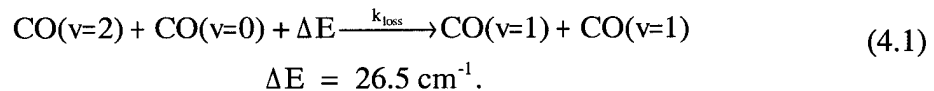


Figure 28. Sample of vibrational relaxation data.

To determine k_{loss} , vibrational relaxation out of eleven rotational levels was measured. Figure 28 shows typical vibrational-loss data. It also shows the exponential-decay fits to the data. Table 8 summarizes the experiment including weighting factors. The weighting factors are based on the inverse square of a fit's 95% confidence interval and reflect the noise associated with each measurement. The weights are normalized so their sum equals the number of data points. Figure 29 plots the weighted rates vs. CO pressure. The slope of the line joining the rates gives $k_{\text{loss}} = 8.96 \pm 0.53 \times 10^{-2} \text{ torr}^{-1} \mu\text{s}^{-1}$ or, in other units, $2.71 \pm 0.16 \times 10^{-12} \text{ cm}^3/\text{molec}\cdot\text{s}$. This compares favorably with the value of $2.73 \times 10^{-12} \text{ cm}^3/\text{molec}\cdot\text{s}$ calculated by Billing [21].

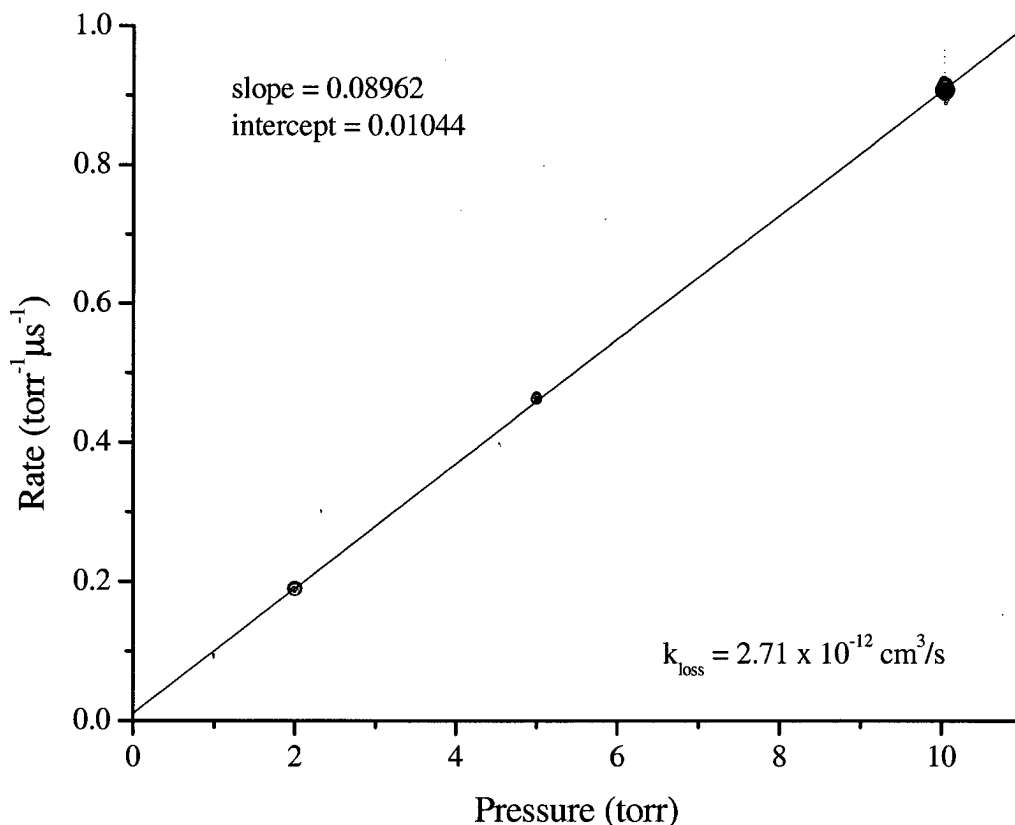


Figure 29. Weighted fit to vibrational relaxation data. The plot shows the vibrational loss rates measured at different pressures. The line was fit to the weighted data in Table 4.1. In the figure, the larger the symbol the greater its weight.

Table 8. Vibrational relaxation data. The data was taken at 292K.

Transition	Pressure (torr)	Rate (μs^{-1})	Weight	Transition	Pressure (torr)	Rate (μs^{-1})	Weight
R0	10.0	0.9564	0.0364	R7	10.0	0.8947	1.0408
R0	10.0	0.9471	0.0468	R7	10.0	0.9060	1.0871
R0	10.0	0.9656	0.0802	R7	2.0	0.1893	0.6885
R1	10.0	0.9333	0.1413	R7	2.0	0.1863	1.1395
R1	10.0	0.9215	0.1628	R7	2.0	0.1866	1.1668
R1	10.0	0.8992	0.1361	R8	10.0	0.8926	0.3200
R2	10.0	0.9186	1.3139	R8	10.0	0.8878	0.3800
R2	10.0	0.9202	1.4152	R8	10.0	0.9148	0.3593
R2	10.0	0.9178	1.3468	R8	5.0	0.4722	0.2268
R3	10.0	0.9103	1.2386	R8	5.0	0.4642	0.4809
R3	10.0	0.9082	1.9108	R8	5.0	0.4589	0.6257
R3	10.0	0.9120	2.1181	R8	2.0	0.1857	0.3958
R4	10.0	0.9050	1.4391	R8	2.0	0.1853	0.4275
R4	10.0	0.9093	1.6141	R8	2.0	0.1854	0.3950
R4	10.0	0.9159	1.9699	P10	10.0	0.9130	0.7511
R5	10.0	0.9045	2.1245	P10	10.0	0.9064	1.2252
R5	10.0	0.9080	2.6434	P10	10.0	0.9128	1.8518
R5	10.0	0.9093	1.8828	P10	10.0	0.9146	1.6908
R6	10.0	0.9121	1.0707	P10	5.0	0.4671	1.1532
R6	10.0	0.9092	1.3441	P10	5.0	0.4630	1.3025
R6	10.0	0.9047	1.6228	P10	5.0	0.4627	1.5384
R6	2.0	0.1889	1.6999	P12	10.1	0.9158	0.3801
R6	2.0	0.1899	1.9959	P12	10.1	0.8994	0.5078
R6	2.0	0.1891	1.8257	P12	10.1	0.9033	0.7264
R6	1.0	0.0942	0.3239	P12	10.1	0.9082	0.6482
R6	1.0	0.0906	0.2255	P12	5.0	0.4636	0.5036
R6	1.0	0.0905	0.2607	P12	5.0	0.4630	0.5252
R7	10.0	0.9003	0.8601	P12	5.0	0.4670	0.6119

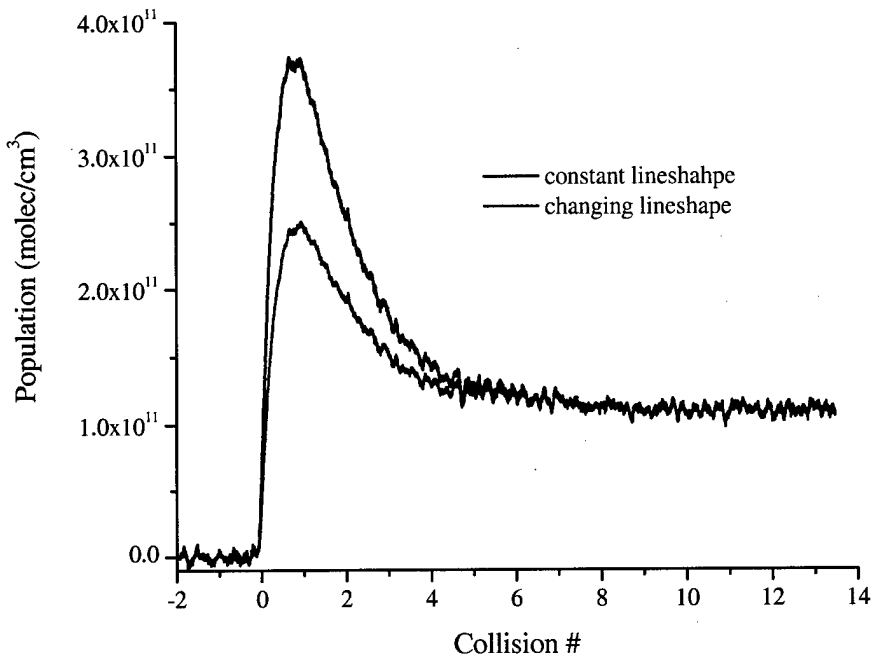


Figure 30. The influence of lineshape relaxation. The curves show the calculated population in $J = 2$ following a P1 pump when the changing line shape is accounted for and when it is not. In the constant line shape case, the room-temperature Doppler lineshape was used.

LINESHAPE RELAXATION

Because the pump's bandwidth is narrower than CO's absorption linewidth, the molecules the pump excites into $v = 2$ have a sub-Doppler velocity distribution. The sub-Doppler distribution allows more excited molecules to absorb the probe than one would predict given the gas temperature. Without a time-dependent lineshape model to compensate for the enhanced absorption, the rotational populations calculated using Eq. (2.2) would be inaccurately high. Figure 30 shows how not compensating for the changing lineshape distorts the calculated $J = 2$ population following a P1 pump.

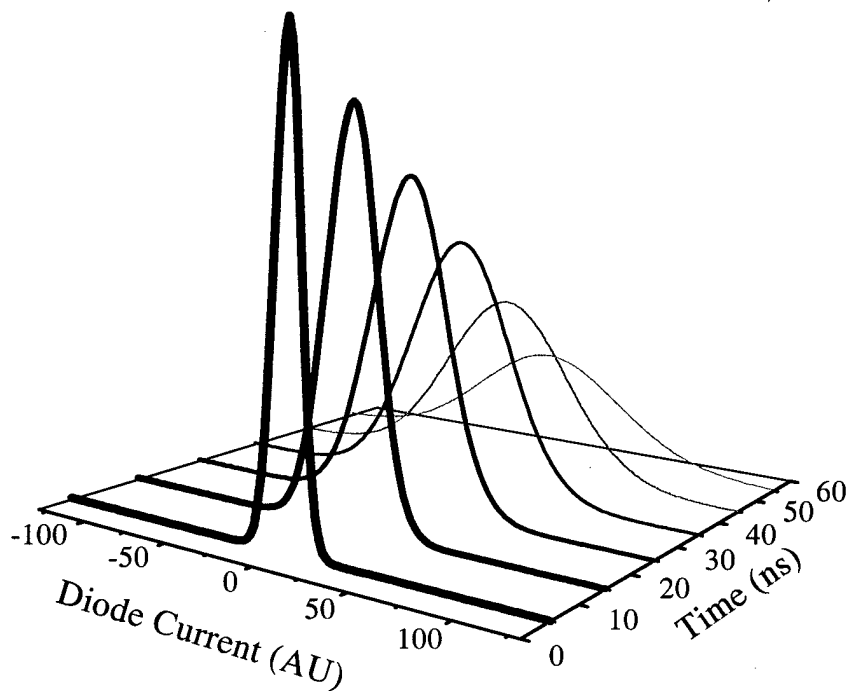


Figure 31. Simulated lineshape data: method 1. The plots show the results of an idealized experiment where the diode current that controls the probe wavelength is scanned rapidly across the absorption feature at different times.

The Experiment

A simple way to measure $S(v,t)$ would be to scan the diode's frequency (v) across the absorption transition at 10 ns intervals, beginning when the pump excites the molecules and ending when the molecules reach equilibrium. Figure 31 shows what the results of such an experiment would look like. Since no laser scans that fast, a more realistic experiment measures the change in probe absorption with time at a fixed frequency. Repeating the measurement at different frequencies generates the data in Figure 32. The simulated data in Figure 32 reveals the lineshape provided enough frequencies are included. Lineshape relaxation was measured using this second method: a computer stepped the diode frequency across the transitions and an oscilloscope recorded the absorption.

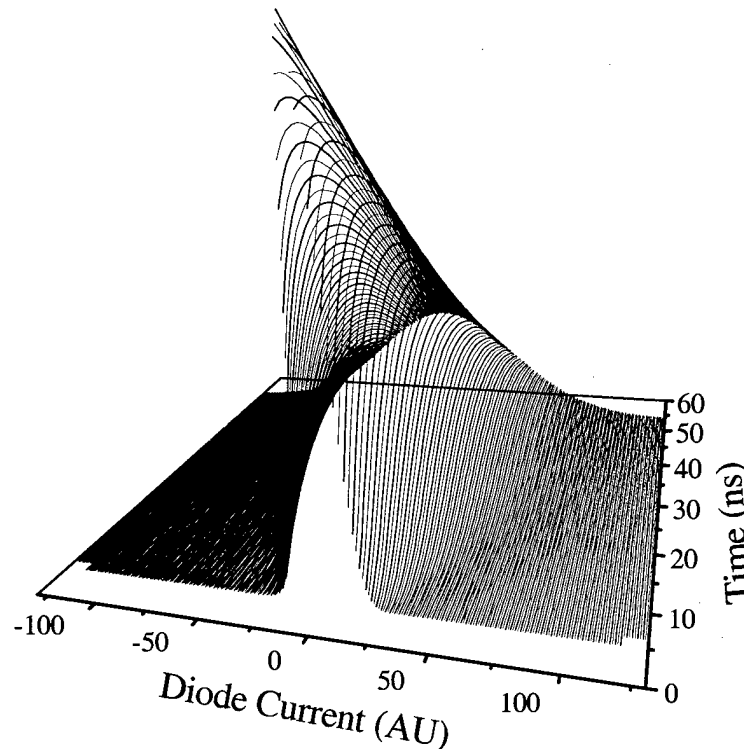


Figure 32. Simulated lineshape data: method 2. The graph shows the results of an idealized experiment where the wavelength (current) is fixed and the population change is measured.

Equipment Limitations

Measuring the lineshape required adapting to the equipment's limitations. The most troublesome was the pump drifting off line-center resonance. An off-resonant pump creates excited molecules whose peak resonant frequency is displaced from the normal resonance frequency. Though collisions eventually shift the peak back, the shift, combined with lineshape broadening, results in a measured linewidth that deceptively remains constant. The best way to avoid this problem and ensure the data was taken with the pump at line center was to repeat the experiment four or five times.

The pump was not the only problem. Every few minutes the diode laser mode hopped, disrupting the measurement (see Fig. 16). Stepping the diode quickly across the transition helped avoid mode hops. Since transferring the data from the oscilloscope to

the computer took time, the oscilloscope was limited to 500 samples per trace. Even then the shortest time achieved between frequency steps was one second.

The time between steps limited how much oscilloscope averaging one could justify. With the OPO operating at 10 Hz, setting the oscilloscope to average fifty traces meant each stored waveform was the combined result of five frequency steps. On the other hand, averaging only ten traces significantly increased signal noise. As a compromise, scope averaging was set to twenty. Averaging twenty traces reduced the noise and restricted the number of frequency steps contributing to a waveform. Including two frequency steps in the data did not induce much error since it helped offset current jitter. Jitter is the difference between the current value set by the diode controller and the current actually sent to the diode (current was the physical quantity changed by the diode controller—changing the current changed the frequency). During a scan, the computer increased the diode current in $5\text{-}\mu\text{A}$ steps, and on average the current changed in $5\text{-}\mu\text{A}$ steps. But the true current could vary by as much as $15\text{ }\mu\text{A}$ from the set current. The actual current labeled the waveform files when they were transferred to the computer.

Frequency Calibration and the Pumped Levels

Converting from current to frequency required a calibration factor. Because this factor changed with diode temperature and age, each set of files had its own calibration determined by comparing the data's equilibrium linewidth (measured in μA) to the theoretical linewidth (calculated in MHz). This method worked well unless probing the levels directly populated by the pump.

Probing pumped levels was difficult because detector ringing obscured the starting population, high initial populations with narrow linewidths absorbed too much of the probe, and relaxation left small equilibrium populations that did not absorb enough. As discussed in chapter three, a rapid and substantial change in intensity caused electronic ringing in the output of the InSb detectors. Lowering the pressure reduced the amplitude of the ringing relative to the size of the signal by decreasing the depth of the intensity drop associated with the pump. A lower pressure also slowed relaxation so any

remaining ringing damped out before significant population changes occurred. Unfortunately low pressure meant less pump absorption, fewer excited state molecules, and a worse signal-to-noise ratio. Too much absorption was also a problem. Even at pressures like 0.3 torr, the excited level's initial narrow linewidth and large population easily combined to absorb 100% of the resonant portion of the probe. When this happened the detector signal dropped and remained flat a short time before rising. Complete absorption hides the population dynamics, and the only practical way to prevent it was to reduce the pressure further.

Low pressures resulted in small equilibrium populations. Figure 33 shows the measured linewidths for the pumped $J = 0, 7$, and 14 levels. In the $J = 14$ case, noise rapidly overwhelms the linewidth measurements, and in the $J = 0$ case a small rise is seen before noise begins to dominate (the noise has been left off). The $J = 7$ pump was the only case where the linewidth of the pumped level was visible from start to finish. Without an equilibrium linewidth on which to base a calibration factor, an educated guess had to be made for the $J = 0$ and $J = 14$ starting linewidths. In the $J = 0$ case, the visible rise suggests further relaxation was swamped by noise so the initial linewidth value was set to 70 MHz—the same as $J = 7$. In the $J = 14$ case, the signal was noise-free long enough that the start of lineshape relaxation should have been visible. That it was not suggests the pump frequency was off line center. More evidence for this conclusion is given in the rotational relaxation section. The linewidth for $J = 14$ was assumed to start and remain at its equilibrium value since experience showed this gave rotational populations that made more sense with the rest of the data.

Measuring lineshape relaxation in levels not directly pumped was more straightforward excepting $J = 9$ and 15 . The lead-salt diode was unstable in the current and temperature regions where transitions probing $J = 9$ and 15 could be found. To use the rotational population data for $J = 9$, the $J = 9$ lineshape was assumed to follow the average of $J = 8$ and $J = 10$. For $J = 15$, a probe resonance was never found.

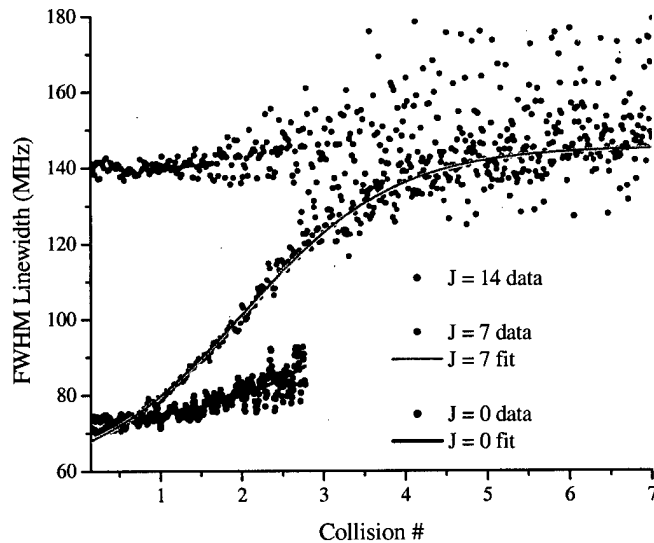


Figure 33. Linewidth data. The plots show the linewidth data for the pumped levels. The pumped level linewidths represent the worst cases in terms of signal to noise.

Analysis Procedure

The data in Fig. 33 are the result of calculations based on probe absorption measurements. Eq. (2.2) is the blueprint for those calculations. Eq. (2.2) shows that the probe intensity gives information about the product of lineshape and population. Because only the lineshape has frequency dependence, the population term acts as a time-dependent amplitude, leaving the linewidth unaffected by rotational relaxation (provided the amplitude does not sink into the noise). The following procedure describes how linewidths were deduced from the probe data.

Lineshape data was saved to the computer as a series of files, usually more than one hundred, with five hundred voltage data in each file. The voltages reveal the change in probe intensity over $\sim 2 \mu\text{s}$. The diode current, measured by the controller at the time the file was saved, labeled each file. All the files were imported as columns into a spreadsheet, labeled, and sorted in order of increasing current. Because probe power grew with current, the baseline voltage increased slightly from column to column. To remove the unwanted offset and establish the same baseline for all columns, the first fifty

points in a column—taken during the pre-trigger, zero-absorption portion of the oscilloscope trace—were averaged. That average was subtracted from the entire column, leaving all columns with a common starting value of zero. A single standard voltage manually recorded during the scan was then added to all columns.

The standard voltage contained the contribution from non-resonant modes (I_{DC}) which had to be estimated and removed. A survey of all the columns identified those few at line center. By averaging the final 50 data points in the line-center columns, the voltage at rotational equilibrium could be combined with absorbed pump energy to calculate I_{DC} . After removing I_{DC} , the lineshape-population product could be calculated for each column. By transposing the columns and rows, the populations as a function of diode current could be plotted at a single time, revealing the lineshape.

The lineshapes were transferred to an automated curve fitting program (TableCurve 2D) that fit the curves with a Gaussian. A Gaussian is the theoretical form of the lineshape at equilibrium. While the post-pump lineshape is likely not Gaussian, a Gaussian fits the lineshape as well as any other peak function. Figure 34 shows lineshape data and fits at three different times for the $J = 2$ level after a P1 pump. Figure 35 shows how the linewidth changes with time for the same level. The probe's 30-MHz bandwidth (also assumed to be Gaussian) was deconvolved from the measurements before calculating the linewidths.

The calculated error in the final value of the lineshape-population product was $\pm 12\%$. The uncertainty in the linewidths was less since theory set the measured equilibrium linewidth value. Uncertainty in linewidth was based on the experimental standard deviation σ among the four to five runs done per rotational level. Eq. (4.2) shows how the deviation was calculated.

$$\sigma = \frac{1}{\Delta v_{th}} \sum_i \sqrt{\frac{\sum_s [\Delta v_s(x_i) - \Delta v_{avg}(x_i)]^2}{N_s}} \quad (4.2)$$

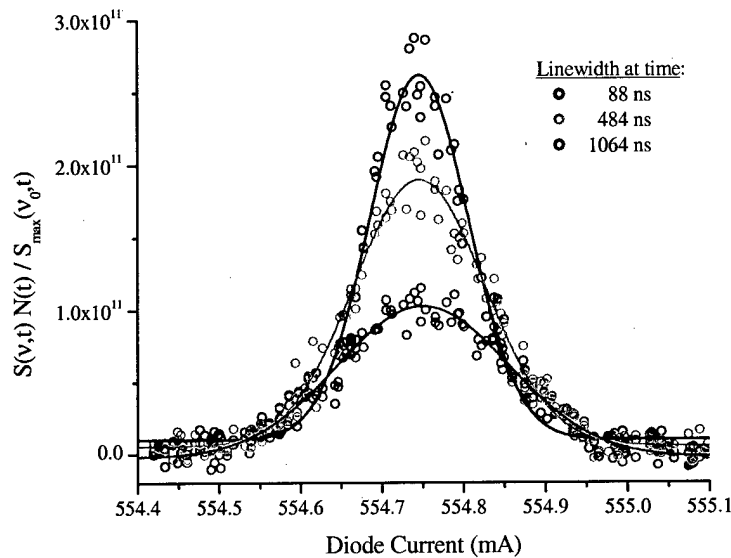


Figure 34. Lineshape data. The plots show measured lineshapes and gaussian fits. Rotational relaxation reduces the lineshape's amplitude but does not affect the linewidth.

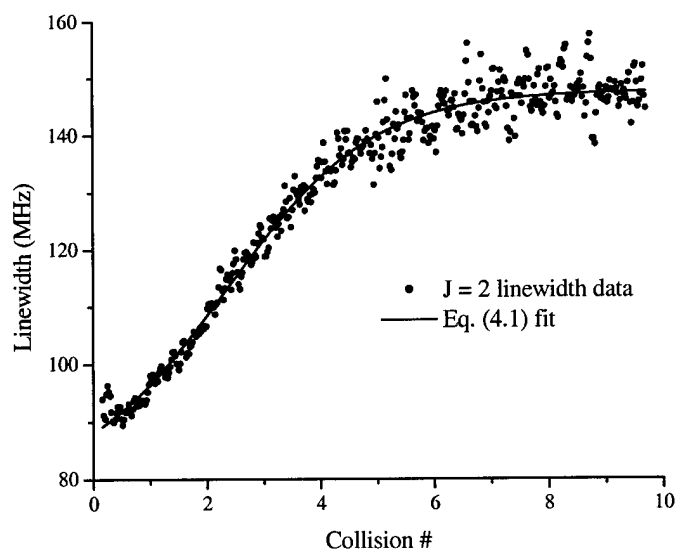


Figure 35. Linewidth vs. collision number. The data shows the absorption linewidth of $J = 2$ as a function of hard-sphere collision number. The absorption follows a P1 pump.

In Eq. (4.2), x_i is the collision number (time divided by the mean time between collisions), N_s is the number of scans across the transition, $\Delta v_s(x_i)$ is the linewidth measured at x_i during scan s , $\Delta v_{avg}(x_i)$ is the average of $\Delta v_s(x_i)$ over all s , and Δv_{th} is the equilibrium linewidth set by theory. Eq. (4.3) gives the parametric fitting function used to describe the change in linewidth

$$\Delta v_{fit}(x) = a + \frac{b}{1 + e^{-\frac{x-c}{d}}} \quad (4.3)$$

where (a, b, c, d) are the parameters. Eq. (4.3), called a sigmoid, was used as a convenience to describe linewidth relaxation in all levels. No effort was made theoretically to explain the form of $\Delta v_{fit}(x)$ since time was limited and the purpose of the research was to measure the rotational populations.

The Linewidth Data

The following tables and figures show the lineshape relaxation data and the fits to the data. The fits are included to allow the reader to gauge for himself their accuracy. Besides the fit coefficients, the tables give the fit figure-of-merit r^2 defined in Eq. (4.4).

$$r^2 = 1 - \frac{\sum_i [\Delta v_{avg}(x_i) - \Delta v_{fit}(x_i)]^2}{\sum_i [\Delta v_{avg}(x_i) - \mu]^2} \quad \mu = \frac{\sum_i \Delta v_{avg}(x_i)}{N_i} \quad (4.4)$$

The value of r^2 ranges from zero to one where $r^2 = 1$ is a perfect fit.

In Fig. 36, the linewidth for $J = 0$ was based on initial experimental values and the assumptions that relaxation is 80% complete after five collisions and 100% complete after ten collisions. Because the axes in Figs. 36 -42 change scale, Figs. 43 - 45 show the linewidth fits on the same scale.

Table 9. Linewidth fit parameters (P1 Pump)

J	a	b	c	d	r ²
0	67.596	79.037	2.461	0.852	0.940
1	107.920	38.068	2.479	1.341	0.912
2	78.588	69.243	2.358	1.286	0.976
3	94.466	53.603	1.838	1.503	0.980
4	90.657	57.796	1.247	1.829	0.947
5	104.111	43.982	1.842	1.535	0.937
6	51.051	98.393	-0.586	1.968	0.964
7	73.054	75.789	0.393	1.817	0.969
8	106.409	38.078	1.062	1.744	0.898
9*	93.465	50.801	-0.017	2.089	n/a
10	59.748	84.329	-1.880	2.513	0.801
11	115.013	28.709	0.959	2.191	0.657
12	127.667	76.406	-2.237	1.234	0.315
13	133.336	17.328	2.382	1.521	0.498
14-18	no measurable lineshape change				

*From the average of the J = 8 and J = 10 fits (not fit parameters).

Table 10. Linewidth fit parameters (R6 Pump)

J	a	b	c	d	r ²
0	126.527	21.325	1.452	2.646	0.153
1	38.113	108.369	-2.019	2.050	0.939
2	65.157	82.299	-0.610	2.045	0.938
3	99.406	49.097	1.282	1.649	0.943
4	27.509	120.795	-2.750	2.089	0.865
5	102.317	46.423	1.093	1.707	0.953
6	-344.326	492.714	-6.553	2.311	0.870
7	57.572	87.777	2.015	0.929	0.981
8	29.987	113.918	-2.697	2.138	0.882
9*	42.881	100.956	-2.072	2.191	n/a
10	49.544	94.221	-1.543	2.213	0.842
11	92.876	49.542	-1.016	2.125	0.606
12	129.643	14.752	2.923	1.224	0.786
13	112.910	37.455	1.172	1.594	0.716
14	104.819	40.295	-7.723	3.247	0.040
16	143.725	-3.994	1.454	-1.812	0.025
17	143.441	-7.387	0.430	-5.105	0.154
18	no measurable lineshape change				

*From the average of the J = 8 and J = 10 fits (not fit parameters).

Table 11. Linewidth fit parameters (R13 Pump)

J	a	b	c	d	r ²
0-6	no measurable lineshape change				
7	121.324	27.583	-0.200	0.896	0.374
8	131.420	12.604	1.157	0.672	0.308
9*	130.609	13.670	1.326	0.823	n/a
10	130.720	13.820	1.647	0.873	0.563
11	116.532	27.393	1.697	0.996	0.940
12	118.949	24.785	1.786	1.228	0.907
13	106.019	43.556	2.314	1.048	0.887
16	106.531	37.299	2.554	1.185	0.808
17	77.115	66.776	-0.888	2.242	0.415
18	93.437	49.432	-0.074	2.080	0.398

*From the average of the J = 8 and J = 10 fits (not fit parameters).

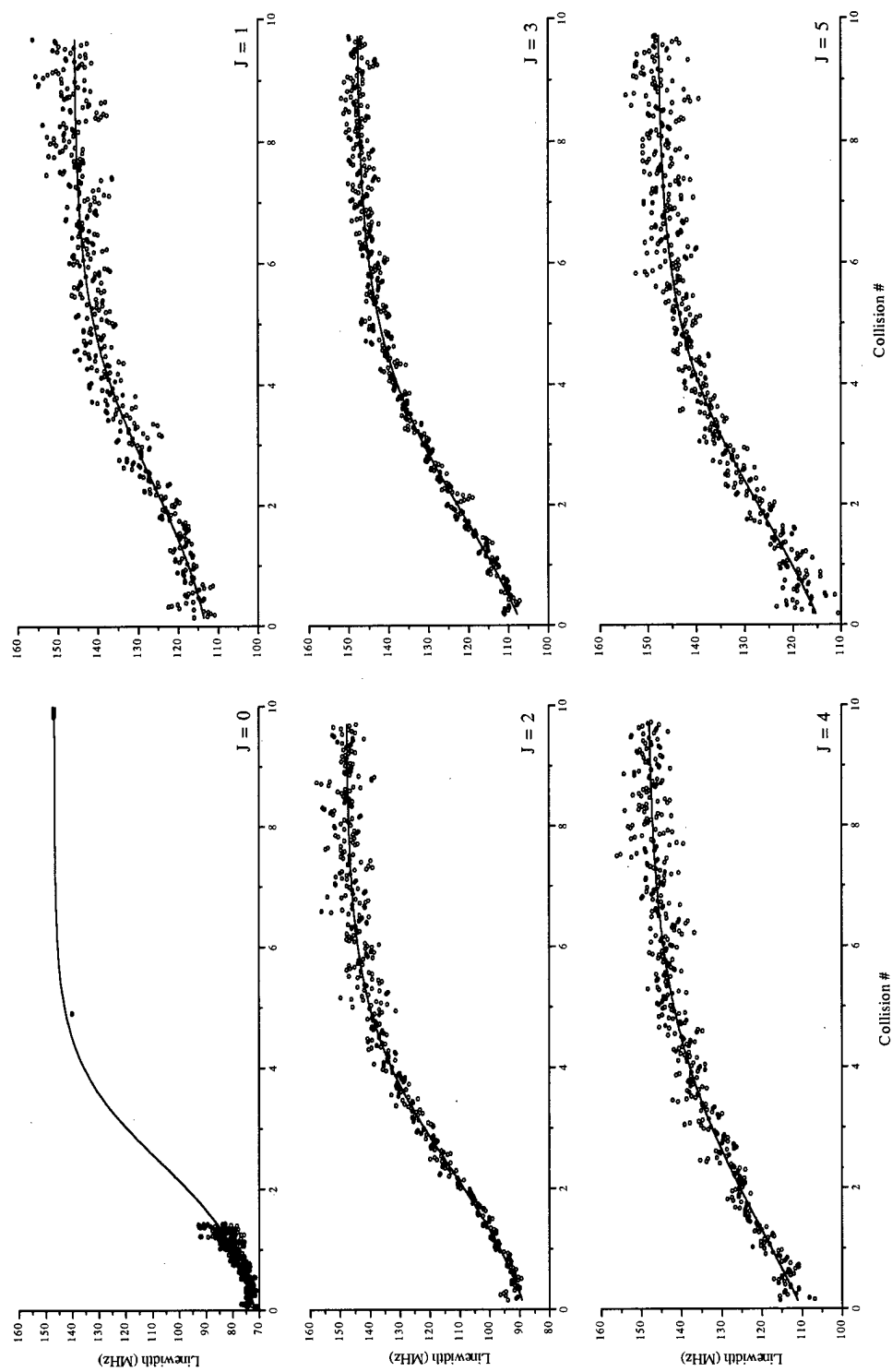


Figure 36. Linewidth relaxation: P1 pump ($J = 0$ to $J = 5$)

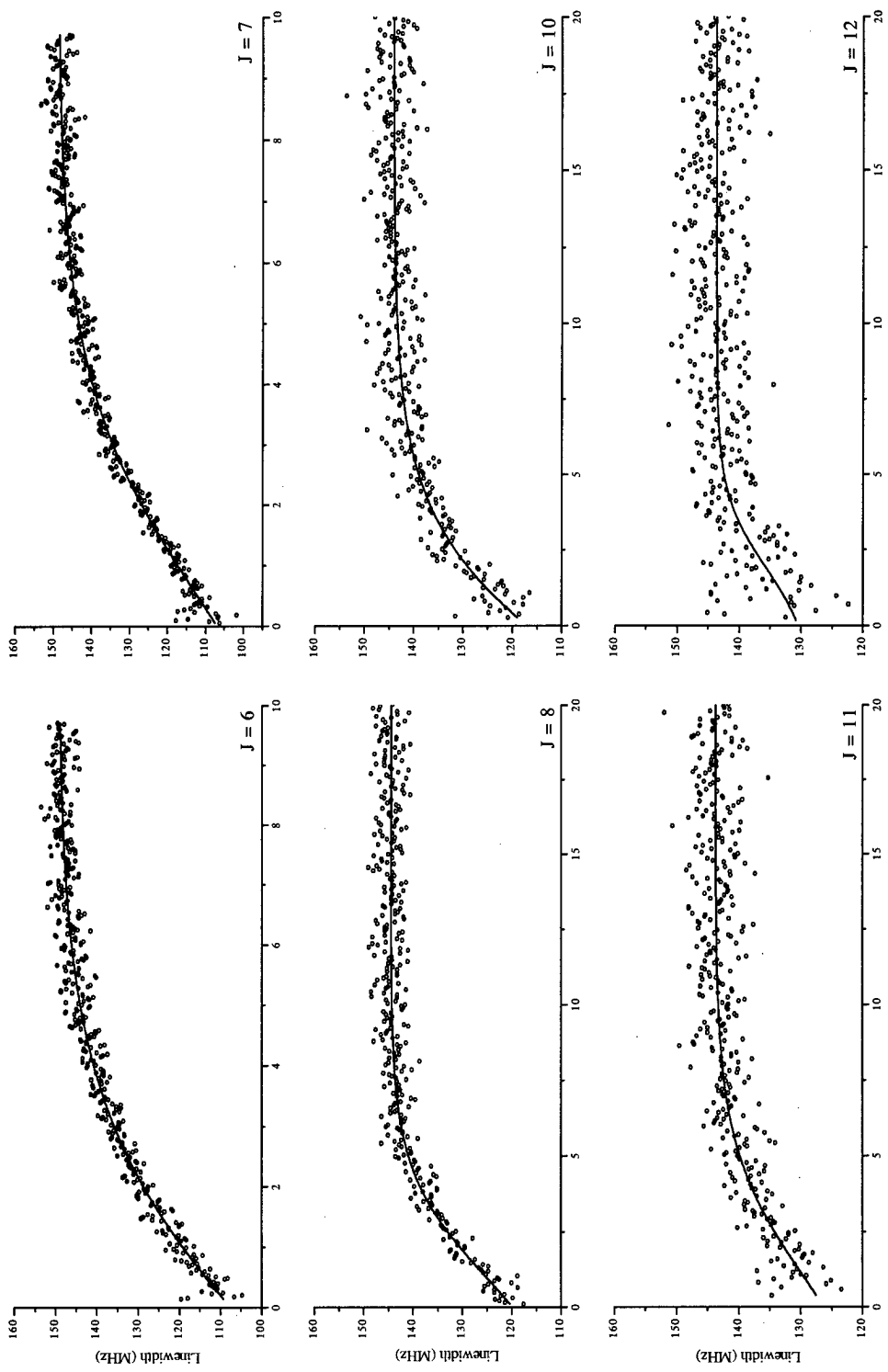


Figure 37. Linewidth relaxation: P1 pump ($J = 6$ to $J = 12$).

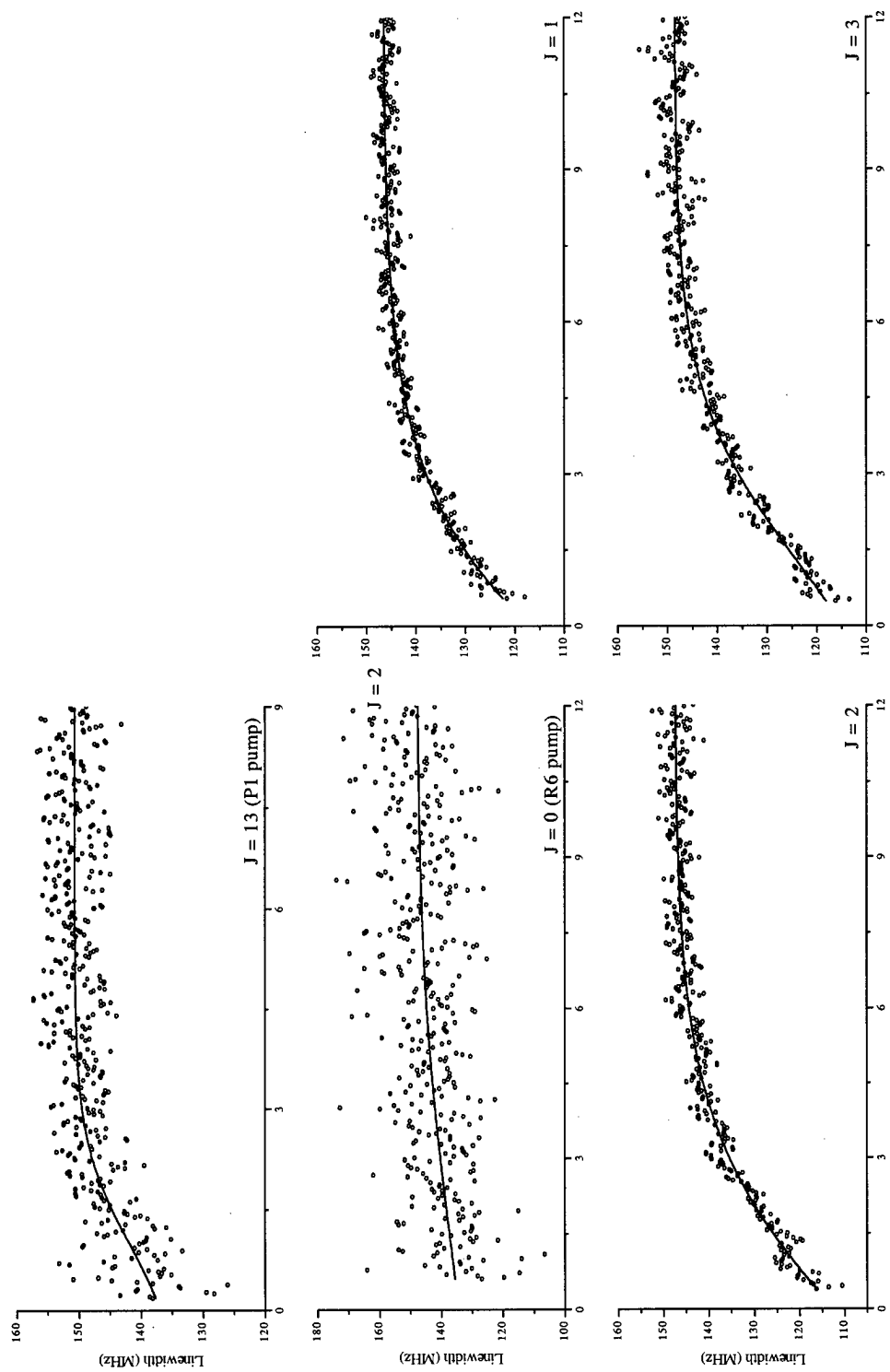


Figure 38. Linewidth relaxation: P1 pump ($J = 13$) and R6 pump ($J = 0$ to $J = 3$).

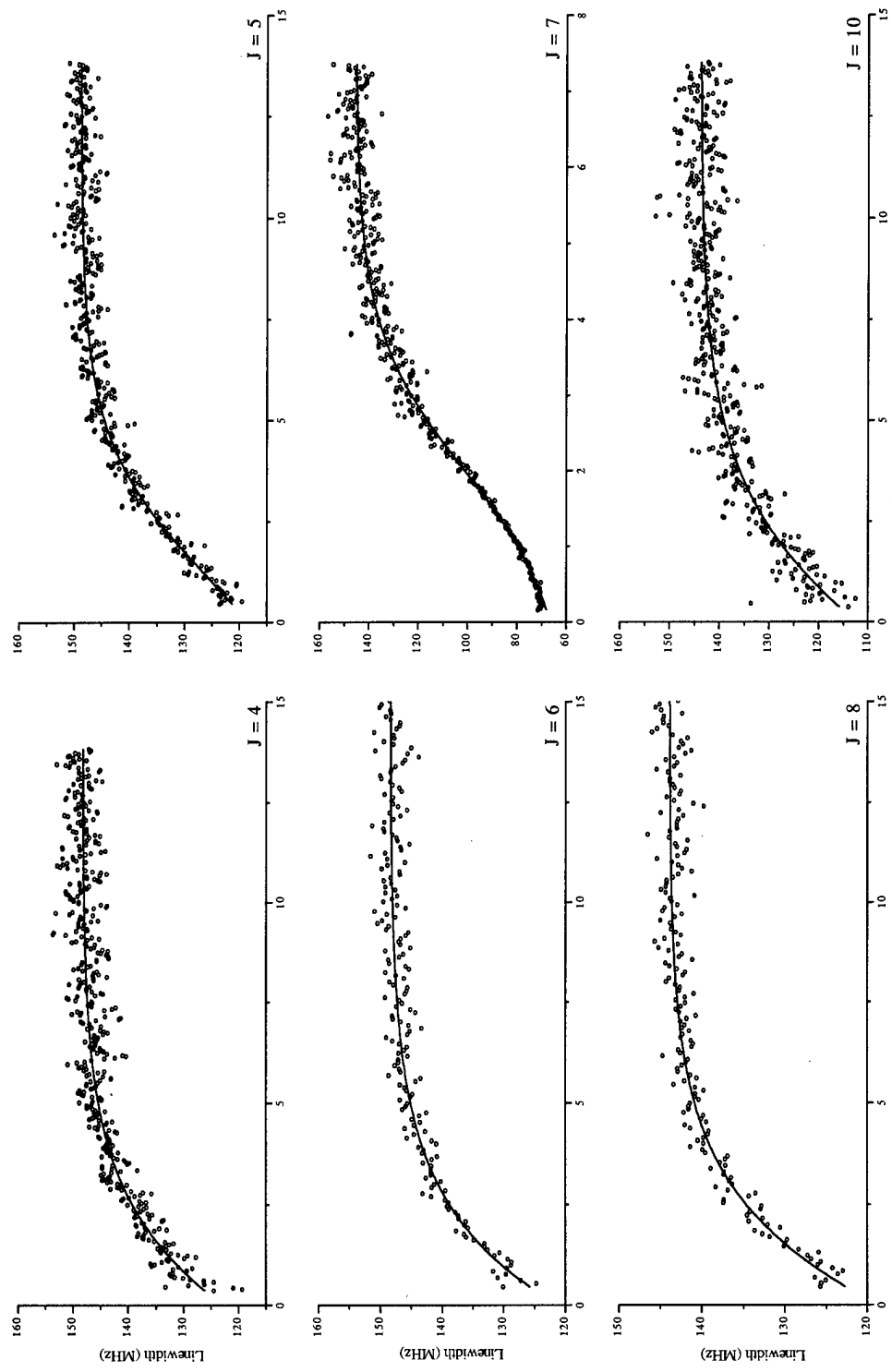


Figure 39. Linewidth relaxation: R6 pump ($J = 4$ to $J = 10$).

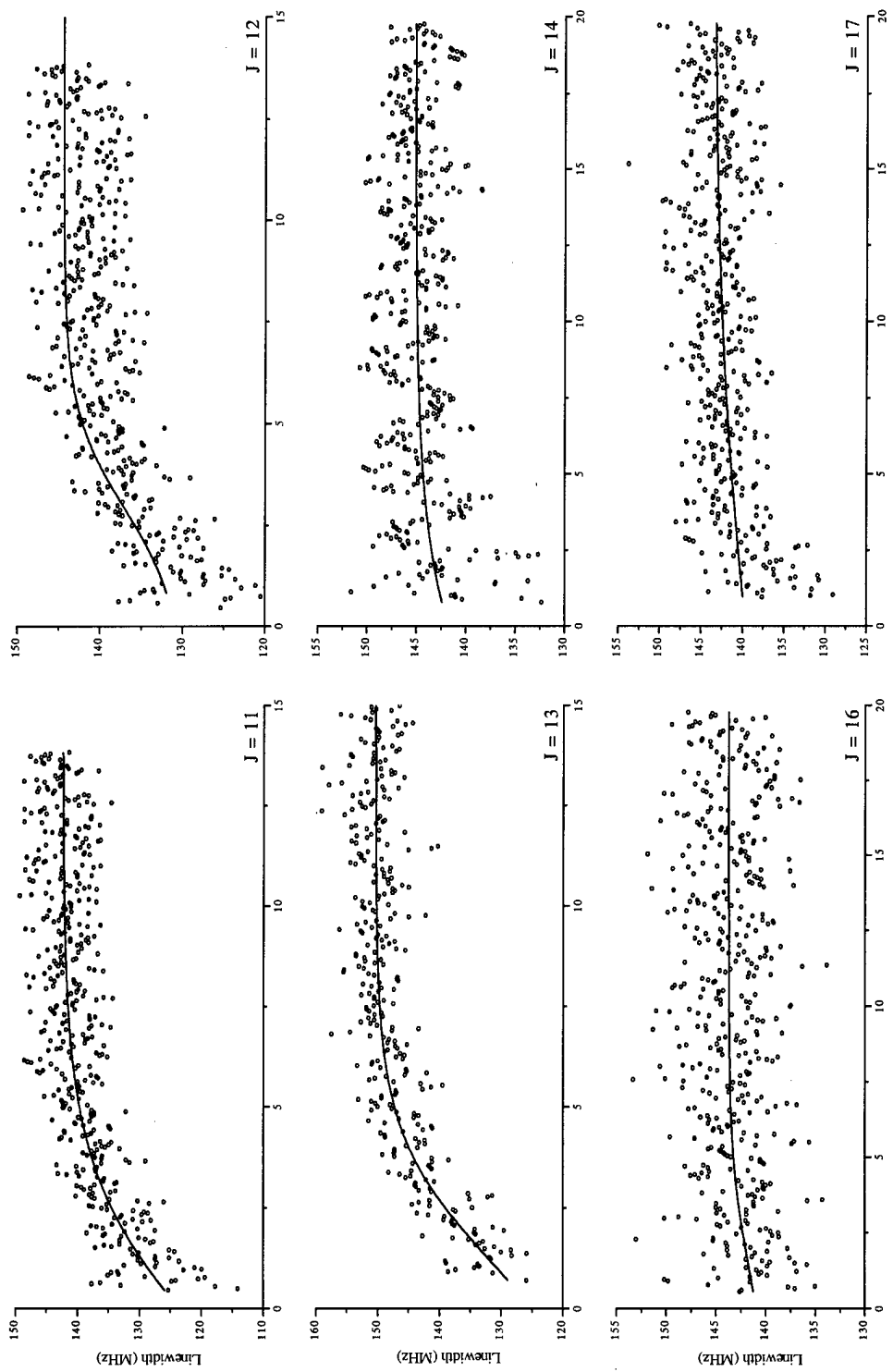


Figure 40. Linewidth relaxation. R6 pump: ($J = 11$ to $J = 17$).

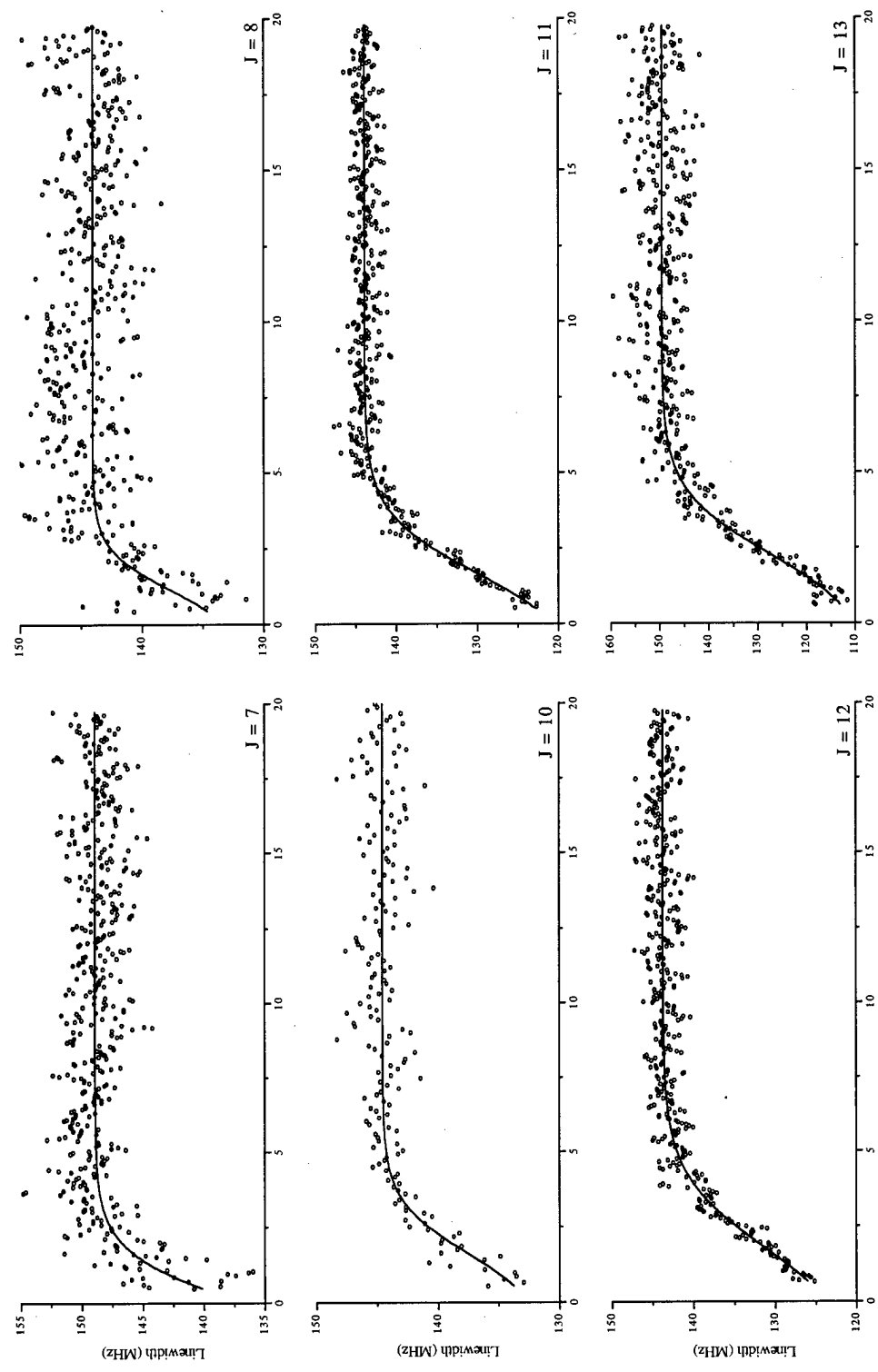


Figure 41. Linewidth relaxation: R13 pump ($J = 7$ to $J = 13$).

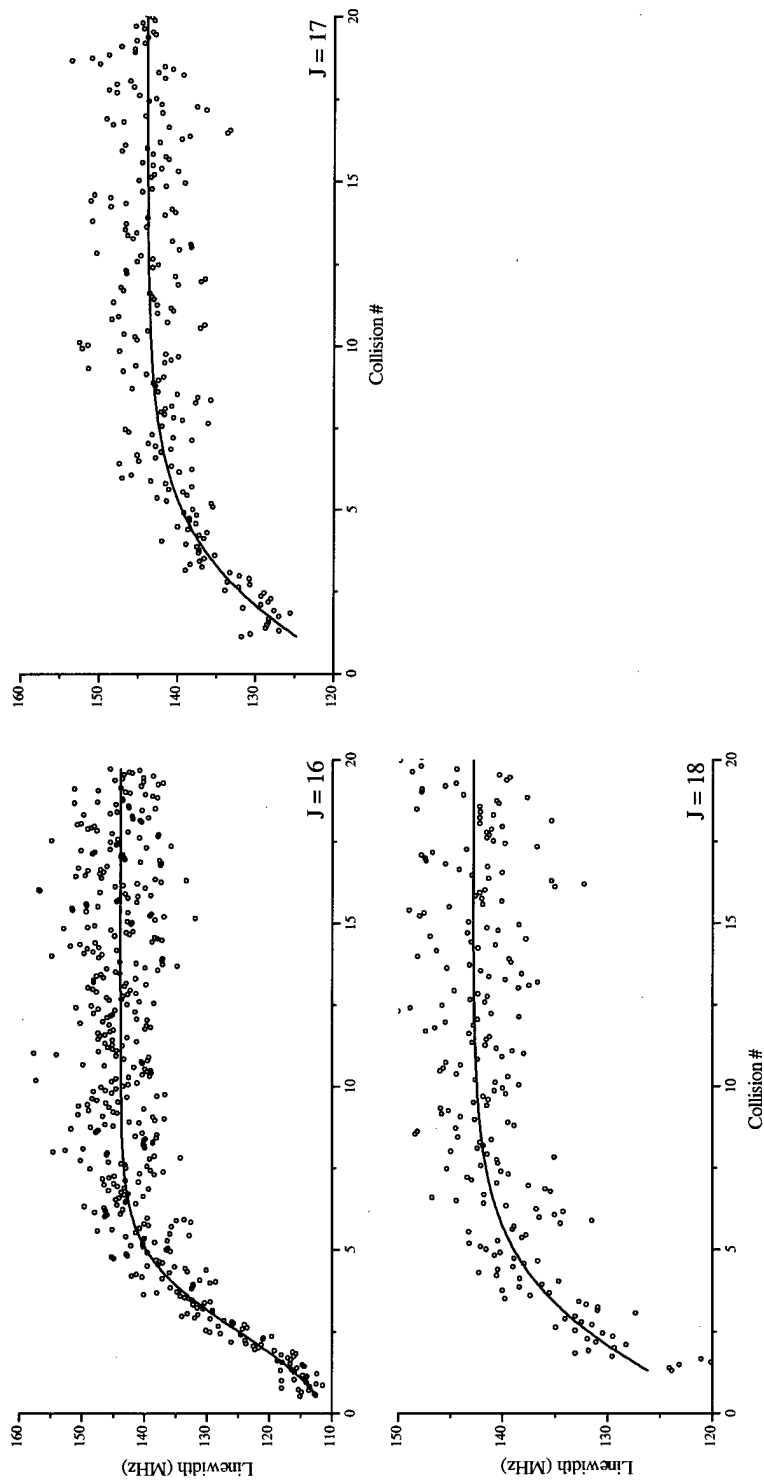


Figure 42. Linewidth relaxation: R13 pump ($J = 16$ to $J = 18$).

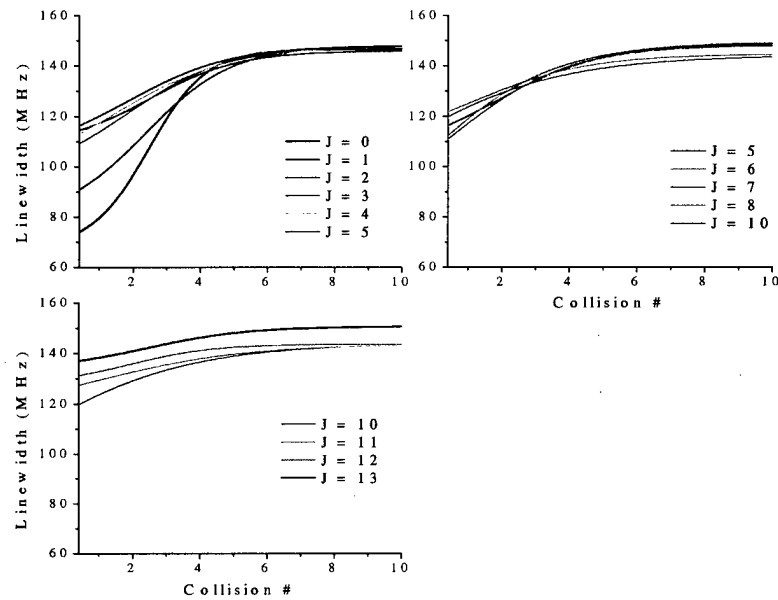


Figure 43. Linewidth comparison: P1 pump.

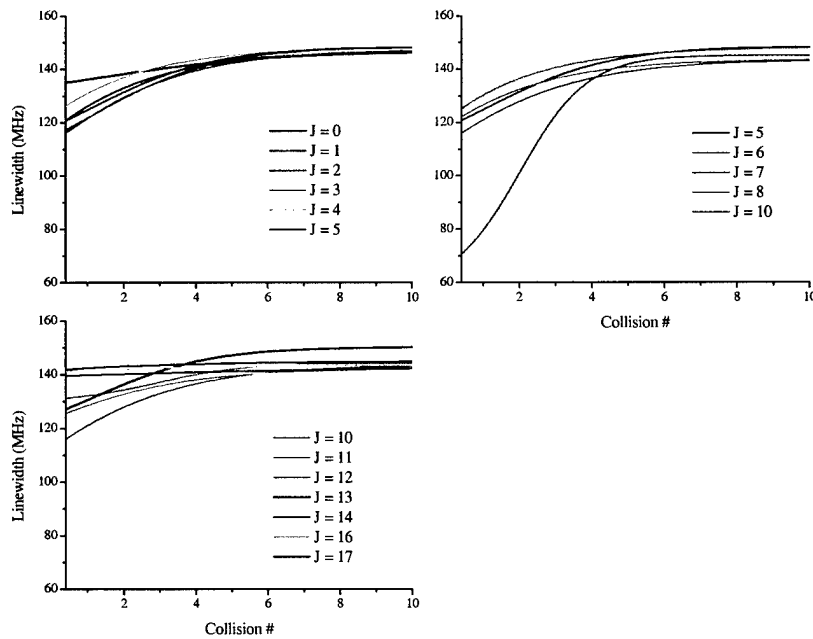


Figure 44. Linewidth comparison: R6 pump.

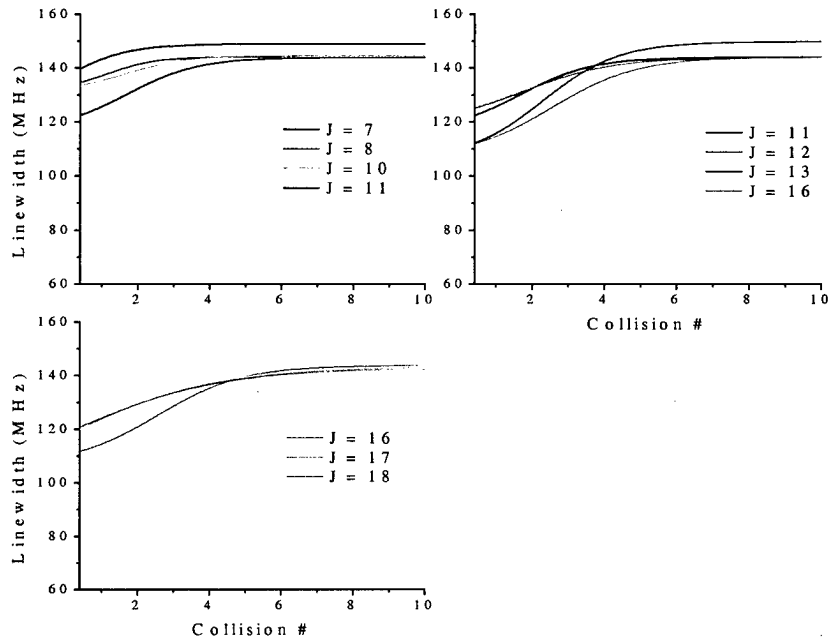


Figure 45. Linewidth comparison: R13 pump.

The equilibrium linewidths in Figures 43 - 45 differ because the probe's wavelength changes. Rotational levels $J = 0 - 7$ and $J = 13$ were probed with R transitions. All remaining levels were probed with P transitions. The linewidths are shown after 0.4 collisions since usually the measurement was unstable before then. Table 12 shows the initial and equilibrium linewidths (at 0.4 and 15 collisions respectively), their ratio, and the uncertainty in the measurement given by σ . The linewidth values are based on the curve fits. If linewidth change was not detected, a single theoretical value is given. The theoretical linewidth was based on the Voigt profile and was calculated using the temperature and pressure measured during the rotational relaxation portion of the experiment. Figure 46 shows the information given in Table 12.

Table 12. Initial and Equilibrium Linewidths. Initial and final values are in MHz.

J Level	P1 pump			R6 pump			R13 pump		
	initial	final	ratio $\pm \sigma$	initial	final	ratio $\pm \sigma$	initial	final	ratio $\pm \sigma$
0	74.1	146.6	0.51 \pm 0.07	135.1	147.7	0.91 \pm 0.08		146.7	
1	114.6	146.0	0.78 \pm 0.04	121.0	146.5	0.83 \pm 0.03		147.4	
2	91.0	147.8	0.62 \pm 0.02	116.3	147.4	0.79 \pm 0.01		147.8	
3	109.3	148.1	0.74 \pm 0.02	117.5	148.5	0.79 \pm 0.01		147.6	
4	113.0	148.4	0.76 \pm 0.03	126.4	148.3	0.85 \pm 0.02		148.6	
5	116.5	148.1	0.79 \pm 0.03	120.9	148.7	0.81 \pm 0.03		148.1	
6	112.3	149.4	0.75 \pm 0.03	125.2	148.3	0.84 \pm 0.02		148.5	
7	111.0	148.8	0.75 \pm 0.03	70.7	145.3	0.49 \pm 0.11	139.6	148.9	0.94 \pm 0.01
8	121.9	144.5	0.84 \pm 0.02	122.2	143.9	0.85 \pm 0.02	134.5	144.0	0.93 \pm 0.02
10	119.8	144.0	0.83 \pm 0.03	116.1	143.7	0.81 \pm 0.04	133.4	144.5	0.92 \pm 0.02
11	127.5	143.7	0.89 \pm 0.03	125.6	142.4	0.88 \pm 0.03	122.4	143.9	0.85 \pm 0.02
12	131.3	143.6	0.91 \pm 0.04	131.3	144.4	0.91 \pm 0.02	125.0	143.7	0.87 \pm 0.02
13	137.0	150.7	0.91 \pm 0.04	127.2	150.4	0.85 \pm 0.03	112.1	149.6	0.75 \pm 0.03
14	143.2			142.1	145.1	0.98 \pm 0.02	141.8		
16	143.6			141.2	143.7	0.98 \pm 0.02	111.7	143.8	0.78 \pm 0.06
17	143.3			139.7	143.0	0.98 \pm 0.02	119.8	143.8	0.83 \pm 0.05
18	143.0			142.9			121.0	142.8	0.85 \pm 0.05

Pump Bandwidth

The linewidth in $J = 7$ following an R6 pump allows an estimate of the pump bandwidth. The known Doppler lineshape of ground state CO is broken into frequency bins, with each bin's width equaling the pressure-broadened linewidth. The pump bandwidth is sectioned into identical bins. Absorption is calculated for each bin using the homogeneous lineshape and Eq. (31) from Ref [27] which accounts for possible saturation by pump. The resulting population was plotted as a function of frequency (at the probe wavelength) and fit to a Gaussian. The pump bandwidth was varied until the width of the excited molecules predicted by the model equaled the bandwidth measured by the probe. The estimated pump bandwidth is 165 ± 5 MHz. Table 13 gives parameters important in the pump bandwidth calculation.

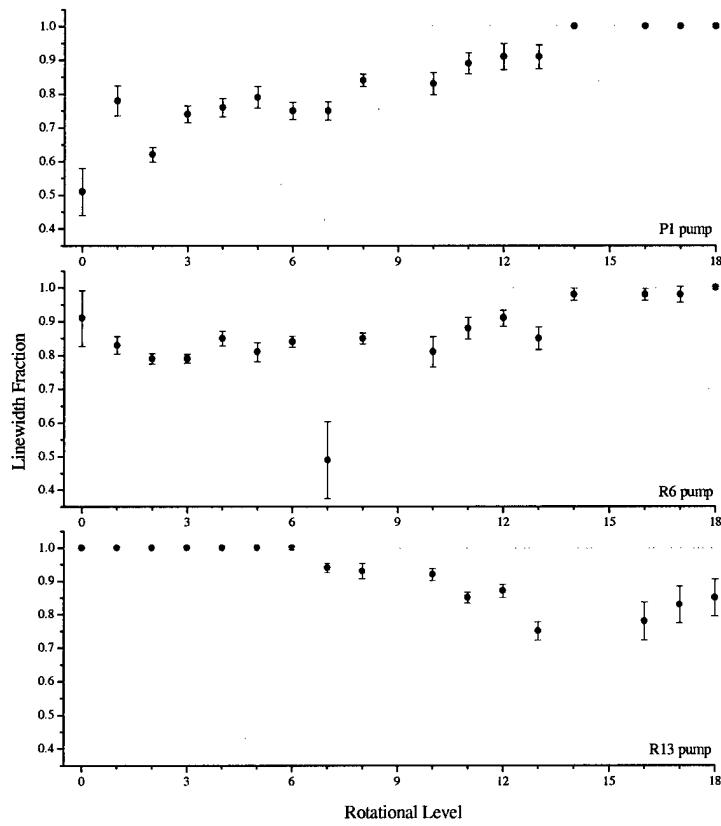


Figure 46. Initial linewidth fractions and error.

Table 13. Pump Bandwidth Calculation Parameters.

Pump wavelength (R6)	2.3337	μm
Probe wavelength (R7)	4.7185	μm
CO pressure	0.15	torr
CO temperature	296	K
CO/CO pressure broadening coefficient (see Ref [11])	7.3	MHz/torr
Homogeneous linewidth	0.35	MHz
Doppler linewidth (pump λ)	299	MHz
Pump energy	0.4	mJ
Path length	71	cm
Pump diameter	2.6	cm

MAGNETIC SUBLVELS AND THE MAGIC ANGLE

The linearly polarized pump creates an aligned distribution among the excited state's magnetic sublevels. How much of the linearly-polarized probe the aligned molecules absorb depends on the probe's polarization direction. Figure 47 shows the difference in absorption as a function of probe polarization after an R0 pump. As seen in the figure, the molecules retain a memory of their alignment even after undergoing a change in rotational level. Through how many rotational levels this memory persists was not measured. To avoid complications caused by magnetic sublevel alignment, the probe and pump polarizations were set so that the angle between them was 54.7° (the magic angle).

The polarization direction of the horizontally-polarized probe was not changed easily so the pump's polarization was varied instead. To compensate for the different losses sustained by the pump's vertical and horizontal polarization components when

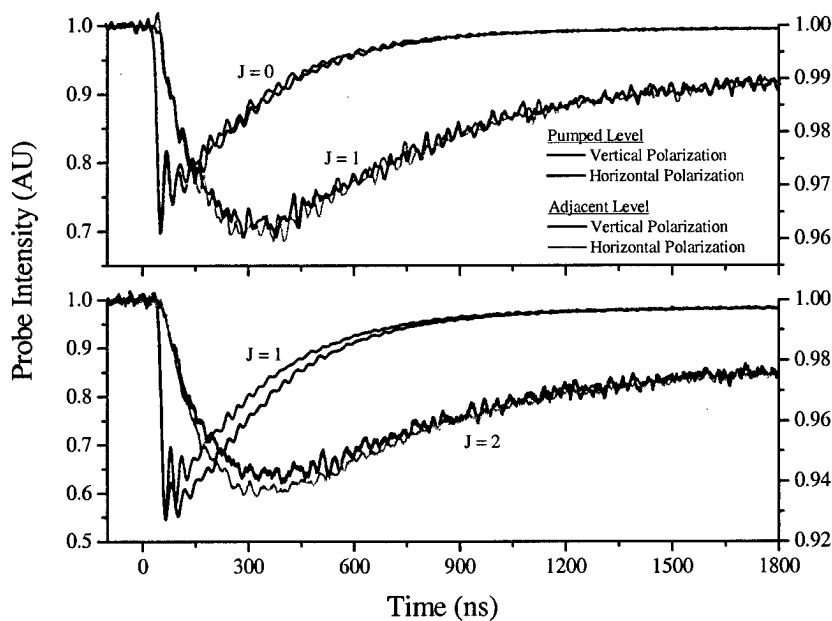


Figure 47. Evidence of magnetic sublevel memory. The top graph shows no difference in probe absorption with polarization following a pump into $J = 0$. The bottom graph shows a polarization dependence following a pump into $J = 1$. The scale of the left-hand y-axes corresponds to the pumped levels. The right-hand y-axes correspond to the adjacent levels.

passing through the CO cell's Brewster window, the pump polarization angle was set at 57.9° from the horizontal instead of 54.7°.

ROTATIONAL RELAXATION DATA

With the pump and probe polarizations set at the magic angle and vibrational and lineshape relaxation measured, the rotational populations were calculated using Eq. (2.16):

$$N_J(t) = \frac{1}{e^{-k_{loss}Mt}} \frac{1}{S(v,t)} \frac{8\pi}{A\lambda^2 L} \frac{g_J}{g_u} \ln \left[\frac{I(0)}{I(t)} \right]. \quad (2.16)$$

To ensure the rotational data was taken when both lasers were on line-center, at least sixteen waveforms were acquired for each J level. During rotational population measurements, the oscilloscope averaged 100 traces with 5000 samples acquired per trace. The calculated populations were scaled for pump energy fluctuations, as discussed at the end of chapter three, and averaged. Outliers, if present, were removed before averaging. Rotational populations J = 0 through J = 18 were measured for each of the three pumps except for J = 15 since a probe mode resonant with J = 15 (either a P or R transition) was never found. Figures 48 - 56 show the rotational populations along with parametric fits (red curves) and the uncertainty boundaries (dotted blue curves). The fits accurately reproduce rotational populations and help the least-squares routine avoid local minima caused by noise. The fits represented the data during the comparison with the rate-constant models. Eq. (4.5) gives the parametric equation (from TableCurve) which best mimics the rotational populations.

$$N(x) = a \left\{ 1 - e^{-b(x-x_c)} - \left[\frac{c}{c+d} \right] \left[1 + \frac{be^{-(c+d)(x-x_c)} - (c+d)e^{-b(x-x_c)}}{c+d-b} \right] \right\} \quad (4.5)$$

In Eq. (4.3), N(x) is the population density, x is the collision number, and (a,b,c,d,x_c) are the parameters. The value of x_c determines where the population rise begins. For collision numbers less than x_c, the value of N(x) is set to zero. Eq. (4.5) provides a convenient, compact way to express the populations and no physical meaning should be attached to its form.

Tables 14 - 16 give the parameter values for Eq. (4.3) that describe the rotational populations. The tables also include the standard deviation of the fit σ and figure-of-merit r^2 . The values of σ and r^2 were calculated using Eqs. (4.1) and (4.3) with the Δv expressions replaced by the populations. The parameter a in the tables has already been scaled so the resulting curves have equilibrium values which match the Boltzman distribution. The curves shown in the figures have not been scaled.

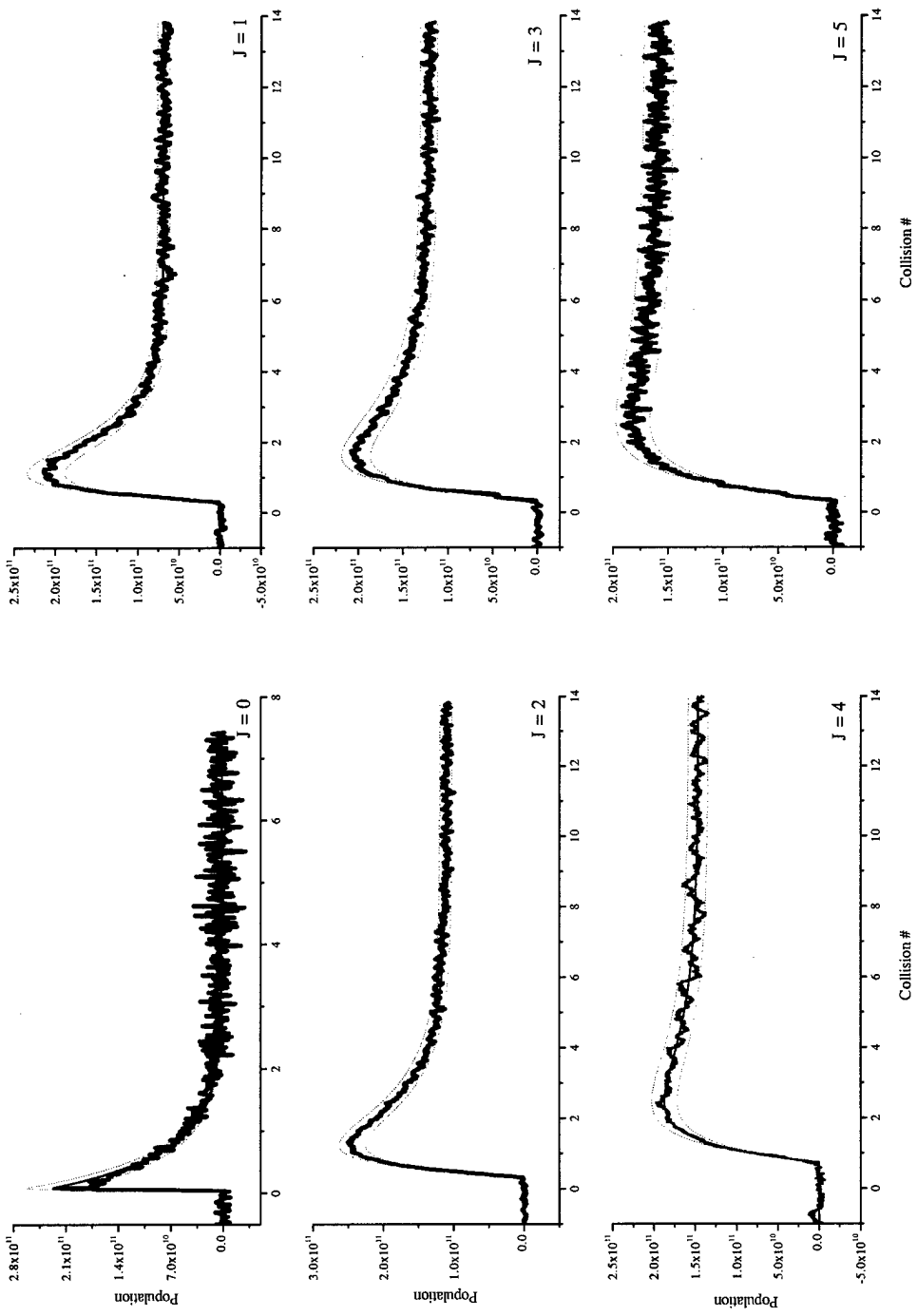


Figure 48. Rotational population: P1 Pump ($J = 0$ to $J = 5$).

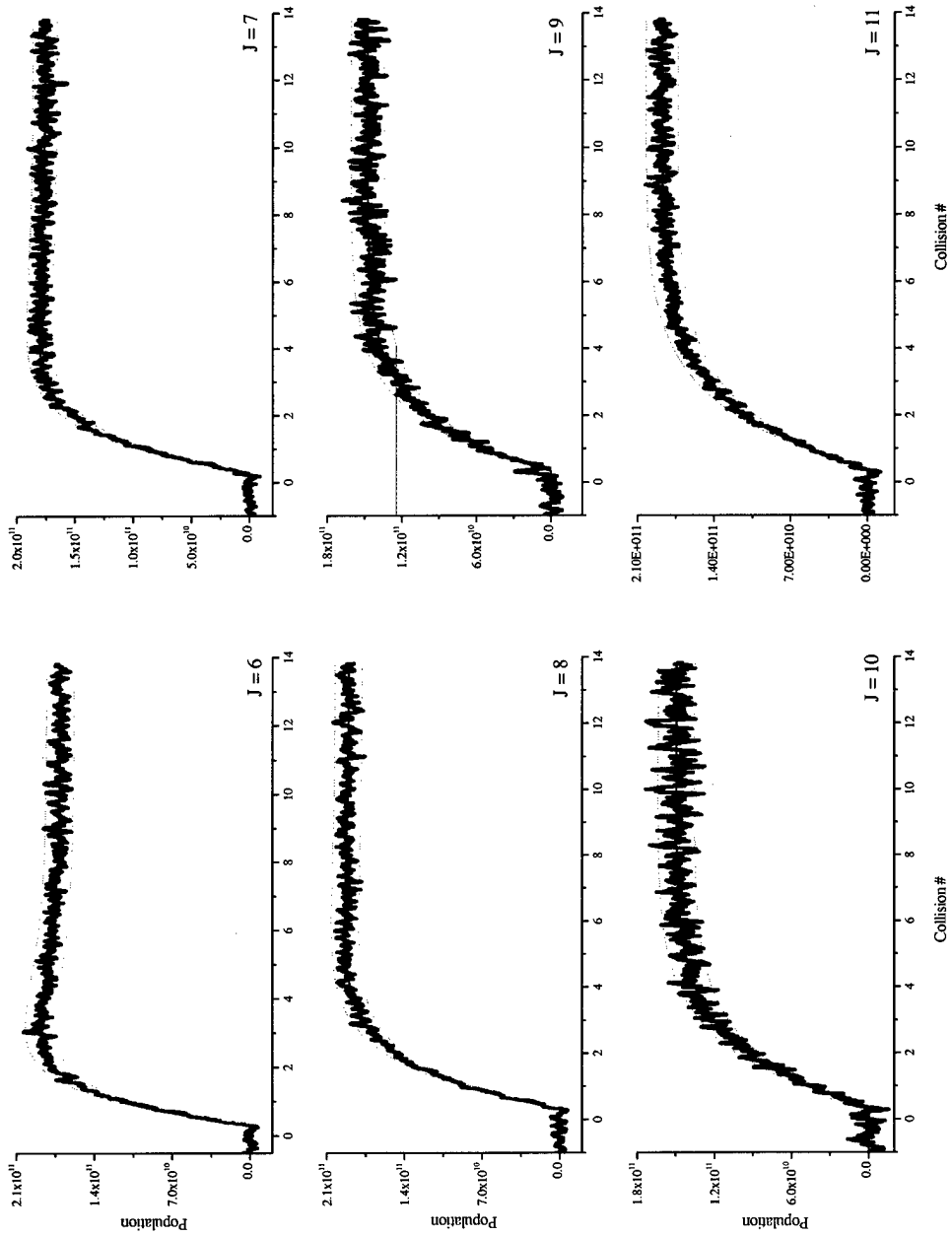


Figure 49. Rotational Populations: P1 Pump ($J = 6$ to $J = 11$).

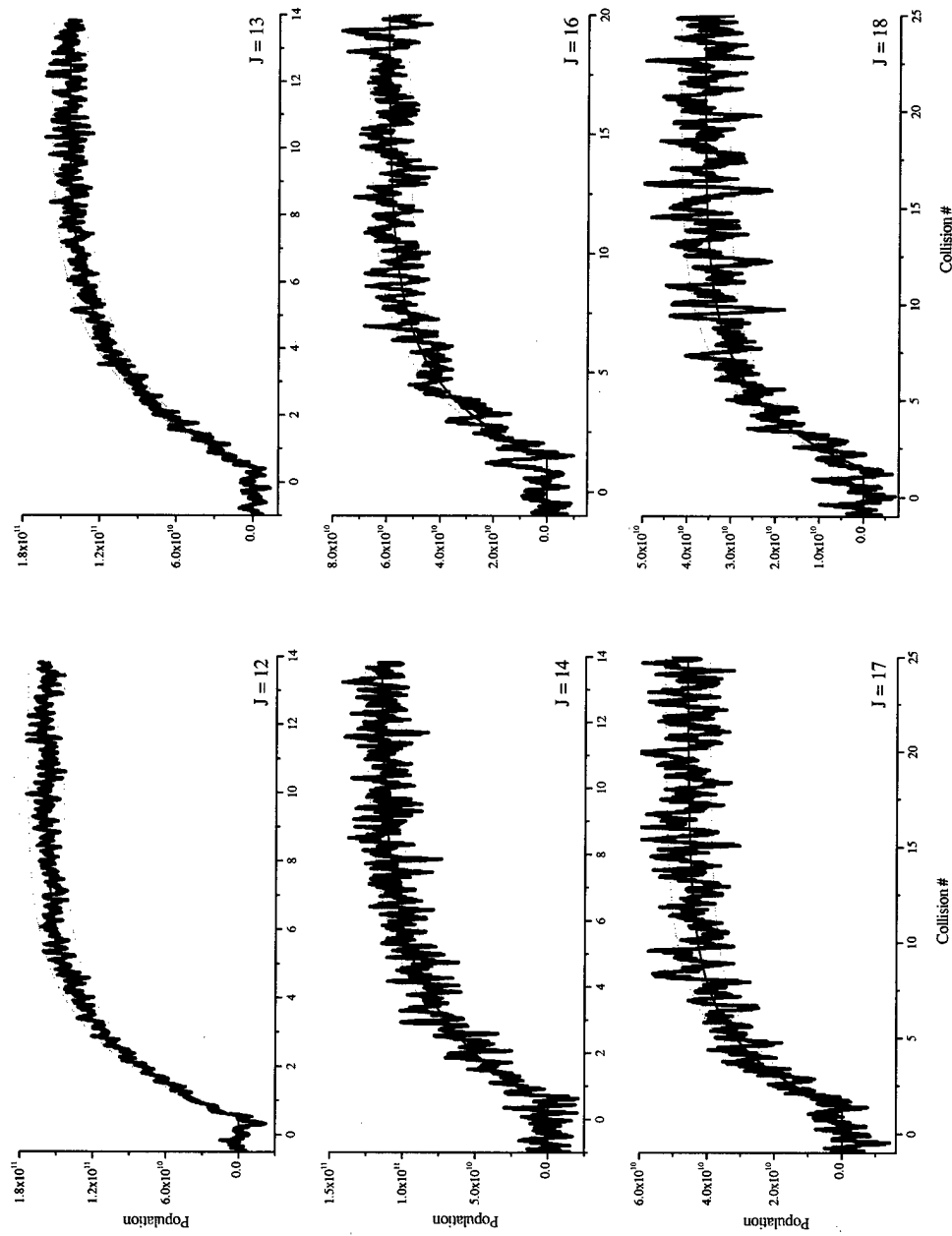


Figure 50. Rotational Populations: P1 Pump ($J = 12$ to $J = 18$).

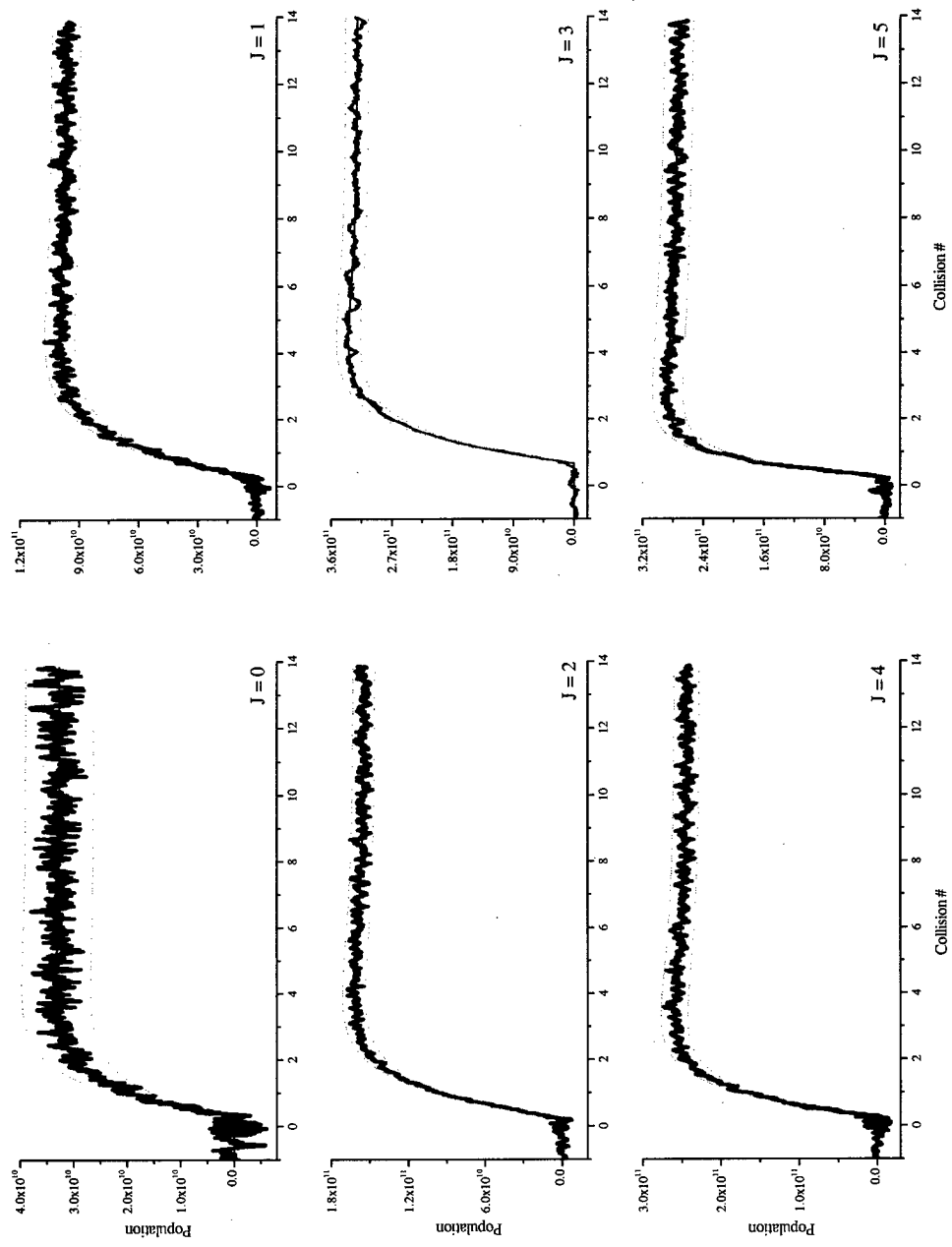


Figure 51. Rotational Populations: R6 Pump ($J = 0$ to $J = 5$).

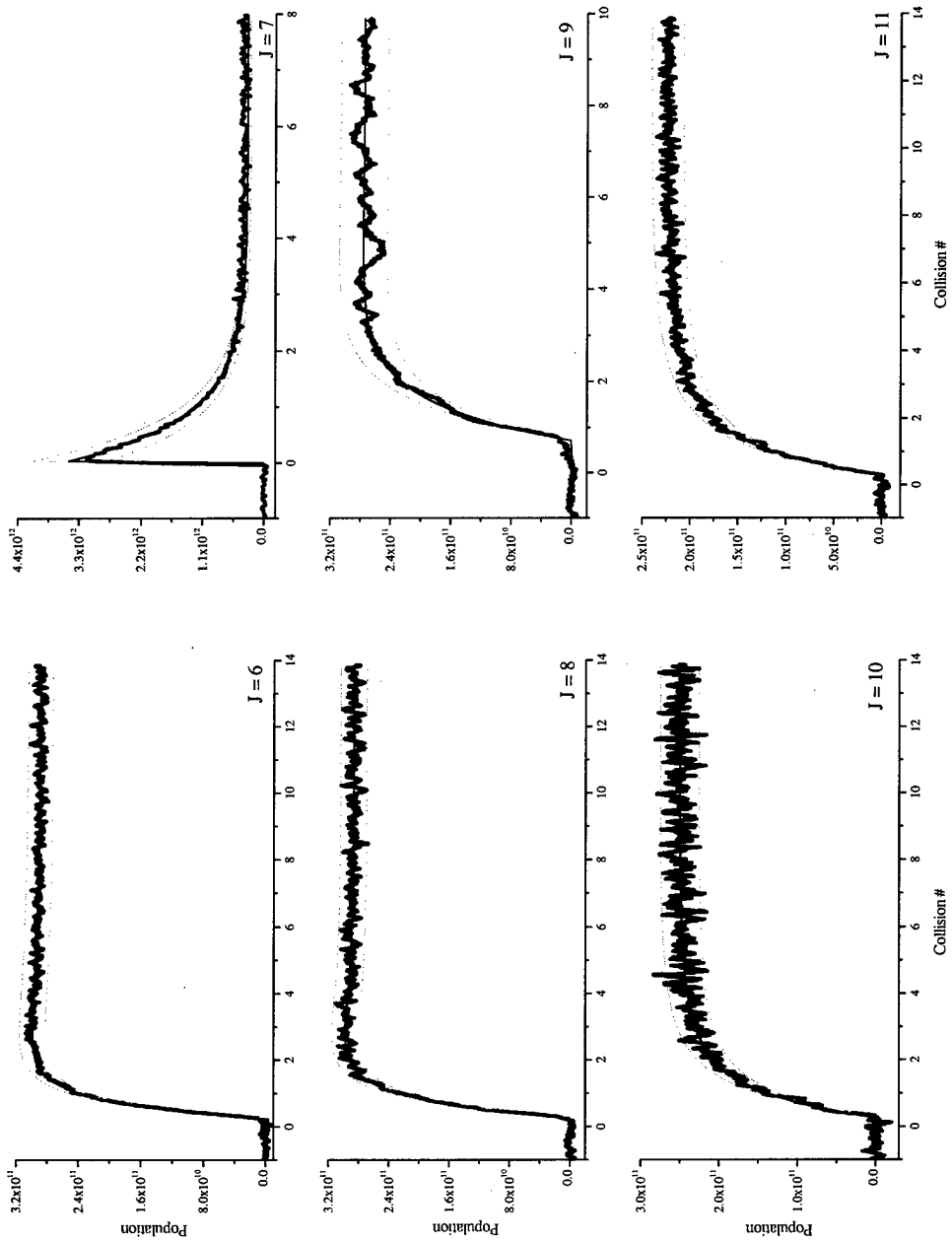


Figure 52. Rotational Populations: R6 Pump ($J = 6$ to $J = 11$).

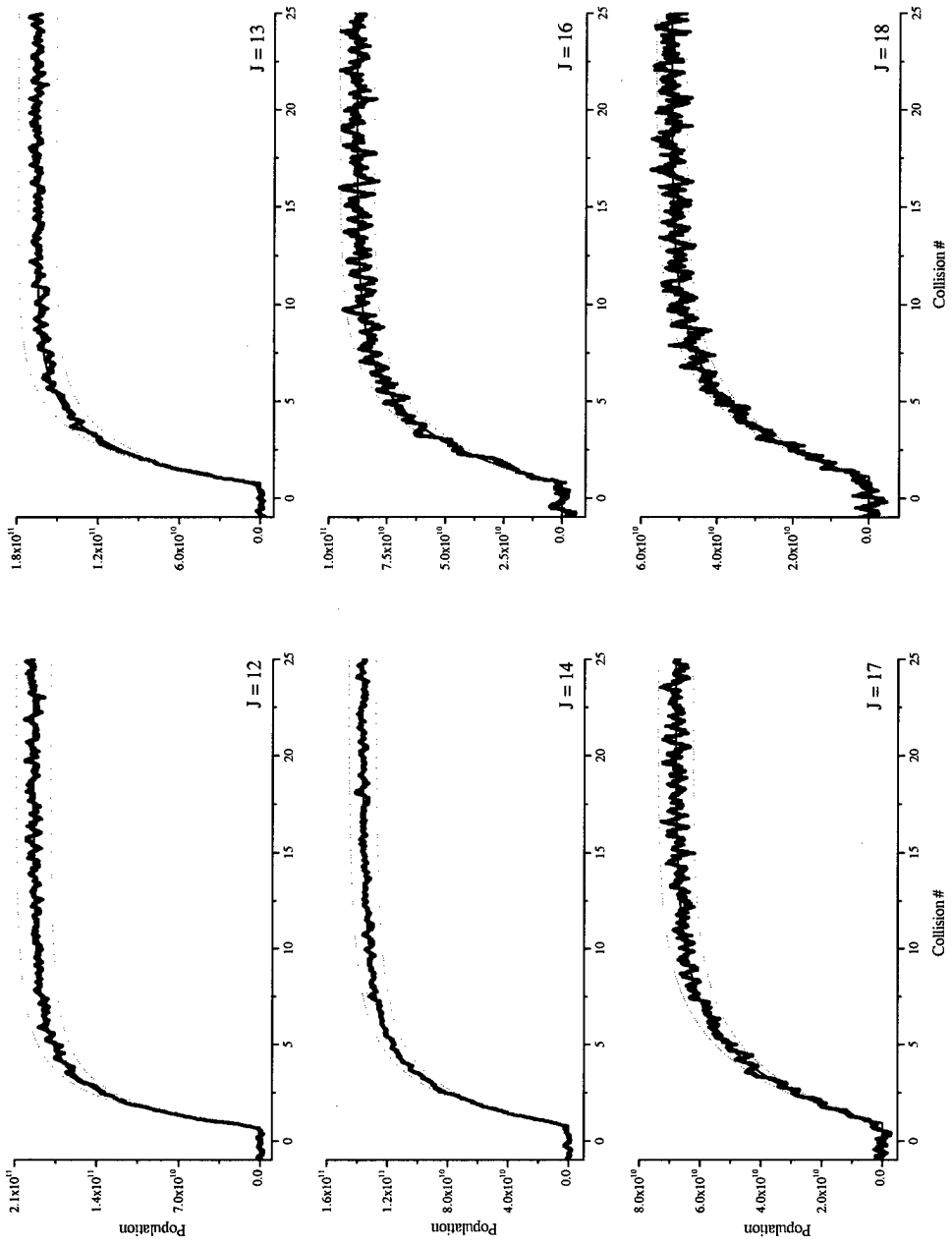


Figure 53. Rotational Populations: R6 Pump ($J = 12$ to $J = 18$).

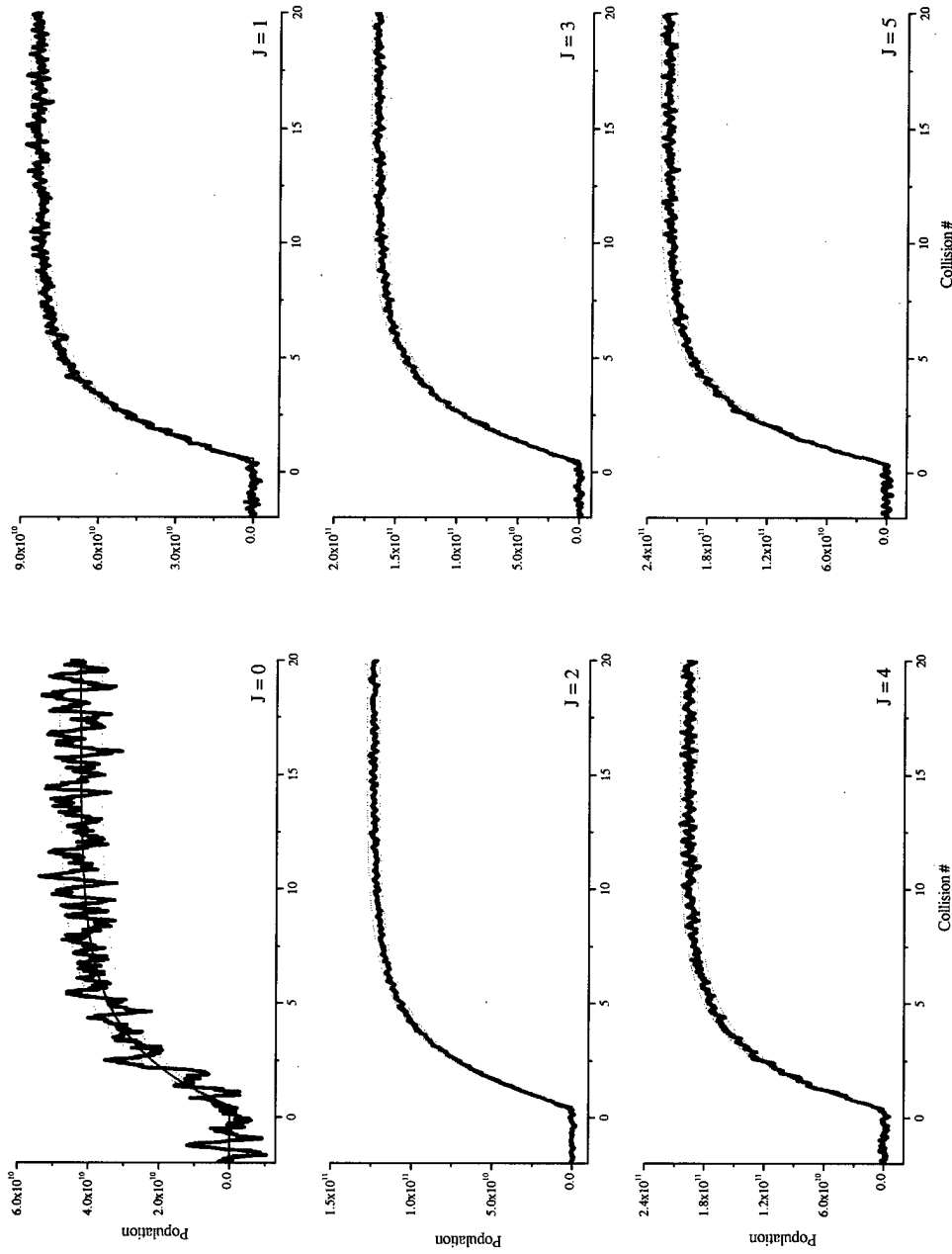


Figure 54. Rotational Populations: R13 Pump ($J = 0$ to $J = 5$).

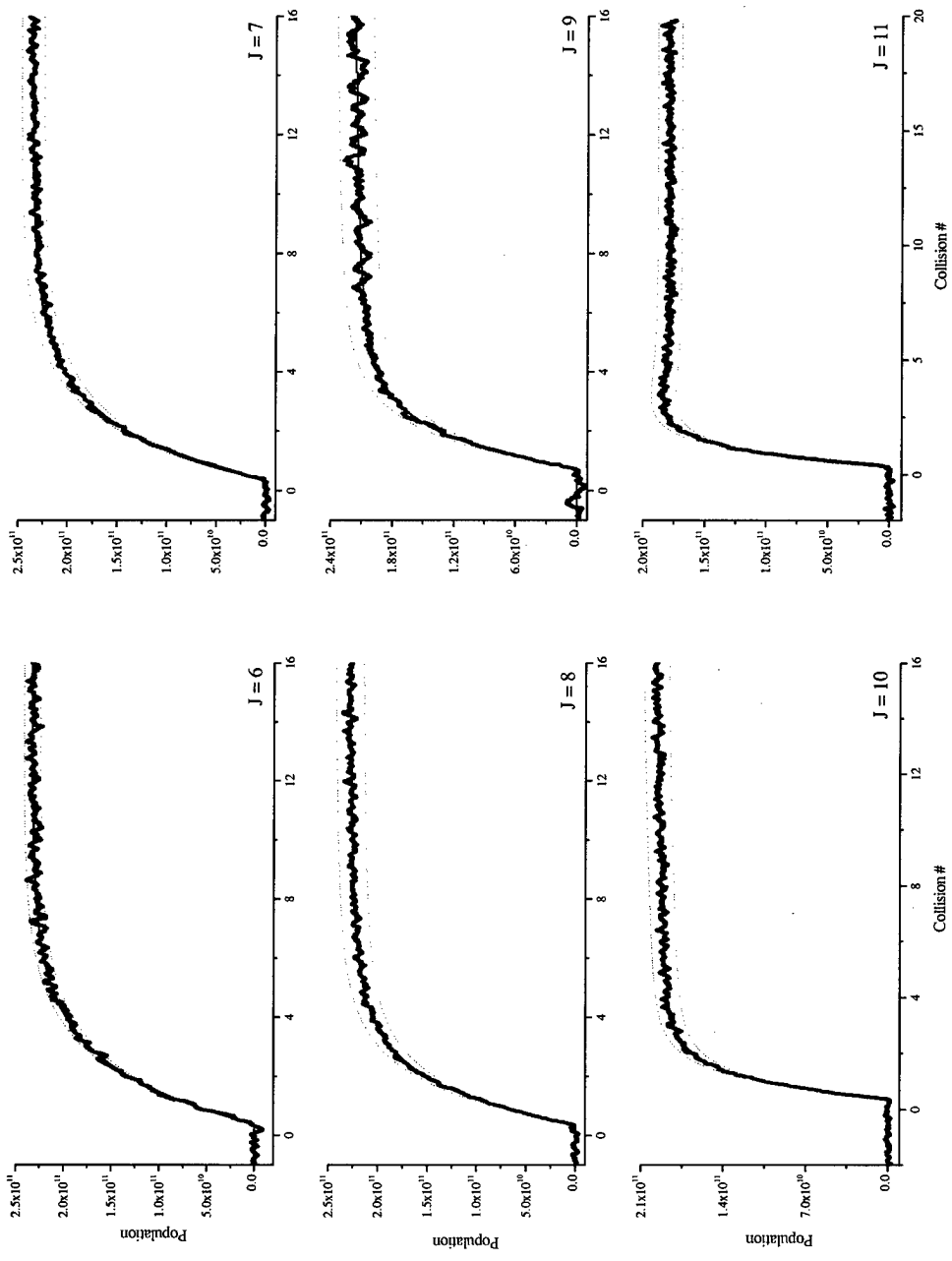


Figure 55. Rotational Populations: R13 Pump ($J = 6$ to $J = 11$).

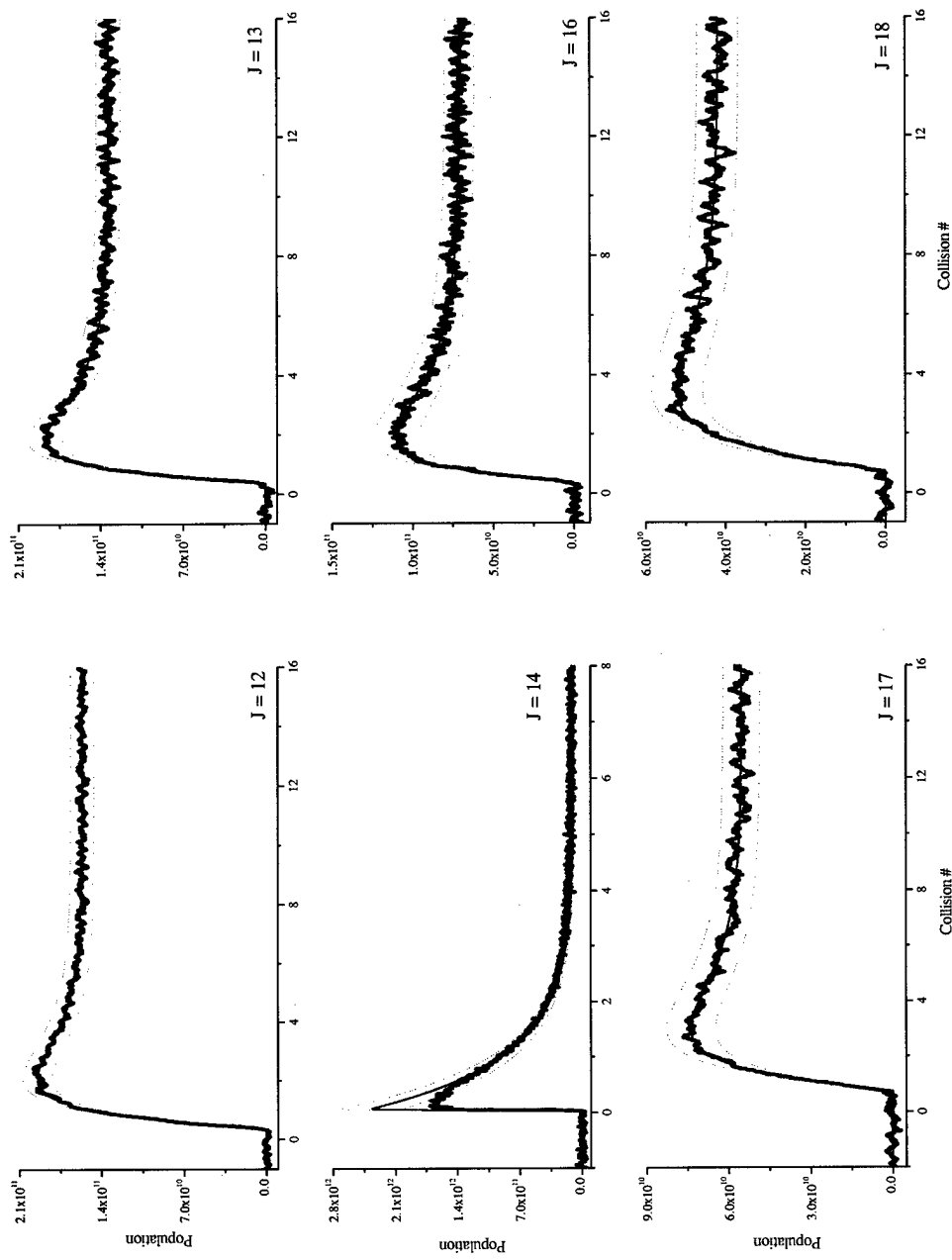


Figure 56. Rotational Populations: R13 Pump (J = 12 to J = 18).

Table 14. P1 pump rotational fit coefficients.

J	a	b	c	d	x_c	r^2	σ
0	2.1672e+16	150	1.78	0.0162	0.053	0.906	0.149
1	3.4678e+11	1.8143	0.9165	0.1824	0.325	0.993	0.108
2	3.0326e+11	2.3048	0.5009	0.2198	0.342	0.996	0.077
3	2.9559e+11	1.7657	0.3465	0.2452	0.362	0.995	0.079
4	7.9709e+11	0.4761	1.2856	0.2889	0.723	0.991	0.082
5	2.2549e+11	1.3803	0.1115	0.2907	0.329	0.993	0.085
6	3.0539e+11	0.7907	0.3013	0.3929	0.333	0.996	0.072
7	2.6470e+11	0.6611	0.2127	0.4178	0.313	0.995	0.059
8	2.6197e+11	0.5418	0.2049	0.3889	0.339	0.997	0.064
9	2.8185e+11	0.3851	0.2646	0.3612	0.343	0.985	0.090
10	2.0394e+11	0.4381	0.1287	0.3539	0.386	0.984	0.095
11	1.7737e+11	0.4168	0.1114	0.3432	0.401	0.996	0.078
12	1.7817e+11	0.3090	0.1347	0.2538	0.507	0.992	0.093
13	1.6126e+11	0.2380	0.1069	0.1600	0.408	0.988	0.093
14	3.4061e+11	0.3651	10.1914	3.2977	0.682	0.950	0.097
16	9.9397e+10	0.1965	0.1761	0.2104	1.443*	0.985	0.125
17	1.2510e+11	0.1100	0.2247	0.1157	1.396*	0.982	0.144
18	1.1732e+11	0.0814	0.2148	0.0802	1.488*	0.976	0.153

*The trigger detector was in a different position.

Table 15. R6 pump rotational fit coefficients.

J	a	b	c	d	x_c	r^2	σ
0	4.2847e+10	0.9102	0.1708	0.5486	0.323	0.997	0.194
1	1.4722e+11	0.6584	0.2169	0.4087	0.253	0.995	0.076
2	2.0291e+11	0.8968	0.1179	0.3759	0.255	0.998	0.055
3	5.4861e+11	0.6773	0.3207	0.4542	0.671	0.999	0.053
4	3.1084e+11	1.1320	0.0995	0.3665	0.260	0.997	0.066
5	2.9904e+11	1.9705	0.0183	0.1741	0.267	0.997	0.070
6	3.1455e+11	1.8918	0.0284	0.3124	0.258	0.999	0.055
7	3.578e+12	150	1.15	0.1025	0.000	0.954	0.192
8	3.3848e+11	1.5899	0.0974	0.5358	0.276	0.997	0.060
9	3.6950e+11	0.9116	0.2446	0.6755	0.710	0.994	0.114
10	5.0195e+11	0.5713	0.7061	0.6977	0.284	0.985	0.099
11	4.8006e+11	0.4922	0.7258	0.6310	0.297	0.997	0.075
12	4.4903e+11	0.3170	0.5146	0.3960	0.707	0.998	0.076
13	3.6701e+11	0.5077	3.4864	2.8660	0.807	0.998	0.085
14	3.4683e+11	0.2197	0.3998	0.2680	0.812	0.999	0.066
16	1.7256e+11	0.3932	5.8482	6.2022	0.857	0.990	0.083
17	1.8895e+11	0.3237	8.8616	5.1436	0.950	0.995	0.084
18	1.5430e+11	0.3213	10.5115	5.4570	1.145	0.986	0.076

Table 16. R13 pump rotational fit coefficients.

J	a	b	c	d	x_c	r²	σ
0	3.7527e+10	0.3662	8.8307	20.6670	0.521	0.934	0.140
1	1.3606e+11	0.4600	8.9400	11.8000	0.587	0.996	0.041
2	1.6892e+11	0.4270	5.7200	16.0000	0.494	0.999	0.032
3	1.8534e+11	0.4320	3.4100	27.3000	0.501	0.999	0.037
4	2.0191e+11	0.4620	1.3500	52.7000	0.438	0.998	0.042
5	2.4736e+11	0.4740	3.8000	29.9000	0.406	0.999	0.038
6	2.5255e+11	0.5170	3.0600	35.0000	0.399	0.998	0.037
7	4.4201e+11	0.5280	3.5300	4.0300	0.435	0.999	0.049
8	1.0785e+12	0.1460	0.5690	0.1550	0.385	0.999	0.062
9	1.0627e+12	0.1670	0.7000	0.1810	0.762	0.997	0.081
10	2.3894e+12	0.1060	1.2600	0.1160	0.383	0.999	0.054
11	2.7399e+11	0.9500	0.3320	0.6320	0.378	0.999	0.054
12	2.9742e+11	1.2600	0.3540	0.3930	0.364	0.999	0.063
13	2.6374e+11	1.5900	0.2950	0.3010	0.383	0.996	0.076
14	2.973e+14	160	1.09	0.0421	0.045	0.952	0.146
16	5.0031e+11	0.4730	1.3200	0.2190	0.383	0.987	0.129
17	1.7526e+11	0.6000	0.5660	0.2610	0.740	0.992	0.121
18	1.0210e+11	0.6090	0.3780	0.2640	0.744	0.989	0.122

In the tables, the differences in the values of x_c are caused by noise obscuring the initial population rise. This is especially true for less-populated levels where the noise was a significant fraction of the total signal. The left side of Fig. 57 shows the growth in rotational populations after molecules were pumped into $J = 14$ ($J = 14$ is not shown). The figure shows it takes 1.5 half hard-sphere collision times for the gradual rise in the $J = 0$ population to climb out of the noise. Discrepancies in x_c were also caused by glitches in the oscilloscope triggering. The delay of $J = 10$ in Fig. 57 is the result of a triggering error. During least-squares minimization with the rate constant model, the value of x_c was set to zero for all but the pumped levels.

Finding appropriate fit parameters for the pumped levels required considerable effort. Figure 58 illustrates the problems with measuring and fitting pumped levels. In the $J = 0$ graph, the equilibrium population of $J = 0$ is hidden in the noise. The scaling procedure which ensures a final Boltzmann distribution among the populations

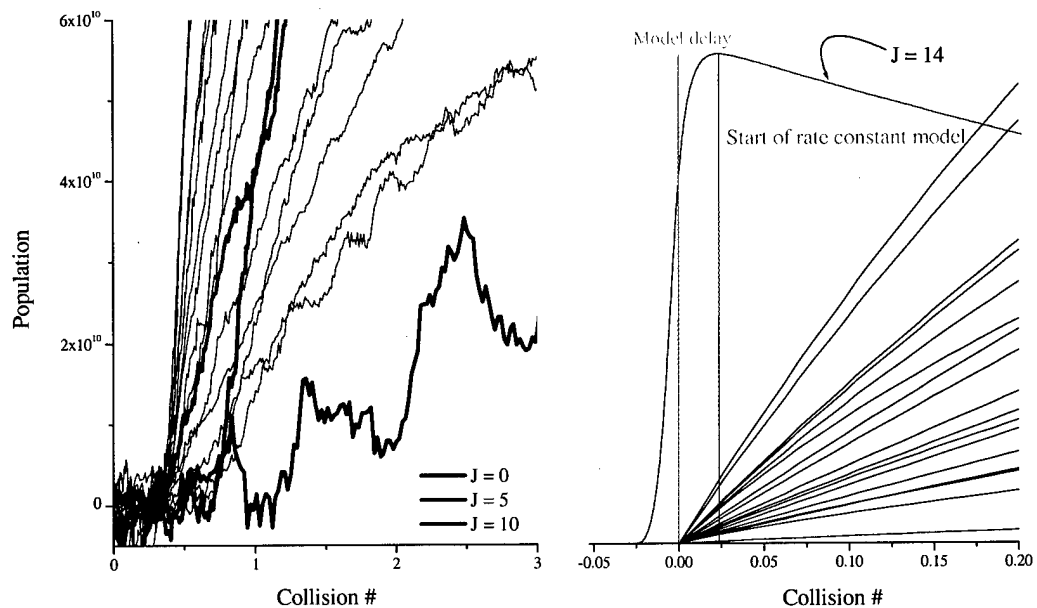


Figure 57. Start of population growth (R13 pump). The data on the left show population growth begins simultaneously in all the levels. The graph on the right illustrates the convention used when preparing the data for fitting with the Eq. (1.22).

uses each level's equilibrium value to find the scale factor. In the pumped levels, small errors in the equilibrium population are magnified at the measurement's beginning. Problems at the population's peak also contribute. In the $J = 14$ graph, the population peak slowly rolls over instead of immediately dropping as it should. The roll over is caused by a non-resonant pump.

Linewidth measurements indicated that the pump was off-resonance during the R13 pump, $J = 14$ measurements. The slow roll over in the bottom graph of Fig. 58 supports this conclusion. Despite efforts to the contrary, iff the pump frequency is tuned off line center, the lineshape of the excited molecules will be displaced from the probe frequency and yield lower-than-expected probe absorption. As collisions move the lineshape back toward its normal frequency, the probe absorption should increase. But molecules rapidly leaving the pumped level and linewidth relaxation, overpower any absorption increase. The combined effect is the slow roll over in population.

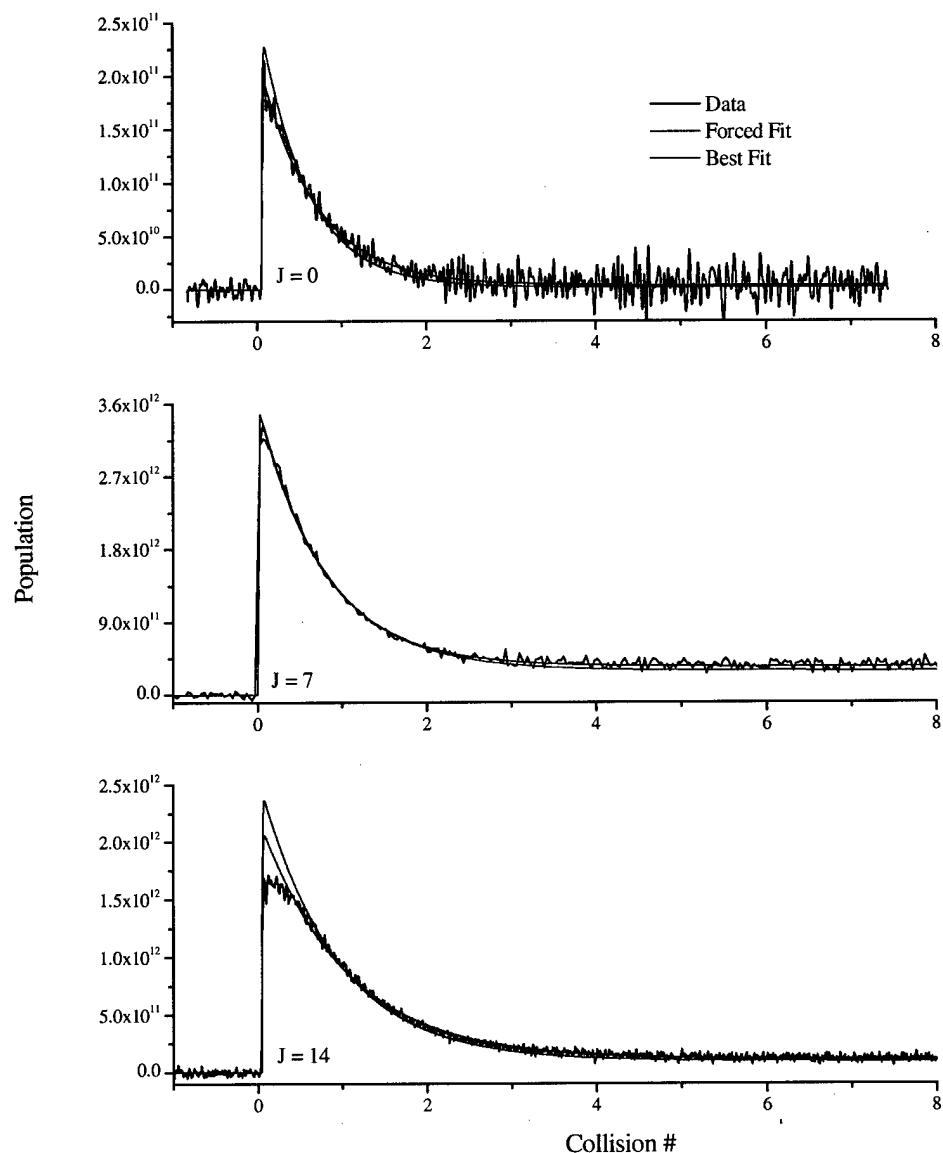


Figure 58. Close up of pumped levels. The figures show the problems involved in measuring the pumped levels. In the $J = 0$ case there is too much noise at equilibrium. In the $J = 14$ case, an off-resonant pump caused the flattened peak.

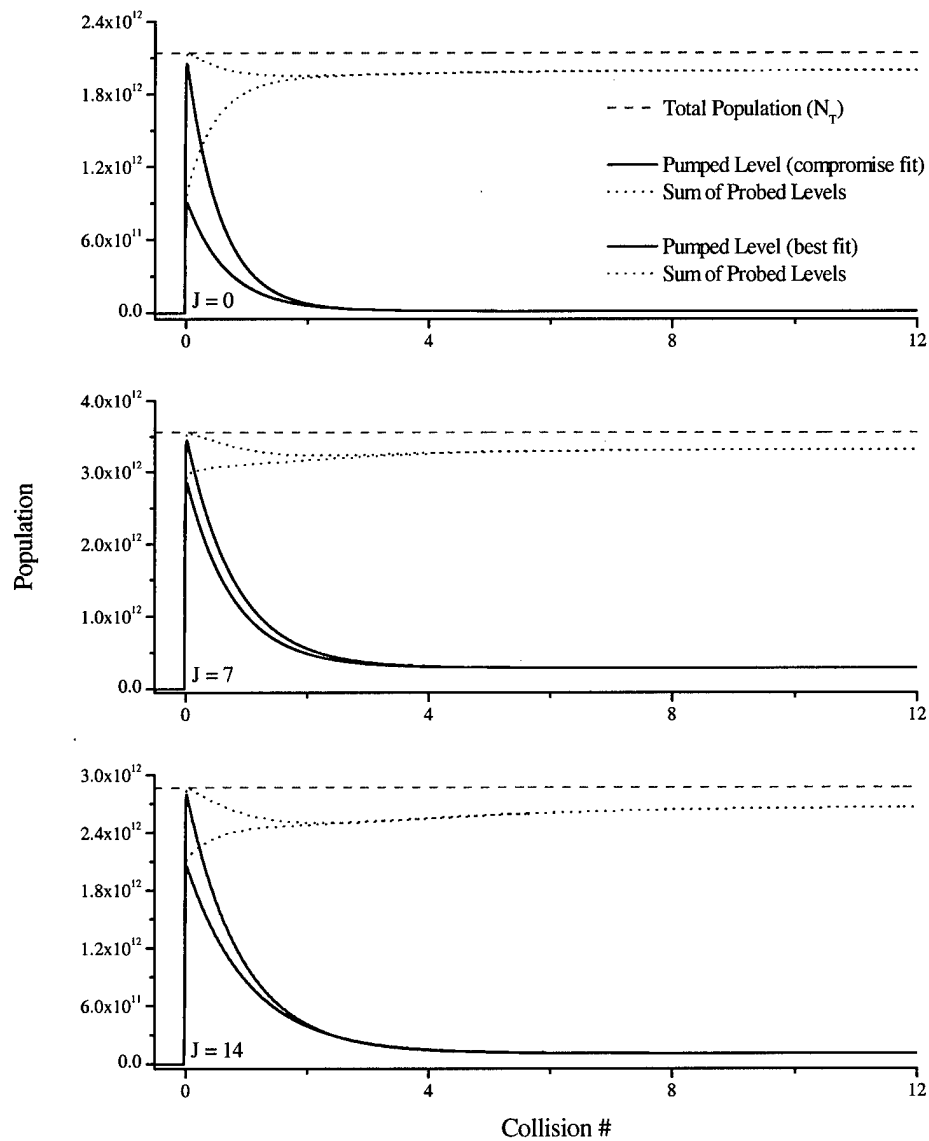


Figure 59. Sum of the rotational levels. The parameters of Eq. (4.3) were altered when applied to the pump levels, forcing the initial population to match the final population.

Problems with the pumped-levels reveal themselves during data reduction. With vibrational losses accounted for, the data should show that the $v = 2$ population remains constant at some value N_T set during the scaling procedure. N_T is easily calculated by dividing the final population in a highly populated level by the level's equilibrium probability. Because some rotational levels were not probed ($J = 15, 19, 20, 21, \dots$) the rotational populations will add up to N_T at the beginning of the measurement but not thereafter. Figure 59 shows the $v = 2$ populations when Eq. (4.3) is best fit to the measured pumped levels and when the fit is forced to meet the N_T population condition.

The poor showing of the best-fits reflects inaccuracy in measuring the pumped levels. Rather than discard the pumped levels, an effort was made to salvage the relaxation information by forcing the fitting parameters to compensate for the experimental difficulties. Of the five parameters in Eq. (4.3), altering the value of d had the greatest effect since it changed the scale factor by altering the equilibrium population. The changes made to d were constrained so at equilibrium the fit population remained within the noise of the measured population. The b parameter determined the amount of time between x_c and the population peak. The pump pulse delivered its energy within 20 ns so b was set to ensure the peak population occurred 20 ns after the population start (at 0.15 torr this was 0.033 collision numbers). The same value of b was used in both the best-fit and forced-fit cases. Noise in the x_c measurements required an educated guess as to the delay between the rise in the pumped level and the rise in the adjacent levels. Population build-up in the adjacent levels was assumed to begin once the pumped level reached eighty percent of its peak value. In collision numbers this corresponded to $x_c = -0.01$ for the pumped levels and $x_c = 0$ for all others. The right side of Fig. 57 shows the timing in the population starts when the fits are used. The value of c was changed to keep the curvature of the fit population in line with the data as much as possible. Any changes in parameter a were countered by the scale factor.

Figures 60 - 62 show the rotational populations on the same scale. The pumped levels are not shown.

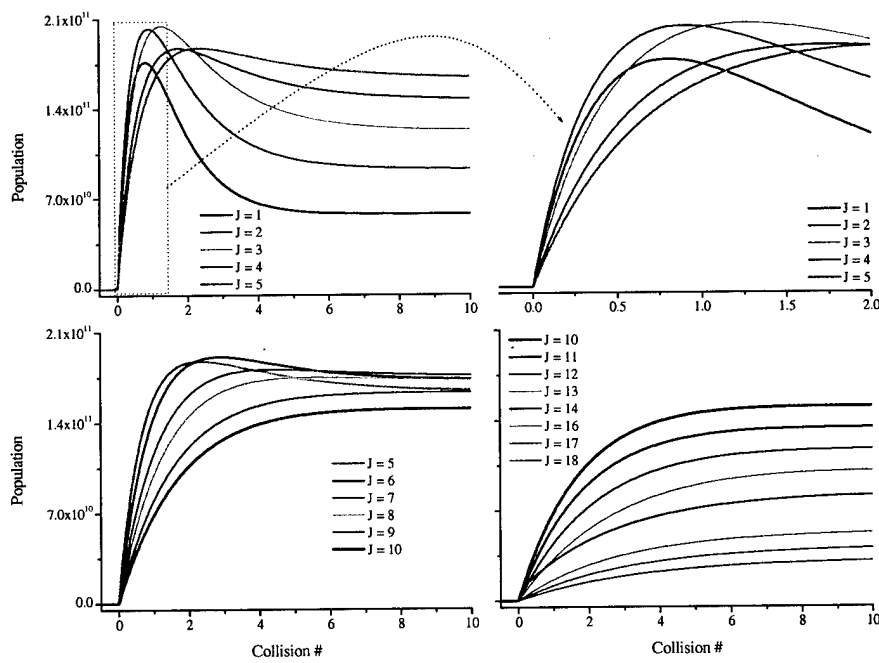


Figure 60. P1 pump populations.

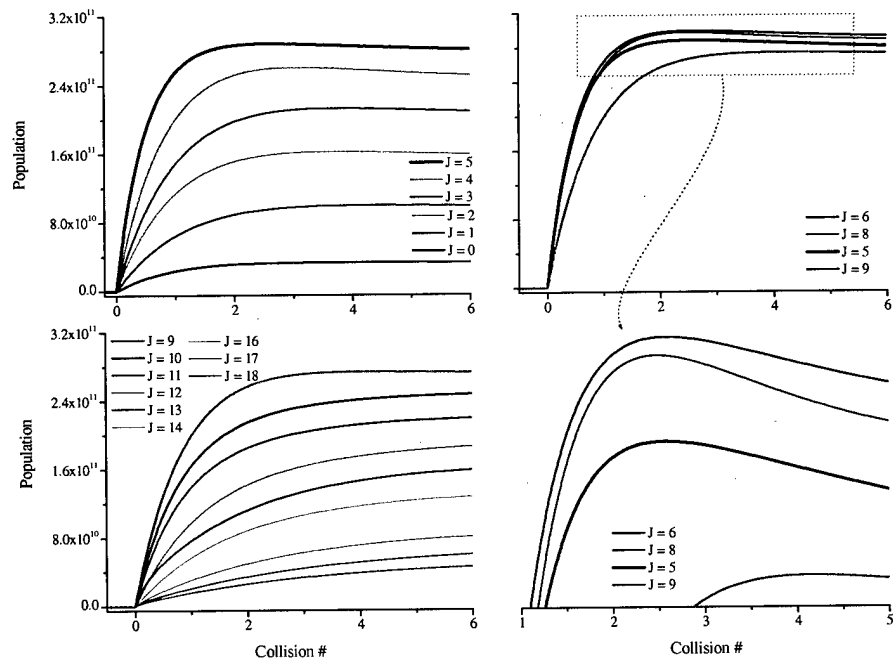


Figure 61. R6 pump populations.

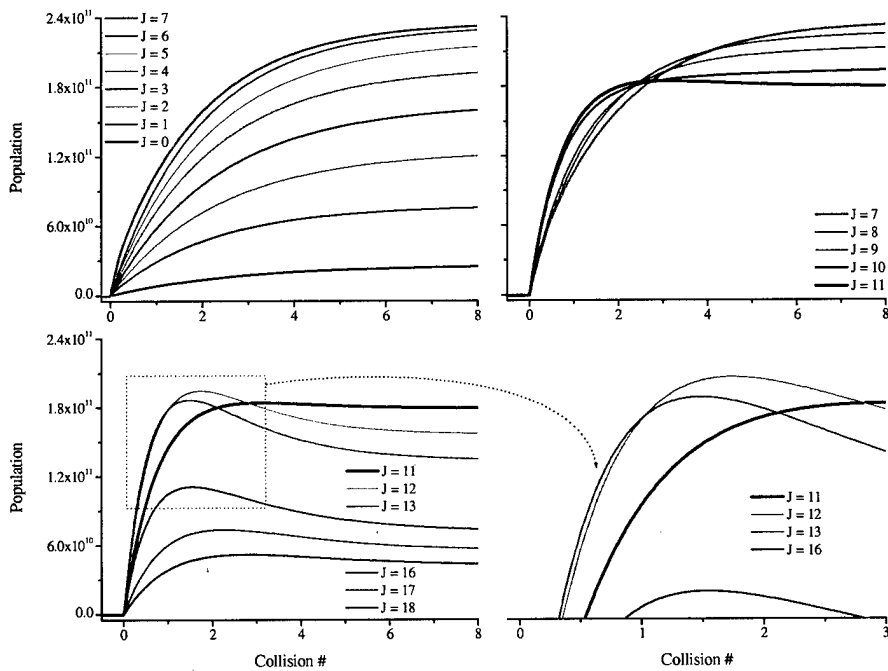


Figure 62. R13 pump populations.

RATE CONSTANT MODEL FITS

With the measured populations in hand, comparison with the RET model given by Eq. (1.22) may begin. The sums in Eq. (1.22) includes all levels out to $J = \infty$. At room temperature, ninety-six percent of the populations lie within levels $J = 0$ to $J = 18$. The model should therefore track at least to $J = 18$. Since molecules pumped into $J = 14$ were expected to temporarily spill over into levels beyond $J = 18$, the model tracked levels out to $J = 29$. Eq. (1.22) becomes

$$\frac{dN_i}{dt} = - \sum_{j=0(i \neq j)}^{29} k_{ij} N_i M + \sum_{j=0(i \neq j)}^{29} k_{ji} N_j M. \quad (4.4)$$

Eq. (4.4) represents a set of thirty coupled differential equations, which, when combined with initial values, predict the movement of molecules among the rotational levels. Because Eq. (4.4) does not account for the pump adding molecules into $v = 2$, the initial population values must come from data acquired after pumping is complete. In the

data, pumping is complete when the sum of the rotational populations in $v = 2$ reaches a maximum. The individual population values at the time of the maximum become the initial values entered into the model (see the right-hand graph in Fig. 57).

The differential equations were solved with a spreadsheet using a fourth-order Runge-Kutta routine. The spreadsheet also performed a Levenberg-Marquardt least-squares minimization [56] when optimizing the rate constant parameters. During the comparison with theory, the data was represented by Eq. (4.3) and the parameters in Tables 14 - 16. Model and data were compared at 500 points over the first 7.5 hard-sphere collisions. Though data beyond 7.5 collisions was available, the majority of rotational relaxation took place within 7.5 hard-sphere collisions.

Error between theory and measurement was calculated using Eq. 4.5

$$\Delta F(x) = \frac{\sqrt{[N_E(x) - N_T(x)]^2}}{N_E(x)} \quad (4.5)$$

where $\Delta F(x)$ is the fractional error at collision number x , $N_E(x)$ is the experimental population value, and $N_T(x)$ is the theoretical value. For each model and data set (P1, R6, R13) Fig. 63 shows the sum of $\Delta F(x)$ over all x for each rotational level (18 levels per data set). The SPG model was left off the lower graph in Fig. 63 as its error was significantly greater than all the other models, even when Eq. (2.26) was modified (for the SPG model only) to add a fourth parameter. Eq. (4.6) shows the homonuclear propensity term adapted for SPG model where c and d are the parameters:

$$H = 1 - \frac{d}{2} \left(\frac{B_v}{\Delta E} \right)^{-c} [1 - (-1)^{J_i + J_r}] \quad (4.6)$$

Figure 64 shows the sum of the fractional error associated with each model. The models were fit simultaneously to all three data sets. Initially the data sets were modeled separately, but the parameters that gave the best fit for one data set did not give the best fit for another. In retrospect, one could have anticipated this since the transition features

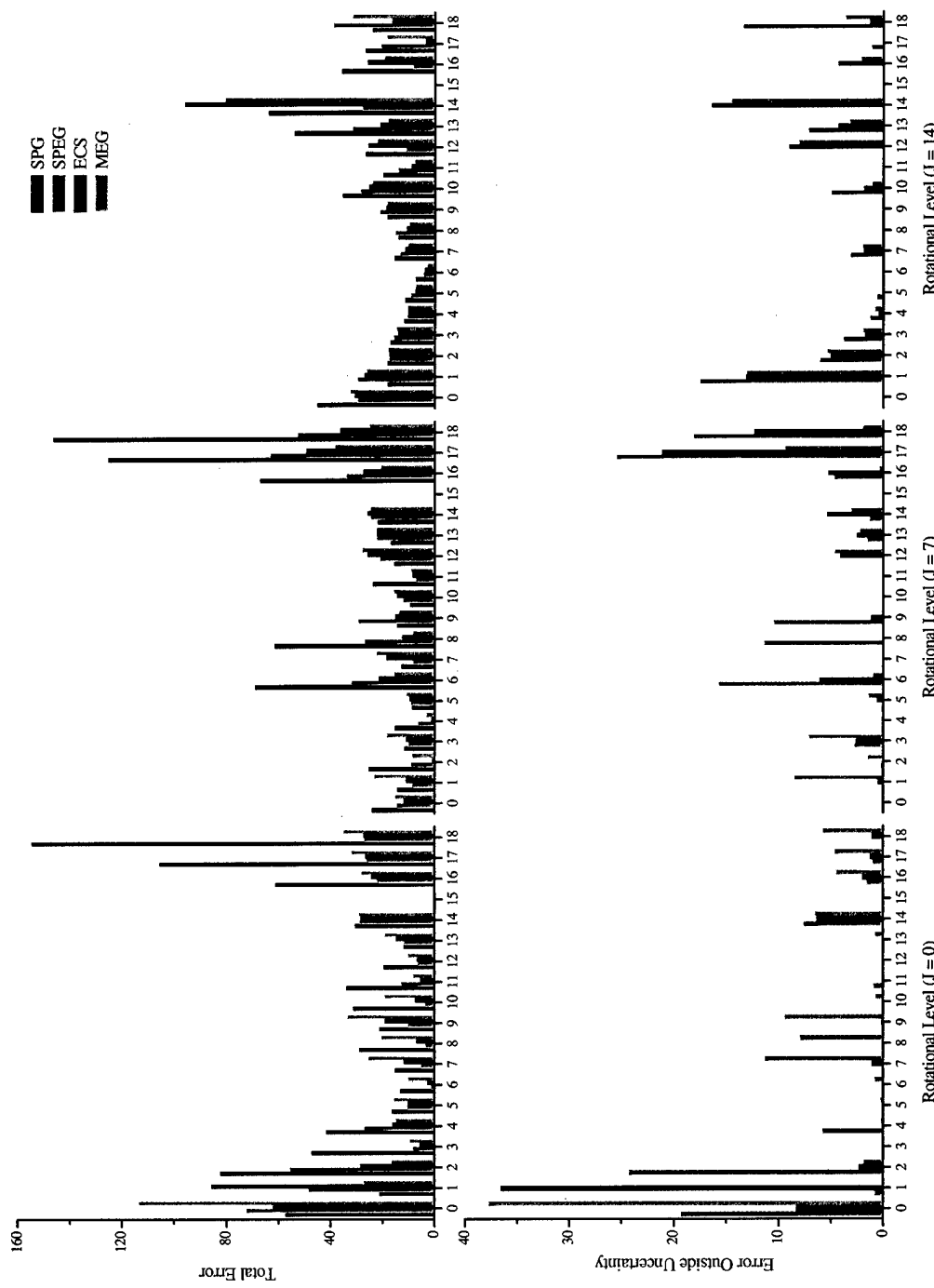


Figure 63. Fitting Errors. The top shows the total fractional error. The bottom shows error outside the uncertainty limits.

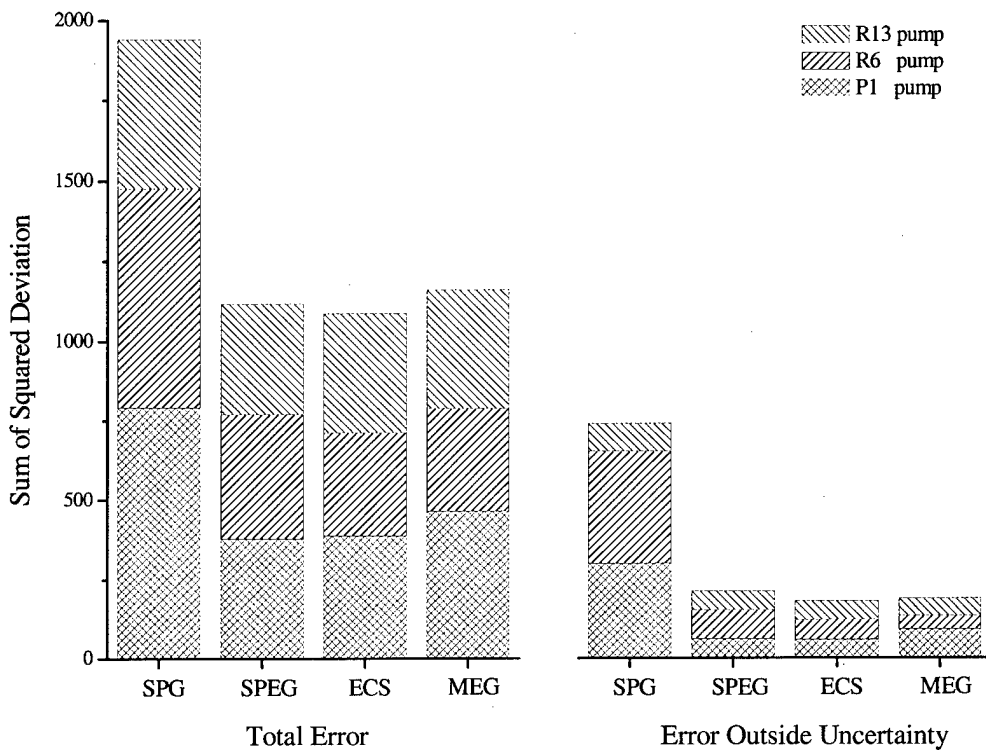


Figure 64. Fractional error associated with each model. There are 29,000 data points associated with each column. A total error of 1200 is equivalent to $\sim 4\%$ error per data point.

associated with small rotational energy gaps, easily seen when pumping into $J = 0$, disappear when pumping into $J = 14$. The top row in Fig. 63 shows the total error calculated according to Eq. (4.5). The bottom row shows the error calculated when the fitting routine accounts for the uncertainty in the population measurements.

When fitting with the uncertainties, the program counted as error only the amount of population falling outside the uncertainty limits. Levenberg optimization did not perform well with uncertainty included since the optimization relies on derivatives of the error with respect to the parameters, and the derivatives do not transition smoothly at the uncertainty boundary. A grid-search method took over when Levenberg optimization failed.

Figure 65 is a color contour plot of each model's 30×30 rate constant matrix. The diagonal in each plot is made up of the k_{ii} rate constants whose values are set to zero. The k_{ij} rate constants ($i < j$) lie below the diagonal and the k_{ji} rate constants—calculated from detailed balance—lie above. The $k_{0,1}$ rate constant is in the upper left corner; $k_{0,29}$ is in bottom left corner; and $k_{28,29}$ is in the bottom right corner. The rate constants are plotted on a logarithmic scale: the regions of brightest red correspond to rate constant values on the order of $2 \times 10^{-10} \text{ cm}^3/\text{molec}\cdot\text{sec}$; the regions of deepest blue correspond to rate constant values on the order of $1 \times 10^{-15} \text{ cm}^3/\text{molec}\cdot\text{sec}$.

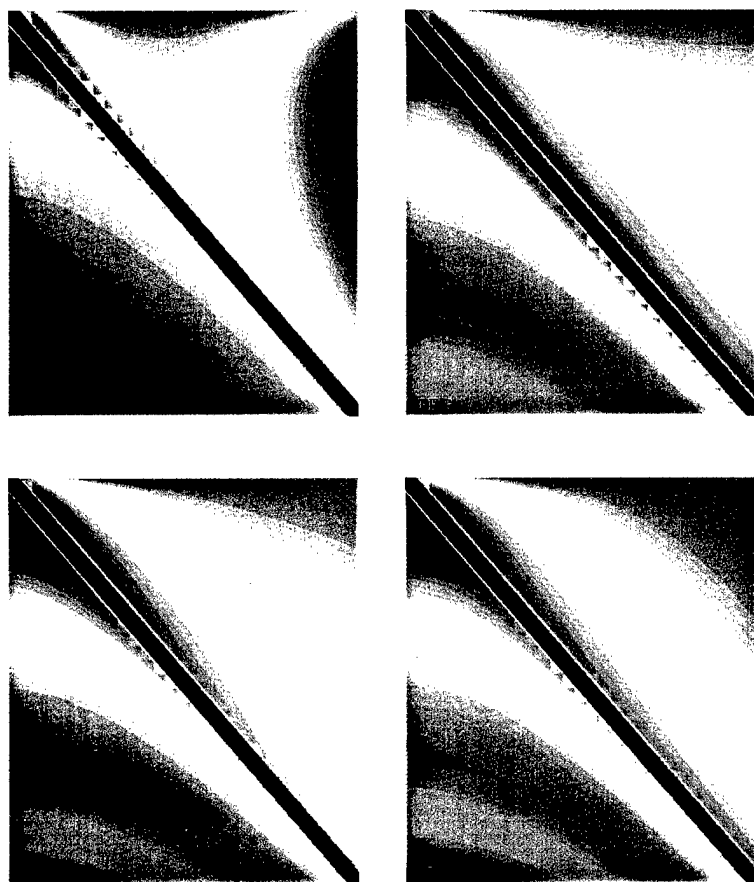


Figure 65. Color contour plots of the rate constant matrices.

CHAPTER 5: DISCUSSION

The SPG, SPEG, ECS-EP, and MEG rate constant models are fitting laws which, with three or four parameters, predict state-to-state RET rate constants. Such predictions are useful when solving an engineering problem like modeling laser performance. In this chapter the model results from Chapter 4 are compared with those in the literature. Knowing which rate constant model best represents CO does not necessarily provide insight into CO's collisional energy transfer dynamics, since the rate constants themselves are highly averaged quantities. An expression linking the rate constants to the internuclear potential is outlined. The changes in the rotational populations hint at the roles of single and multi-quantum RET in CO. Specifically, the data reveal a preference for even- ΔJ transitions between low-lying rotational levels. Such a preference allows one to make qualitative observations about the intermolecular potential. The linewidth measurements, initially considered a necessary evil, show that energy transfer, rather than angular momentum transfer, controls the likelihood of RET in CO.

FITTING LAW ANALYSIS

Table 17 gives the model parameters resulting in the least error when fit simultaneously to all three pump-probe data sets (see Table 5 in Chapter 2 for rate constant expressions). To find the parameter uncertainties, each parameter was adjusted (holding all other parameters constant) until the total error increased by 10% beyond its minimum value. In Table 17, parameter d for the ECS-EP law represents l_c . The negative value of b for the ECS-EP law is a result of allowing the parameters to freely vary. During the MEG fit, including the homonuclear propensity term invariably increased error, hence the value of zero for d .

Table 18 gives the model parameters found in the literature. The literature parameters are based on self-broadening coefficients of the Raman Q-branch. Published parameter values for the SPG model were not found, likely because the SPG model does not accurately predict RET in CO as shown by its large error in Fig. 63. Figures 63 and 65 show the error stems mainly from the SPG model's inability to reproduce rapid decay

Table 17. RET model parameters.

Model (w/o uncertainty)	a (cm ³ /molec·sec)	b	c	d
SPG	$2.01^{+0.28}_{-0.19} \times 10^{-9}$	$1.137^{+0.023}_{-0.025}$	431^{+106}_{-311}	$8.90^{+1.80}_{-0.32}$
SPEG	$4.09^{+0.26}_{-0.24} \times 10^{-10}$	$0.553^{+0.013}_{-0.014}$	$0.836^{+0.050}_{-0.050}$	$0.81^{+0.37}_{-0.54}$
ECS-EP	$1.07^{+0.07}_{-0.06} \times 10^{-10}$	$-0.016^{+0.027}_{-0.025}$	$0.872^{+0.012}_{-0.012}$	$18.5^{+9.9}_{-9.9} \text{ Å}$
MEG	$9.14^{+0.67}_{-0.65} \times 10^{-11}$	$1.216^{+0.049}_{-0.058}$	$0.588^{+0.036}_{-0.036}$	0
Model (with uncertainty)	a (cm ³ /molec·sec)	b	c	d
SPG	$2.15^{+0.15}_{-0.17} \times 10^{-9}$	$1.148^{+0.018}_{-0.014}$	446^{+67}_{-96}	$8.90^{+0.36}_{-0.20}$
SPEG	$3.88^{+0.15}_{-0.16} \times 10^{-10}$	$0.530^{+0.009}_{-0.008}$	$0.870^{+0.035}_{-0.030}$	$0.80^{+0.18}_{-0.22}$
ECS-EP	$1.10^{+0.03}_{-0.04} \times 10^{-10}$	$-0.010^{+0.009}_{-0.014}$	$0.872^{+0.007}_{-0.005}$	$21.5^{+9.7}_{-9.7} \text{ Å}$
MEG	$9.44^{+0.32}_{-0.29} \times 10^{-11}$	$1.205^{+0.025}_{-0.025}$	$0.580^{+0.016}_{-0.016}$	0

Table 18. Literature RET model parameters.

Model	a (cm ³ /molec·sec)	b	c	d	Ref.
SPEG*	7.75×10^{-11}	0.2646	1.295	n/a	[38]
ECS-EP	$1.227 \pm 0.012 \times 10^{-11}$	0.0543 ± 0.0021	0.7539 ± 0.0043	$5.45 \pm 0.65 \text{ Å}$	[39]
MEG*	1.59×10^{-11}	1.312	1.397	n/a	[37]

Uncertainty not given in the literature.

in the rate constants with increasing ΔJ . A comparison between the literature and pump-probe SPEG results is difficult because the literature values were obtained by limiting RET to ΔJ -even transitions only. The addition of the homonuclear propensity term H in the pump-probe fits is not as harsh a restriction since H approaches unity with increasing ΔE .

There is a marked difference between literature and pump-probe ECS-EP parameters. The ECS-EP fit to the pump-probe data results in a much larger *a* parameter and a negative *b* parameter. The larger *a* parameter indicates RET is more probable than one would predict based on linewidth measurements alone. The negative *b* parameter unreasonably implies the probability of RET increases with ΔE . Given its uncertainty, *b*'s value is most likely close to zero, suggesting RET in CO is better described with an

ECS-P model. The pump-probe's larger l_c value is reasonable. Belikov and Smith found an interaction length of 6.6 Å when applying the ECS-EP model to collisions between CO and Ar [51]. Since dipole-dipole interactions occur during CO-CO collisions, one expects l_c for CO-CO interactions to be larger than 6.6 Å. The upper error limit on l_c in Table 17 was set to infinity as increasing the value of l_c to 10^{10} raised the total error by less than one percent.

Like the ECS-EP model, fitting the MEG model to the pump probe data gives a much larger a parameter. The c parameter in Table 17 is also smaller, implying multi-quantum transitions play a larger role in RET than one would predict based on linewidth measurements alone. That the MEG model gives useful RET rate constants with only three parameters is impressive, especially when noting the model's greatest errors occur when predicting the most questionable populations: $J_{P1} = 0$ and $J_{R13} = 14$.

The fitting results presented here do not decisively show which model best represents CO's RET rate constants. Further pump-probe measurements should make the distinction between models more clear, especially measurements associated with R1, R2, and R3 pumps where differences between even and odd ΔJ transitions among low-lying rotational levels should be evident. A more sophisticated expression for H should also make the SPEG model more competitive. Despite the usefulness of the rate constant models, the rate constants themselves are highly averaged quantities, and knowing their values does not allow one to unambiguously determine the CO-CO intermolecular potential. The next section discusses the connection between the intermolecular potential and the rate constants. The discussion introduces the impact parameter, a concept relied on heavily throughout the rest of the chapter.

RATE CONSTANTS AND THE INTERMOLECULAR POTENTIAL

Figure 66 identifies the variables used to describe the interaction between two molecules [57]. In the figure, the two-body problem has been reduced to a single-body problem by moving to the center-of-mass reference frame. The relative motion of the two-bodies is represented by the motion of a single body that approaches the origin along

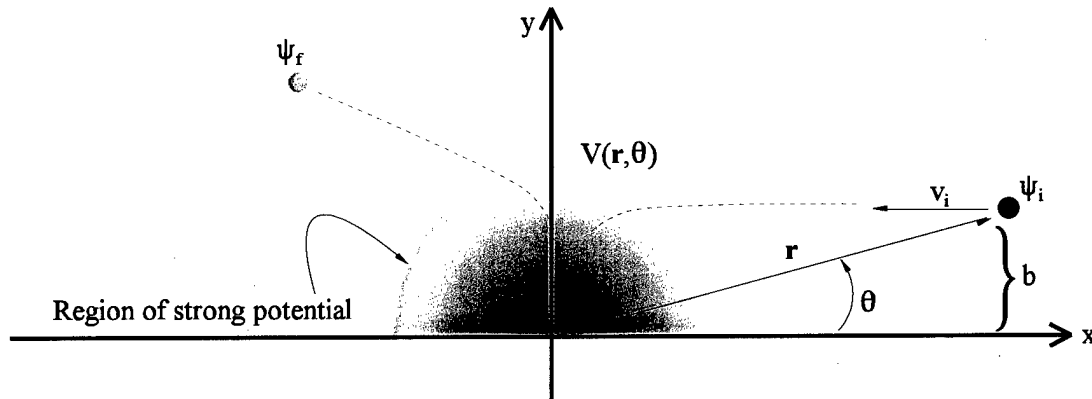


Figure 66. Center-of-mass coordinate system for a bimolecular collision.

a path parallel to the x-axis. As the body approaches the origin, it is subject to the potential $V(r, \theta)$. The impact parameter b is defined as the particle's distance from the x-axis in a region where $V(r, \theta) \approx 0$. When b is large, only weak forces act on the particle as it nears the origin are weak. When b is small, the forces are much stronger. The labels ψ_i and ψ_f specify the initial and final internal energy states of the particle. If $V(r, \theta)$ is known, the initial conditions (b, v_i) determine the particle's final trajectory. With the assumption that $V(r, \theta)$ perturbs the particle's internal energy states without affecting the final trajectory, the initial conditions (b, v_i) also determine the probability $P_{ij}(b, v_i)$ of the particle going from state ψ_i to state ψ_f . The effect of $V(r, \theta)$ on the $\psi_i \rightarrow \psi_f$ transition is embedded in $P_{ij}(b, v_i)$.

A molecule immersed in a bath of other molecules will undergo collisions having all possible values of b and v_i . Restricting the analysis initially to collisions with initial velocity v_i , the likelihood of going from ψ_i to ψ_f , assuming random impact parameters, can be expressed as a cross section given by

$$\sigma_{ij}(v_i) = \int_0^\infty P_{ij}(b, v_i) 2\pi b db. \quad (5.1)$$

With Eq. (5.1), the number of molecules in a volume V going from ψ_i to ψ_f can be calculated. If N_i is the number density of molecules in ψ_i and M is the number density of

bath molecules, the change in N_i is given by

$$\Delta N_i \cdot V = -(N_i \cdot V)(M \cdot V) \cdot \left[\frac{\sigma_{ij}(v_i) v_i \Delta t}{V} \right]. \quad (5.2)$$

The product $(N_i \cdot V)(M \cdot V)$ is the number of interacting systems while the ratio in square brackets is the fraction of successful interactions that occur in time Δt . Because the molecules have a range of velocities, the velocity must be averaged over all v_i . Averaging over v_i and taking the limit as $\Delta t \rightarrow 0$ leads to

$$\frac{dN_i}{dt} = - \left[\int \sigma_{ij}(v_i) v_i f(v_i) dv_i \right] N_i M \quad (5.3)$$

where $f(v_i) dv_i$ is the fraction of molecules with a velocity between v_i and $v_i + dv_i$. The term in square brackets in Eq. (5.3) is the rate constant k_{ij} where j is the rotational energy state of ψ_j . The relation between the rate constants and the intermolecular potential is given by

$$k_{ij} = \int v_i f(v_i) dv_i \int P_{ij}(b, v_i) 2\pi b db \quad (5.4)$$

where $P_{ij}(b, v_i)$ is a function of the unknown $V(r, \theta)$. Eq. (5.4) shows that while knowledge of $V(r, \theta)$ allows one to calculate k_{ij} , the converse is not true.

ROTATIONAL POPULATIONS

Three pump transitions were chosen for the experiment: P1, R6, and R13. The P1 pump revealed the peculiarities of transitions between rotational levels with small energy gaps. Pumping into $J = 0$ also avoided magnetic sublevel alignment. The R6 pump made the pump bandwidth measurement possible since $J = 7$ has a large equilibrium population at room temperature. RET out of $J = 14$ was investigated to observe the effect of larger energy gaps and because $J = 14$ was near the probe laser's detection limit. As seen in Figs. 60 - 62, the data sets of all three pump transitions share

two common features: peaks in the populations of levels neighboring the pumped level and population growth rates that diminishes with distance from the pumped level.

A population peak occurs when a level's population rises beyond the value associated with thermal equilibrium. Peaks are caused by large numbers of molecules migrating through levels adjacent to the pump. The relative positions of the peaks give insight into the balance between single and multi-quantum transitions. That the peaks appear later the further a level is from the pumped level suggests $\Delta J = 1$ transitions occur most often. But the peaks also rapidly dissipate signifying a substantial contribution from $\Delta J > 1$ transitions. Surprisingly, closer proximity to the pumped level does not guarantee a greater peak population as seen in the top left graph of Fig. 60 and in the bottom left graph of Fig. 62. In those figures, $J_{P1} = 2$ and the $J_{R13} = 12$ populations have greater peak populations than the $J_{P1} = 1$ and $J_{R13} = 13$ levels respectively. This implies that the $\Delta J = 2$ rate constants linking the levels are as large or nearly as large as the $\Delta J = 1$ rate constants. The population in $J_{R6} = 5$ does not exceed that in $J_{R6} = 6$ but its growth rate is the same.

A level's population growth rate generally diminishes the further the level is from the pumped level. The exceptions occur with $\Delta J = 2$ transitions out of the pumped level. For example, populations in $J_{R13} = 12$, $J_{R6} = 5$, and $J_{P1} = 2$ increase as fast as populations in $J_{R13} = 13$, $J_{R6} = 6$, and $J_{P1} = 1$ respectively. In the last case, $J_{P1} = 2$ rises faster than $J_{P1} = 1$. The high peak populations and equivalent growth rates in $\Delta J = 2$ transitions from the pumped level are evidence of homonuclear propensity in CO. Linewidth measurements support this conclusion.

LINEWIDTHS

The pump laser's sub-Doppler bandwidth sets the initial absorption linewidth of the molecules excited into the pumped level. At a probe wavelength of 4.8 microns, the nascent excited-state absorption linewidth is ~ 70 MHz. One should recognize that the pump leaves the velocities of the molecules excited into $v = 2$ unchanged. The excited state's sub-Doppler absorption linewidth is due instead to the pump preferentially promoting molecules traveling at right angles its propagation axis. Collisions broaden the

absorption linewidth by randomizing the velocity directions of the excited-state molecules. Because redirecting a molecule requires a significant exchange of linear momentum, collisions that broaden the absorption lineshape will have small impact parameters.

RET occurs simultaneously with the velocity re-direction, and the sub-Doppler linewidths of the non-pumped levels in Figs. 36 - 42 show that molecules retain a portion of their original velocity direction during rotational relaxation. The persistence of a sub-Doppler linewidth after RET implies rotational relaxation can occur at large impact parameters where the forces are too weak to significantly alter a molecule's velocity. The data in Fig. 67 help confirm this conclusion. The figure shows that by the third hard-sphere collision the majority of rotational relaxation is complete while velocity relaxation is only half finished. Rotational relaxation is faster than velocity relaxation because RET collisions are more frequent which could only be true if RET took place at large as well as small impact parameters. The mechanism for the long-range interaction is CO's permanent dipole moment.

The relative size of the impact parameter required to move, in a single collision, from the pumped level to a second level can be inferred from the second level's initial linewidth. As an illustration, Fig. 57 shows that populations in levels far removed from the pumped level begin growing simultaneously with populations in levels adjacent to the pumped level. For molecules to reach distant levels in so short a time, they must have undergone a single multi-quantum transition. Because the strong torques required for large RET occur at small impact parameters where velocity re-direction is most efficient, the initial linewidth of molecules in distant levels should be high. The initial linewidths in Fig. 46 verify this expectation.

An oddity in Fig. 46 is the linewidth difference between $J_{p1} = 1$ and $J_{p1} = 2$. The narrower linewidth of $J_{p1} = 2$ indicates the collisions transferring molecules into that level have larger impact parameters than the collisions transferring molecules into $J_{p1} = 1$. This seems contradictory since the $J = 0 \rightarrow 2$ energy gap of 11.3 cm^{-1} is nearly three times

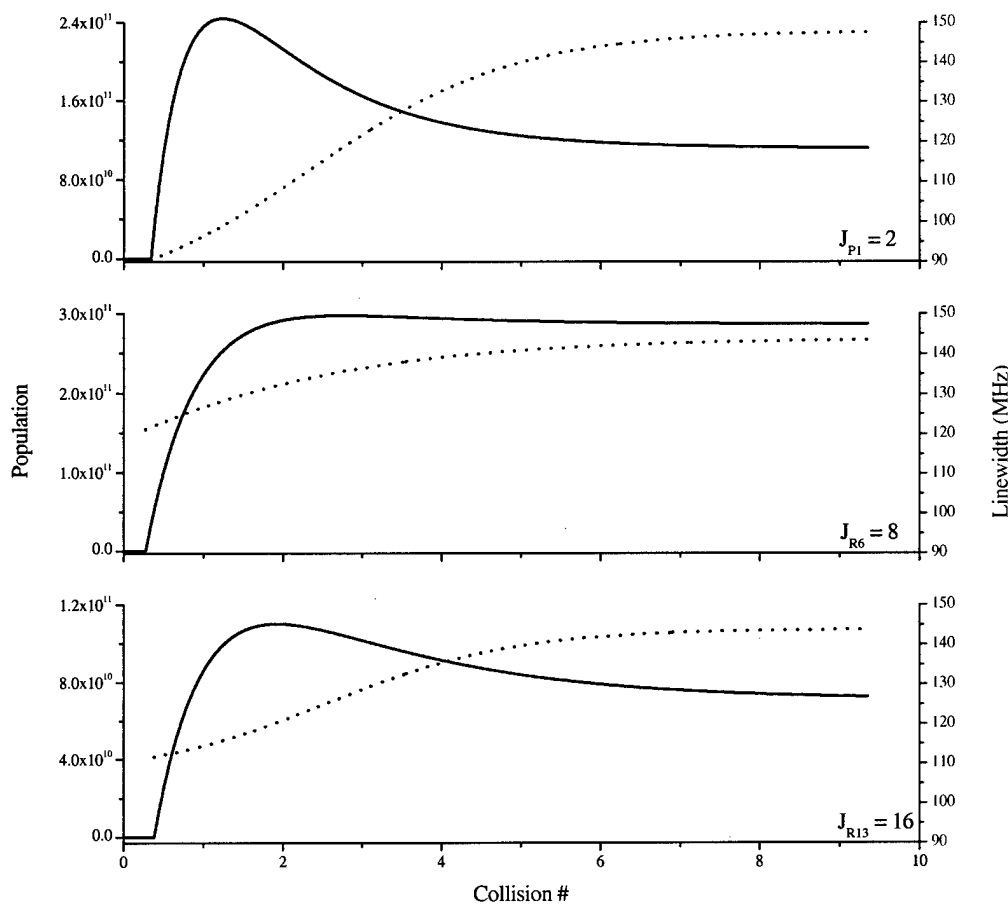


Figure 67. The relative speeds of rotational and velocity relaxation.

greater than the $J = 0 \rightarrow 1$ energy gap of 3.8 cm^{-1} . The narrower initial linewidth, faster population rise, and greater peak population of $J_{P1} = 2$ compared to $J_{P1} = 1$ are clear evidence of homonuclear propensity in CO.

HOMONUCLEAR PROPENSITY AND THE INTERMOLECULAR POTENTIAL

The intermolecular potential of homonuclear molecules is symmetric. In a Legendre-polynomial expansion of a symmetric potential, the odd terms in the expansion and the odd- ΔJ transitions associated with them disappear. In a near-homonuclear molecule such as CO where the sizes of the atoms and the number of electrons

surrounding them are similar, the differences between atoms becomes less visible the further one is from the molecule. Symmetric terms in CO's potential will therefore dominate at large impact parameters. As the impact parameter shrinks, the distinction between the C and O atoms becomes more apparent and odd terms contribute to the potential. The larger linewidth of $J_{p1} = 1$ compared to $J_{p1} = 2$ shows the $\Delta J = 1$ transition required a smaller impact parameter than the $\Delta J = 2$ transition. This is easily explained if symmetric terms in the CO-CO intermolecular potential dominate at large impact parameters. Fig. 46 shows the linewidth of $J_{p1} = 4$ is broader than that of $J_{p1} = 3$ suggesting that homonuclear propensity is quickly lost as ΔJ increases. Restricting a rate constant model to even- ΔJ transitions, shown by Looney et. al. to help predict the collapse of Raman Q-branch linewidths at high pressure, is a more extreme measure than the pump-probe data warrant. The homonuclear propensity term H added to the fitting laws attempts to account for the loss of homonuclear propensity with increasing ΔE .

THE DOMINANT FACTOR: ΔJ OR ΔE

Whether an increasing energy gap or an increasing change in angular momentum controls the likelihood of RET has been discussed by McCaffery et. al. [58]. The rate constant models introduced in Chapter 2 assume ΔE is most important when calculating the rate constants. McCaffery proposed a model that assumes ΔJ controls RET. With the angular momentum model, McCaffery derived an exponential-decay dependence of the rate constants on ΔJ . The linewidth data however suggests a ΔE -based model is most appropriate for CO. If RET was controlled by ΔJ , collisions at large impact parameters should induce $J_{R13} = 14\rightarrow16$ transitions (116.8 cm^{-1} energy gap) as easily as they induce $J_{p1} = 0\rightarrow2$ transitions (11.3 cm^{-1} energy gap). But measurement shows molecules entering $J_{R13} = 16$ have attained 80% of their final linewidth as opposed to 60% in the $J_{p1} = 2$ case. A rate constant model based on ΔJ does not explain the smaller impact parameters required to drive molecules into $J_{R13} = 16$ while a ΔE -based model does.

FUTURE WORK

None of the fitting laws stood out as best representing CO. Pumping into additional levels should provide a better test of the fitting laws, especially if pumping into $J = 1, 2$, and 3 continues to show homonuclear propensity. Diluting the CO with nitrogen would remove the effect of the dipole moment on RET while preserving linear momentum exchange and the possibility of resonant rotation-to-rotation energy exchange. Using atomic diluents such as Neon or Argon would remove both the effect of CO's dipole moment and the possibility of rotational energy exchange while keeping the mass of the collision partner similar. Using Helium and H_2 diluents would allow a test of theoretical potential calculations. Repeating the experiments at liquid nitrogen and elevated temperatures would provide additional rate constant information that can be linked to collision cross-sections.

CONCLUSION

This has been the most extensive pump-probe experiment performed on CO. It gives direct evidence for homonuclear propensity in CO and shows homonuclear propensity is restricted to small-energy-gap transitions. The linewidth data identify ΔE as the dominant factor determining the probability of RET in CO. Peaks in the populations and the population growth rates suggest RET is faster and that multi-quantum transitions are more important than one would anticipate based on linewidth measurements alone. The results of the rate constant model fits support this assertion. The relative speeds of rotational and velocity relaxation imply RET will help prevent a high-energy pump pulse from saturating an absorption transition, even if the pulse bandwidth is sub-Doppler.

LIST OF APPENDICES

Appendix A: Computer Study of Optical Pumping	132
Appendix B: The Pump Source for Optical Pumping	138
Appendix C: Coherent Effects in CO	140
Appendix D: OPO Calculations	147
Uniaxial and Biaxial Crystals.	147
Light Propagating Through Uni- and Biaxial Crystals	149
Phase Matching Angles	151
Efficiency	153
The Initial OPO Configuration	153
Appendix E: Mode Matching Circuit	157

APPENDIX A: COMPUTER STUDY OF OPTICAL PUMPING

A justifiable concern is whether optical pumping, even under ideal circumstances, can produce a high-energy CO laser with output at 4.7 microns. The AFRL developed a computer code to model optical pumping. The code predicts pump absorption, population dynamics, and subsequent lasing intensities while accounting for rotational and vibrational relaxation. When compared to data obtained in optical pumping experiments at AFRL, the model shows fair predictive ability [24]. In what follows, model predictions illustrate the scaling potential of CO and highlight the role of RR.

The model assumes an ideal pump laser that produces 5 J of narrowband energy—200 MHz FWHM—with a 6 ns temporal width. The ideal pump is actually a 50 \times scaled version of a 100-mJ OPO already in use at the laboratory. Figure 68 shows the experimental configuration modeled by the computer code and Table 19 gives the code inputs.

The cell and cavity lengths were chosen to allow maximum pump absorption while keeping the size of the laser reasonable. A CO pressure of 50 torr gives an estimated vibrational relaxation time of around 230 ns. Lasing must occur before this time to prevent energy loss to higher vibrational levels where the optical transitions are at longer wavelengths. The R(0) transition was chosen to highlight rotational relaxation

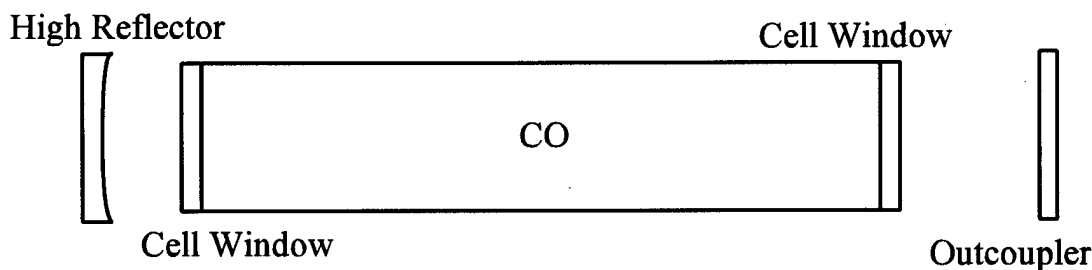


Figure 68. The experimental set-up modeled in the AFRL computer code.

Table 19. AFRL Code Program Inputs.

Cell Length	75 cm	
Cavity Length	100 cm	
CO Pressure	50 torr	
Wavelength	2.3 μ m	4.7 μ m
High Reflector Transmission	0.98	0.01
Cell Window Transmission	0.96	0.98
Outcoupler Transmission	0.02	0.50
Pump Duration (FWHM)	6 ns	
Pump Energy	5000 mJ	
Transition R(0)	$v, J=0,0$ to $v, J=2,1$	
Temperature	300K	
He diluent pressure	variable	
Pump diameter	variable	

effects. To simplify the code, a stable resonator was modeled. An actual device would employ an unstable resonator since optically-pumped CO lasers are high gain systems.

The first thing noticeable with a 5 J pump energy is that the pump saturates the absorption transition. Saturation occurs when the upper and lower rotational state populations linked by the pump radiation are equal (ignoring degeneracy factors). Rotational relaxation is an important mechanism that can delay or even eliminate saturation. RR prevents saturation by transferring molecules out of the pumped upper state population and feeding molecules into the depleted lower state population. Figure 69 shows the difference in the computer model's absorption predictions when rotational relaxation is accounted for and when it is not. CO would absorb much more energy on an R(6) or R(7) transition because of the much greater populations in the $J = 6$ and 7 states at 300K, but the benefits of rotational relaxation would not be as immediately apparent.

Adding a diluent such as helium to the gas mixture increases rotational relaxation further. Diluent improves the relaxation rate without increasing vibrational losses.

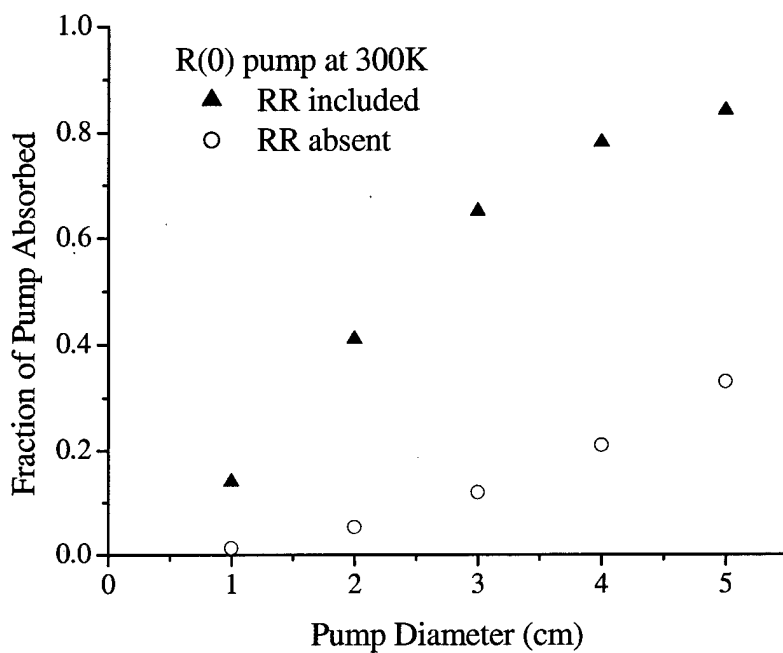


Figure 69. 5-J predicted absorption. The graph shows the predicted absorption of the 5-J pump beam as a function of pump diameter when rotational relaxation (RR) is and is not accounted for.

Figure 70 shows how diluent affects absorption given a 1-cm diameter or 5-cm diameter pump. In the 1-cm case, saturation remains a problem and rotational relaxation improves absorption out to 100 torr. In the 5-cm case, expanding the beam has already reduced saturation to the point where faster rotational relaxation shows little benefit. In fact, increasing diluent pressure to raise the rotational relaxation rate broadens the absorption bandwidth, driving down the peak value of the absorption cross section. The net result is less absorption.

While declining absorption suggests the diluent pressure ought to be kept low, the problem of ASE argues for increasing diluent pressure further. Increasing the rotational relaxation rate by raising the diluent pressure reduces the gain by distributing it over many different lasing lines. To see how rotational relaxation prevents ASE, consider an intense narrowband pump that selectively places a large number of molecules into a

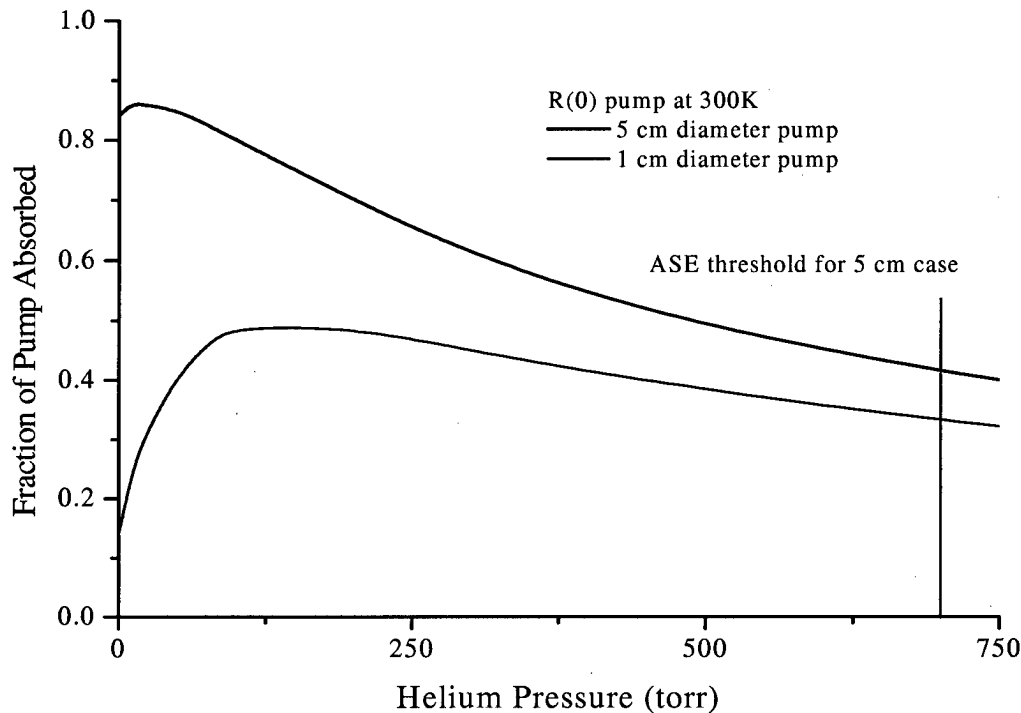


Figure 70. ASE threshold. The curves show predicted absorption as a function of diluent pressure at two different pump diameters. At pressures below the ASE threshold, ASE is predicted to remove much of the energy deposited into the gas by the pump.

single rotational state. If rotational relaxation doesn't remove molecules from the state fast enough, gain builds to values well over 1000% per centimeter. By increasing diluent pressure, the rotational relaxation grows to the point that it removes molecules from the pumped rotational state as fast as the pump deposits them. By transferring molecules into adjacent rotational levels, rotational relaxation spreads the gain among many different transition lines so that the gain on any one line remains moderate.

Analytic expressions for ASE intensity typically involve the saturation intensity for cw lasers [59] or saturation fluence for pulsed lasers [60]. The present AFRL code does not directly account for ASE, but it can be used to estimate when ASE becomes significant. Under conditions known to produce ASE, the code predicts a negligible time delay between the pump pulse and subsequent laser pulse. This suggests that when the

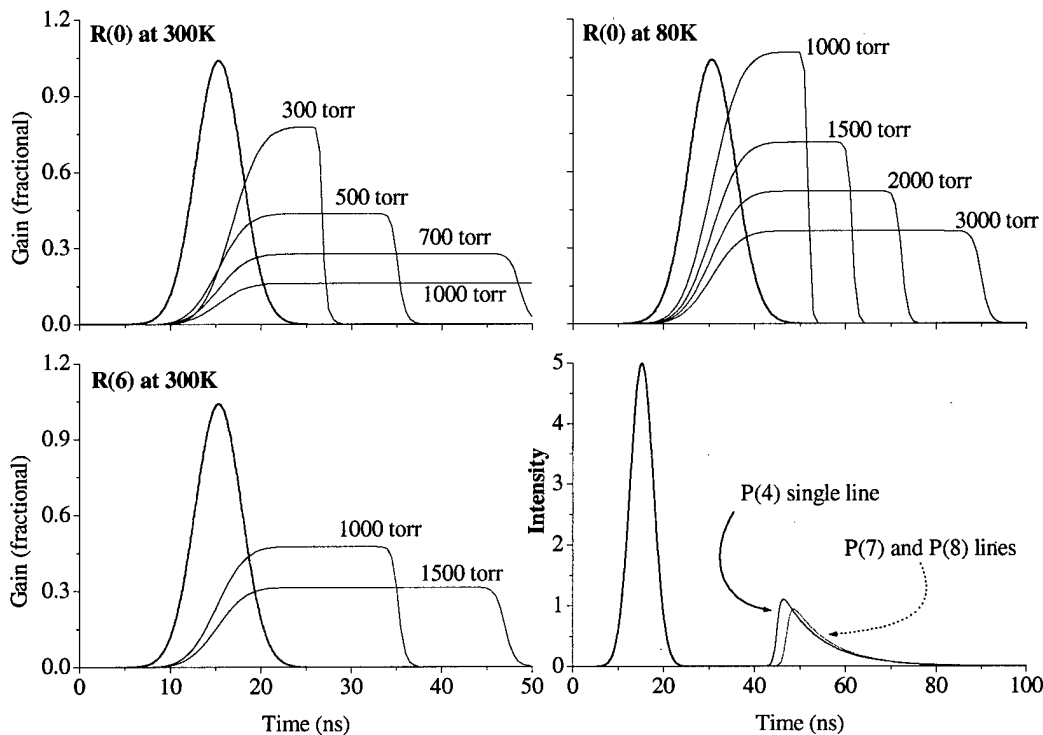


Figure 71. Diluent effects. All but the bottom right graph show how gain between $v = 2$ and $v = 1$ changes with time. The gain drops to zero when the laser pulse is emitted. The blue line in each case represents the pump. The bottom right graph shows the pump and the predicted lasing pulse. The y-axis scale in the bottom right graph was altered so the y-value at each pulse's peak represents the pulse energy.

code predicts an extended delay, say around four cavity round trip times, ASE losses will be small. Applying this qualitative but reasonable delay rule to the code output, ASE losses become negligible when the gain per unit length (cm^{-1}) is approximately 35%.

Figure 71 shows calculated gain as a function of time for various transitions, temperatures, and diluent pressures. In all four graphs, the blue line represents the pump pulse. The black curves trace the gain as a function of time. The CO laser pulse begins when the gain drops off suddenly. The top left graph shows gain on the P(8) line at 300K¹. The delay between pump and output reaches 25 ns at around 700 torr of helium . Though ASE is minimized at this pressure, absorption of the R(0) pump is less than 50%. To test whether absorption could be increased while maintaining a high diluent pressure,

¹ Despite an R(0) pump, gain remains highest on the P(8) because of rapid RR.

a low temperature case more suited to an R(0) pump was studied. The top right graph of Fig. 71 shows gain on the P(4) line at a gas temperature of 80K. Note in this case that the desired delay comes at 3000 torr of diluent pressure. Despite the high diluent pressure, pump absorption remains at 91% because CO number density in the J = 0 state is greater at lower temperatures. To test whether CO could absorb most of the pump energy while at room temperature, an R(6) pump transition was selected. The lower left graph shows gain on the P(8) line again but this time with an R(6) pump. The 25-ns delay occurs at 1500 torr of diluent pressure with a pump absorption of 88%.

Predicted lasing intensity is shown in the lower right graph of Fig. 71. The y-axis was scaled so the value at the pulse peak is the pulse energy. This last graph illustrates the final benefit rotational relaxation has on laser output—single line lasing. As the diluent pressure is increased, the gain saturates more homogeneously and the number of competing lasing lines diminishes. In the room temperature R(6) pump case, significant lasing occurs only on the P(7) and P(8) lines. In the 80K R(0) pump case only the P(4) line lases. In either case the energy efficiency (E_{out}/E_{in}) is around 20%. The computer study indicates that with a suitable pump, CO can absorb large amounts of optical energy, store it without significant loss (ASE or V-V), and finally release the energy on a single line at 4.7 microns. The key element in each step is rotational relaxation.

APPENDIX B: THE PUMP SOURCE FOR OPTICAL PUMPING

The first and probably most difficult problem associated with optical pumping is finding a good pump source. For CO, the essential elements of an efficient, compact, and scalable optical pump already exist in industry: diode-pumped fiber lasers. Two types of fiber lasers could optically pump CO: erbium-doped fiber lasers operating at 1.57 microns and thulium-doped fiber lasers operating at 2.35 microns.

The optical communications industry has extensively researched and developed erbium-doped fiber lasers/amplifiers because they operate at the 1.57-micron transmission window in glass. Fortunately, 1.57 microns also happens to be the resonance wavelength for the $v = 0$ to $v = 3$ second overtone transition in CO. One advantage of switching to the 0-3 transition is improved photon efficiency—cascade lasing can occur on the 3-2 and 2-1 transitions. The main drawback to the 0-3 transition is the $150 \times$ reduced absorption cross section. However the loss in absorption cross section can be offset somewhat by cooling the CO to 70K. For example, the intensity absorption coefficient² α drops from a value of 0.384 on the R(7) transition at 300K to a value of 0.037 on the R(3) transition at 70K—a factor of 10 instead of 150. Narrow 60-MHz bandwidth operation has already been demonstrated with erbium-doped fiber lasers [61] as has 10-ns pulsed operation [62]. Single-mode pulse energies on the order of 1 mJ were reached [63] with much greater energies expected from multi-mode beams. Thulium-doped fiber lasers operating at 2.35 microns—the first overtone 0-2 transition in CO—are another possible option. Though reports of pulsed operation were not found for thulium-doped fiber lasers, cw thulium lasers could serve as a pump.

It is questionable question whether cw lasing in CO can be restricted to 4.7 microns given rapid vibrational relaxation. The answer is yes provided supersonically expands the gas to cool it and to convert vibrational relaxation time into a distance. Cooling the gas reduces the number of available rotational states so the CO number density in the low lying J states grows. Besides making the short-wavelength optical

² Defined according by the relation $I(x) = I(0)e^{-\alpha x}$.

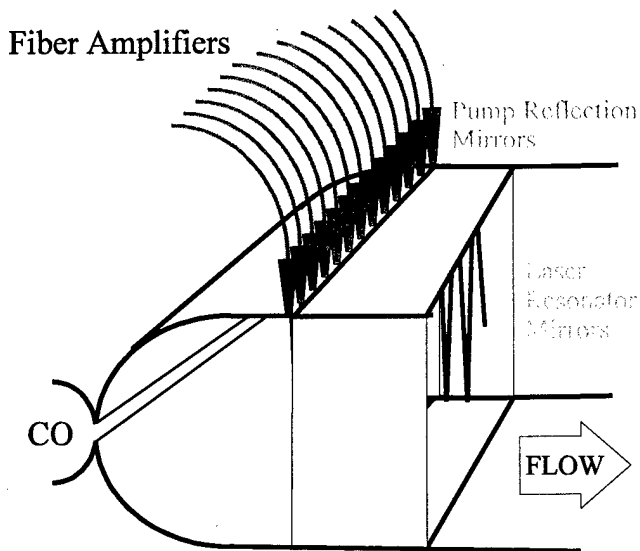


Figure 72. Pump concept. The diagram shows a pumping scheme for an optically pumped cw CO laser. The CO gas is cooled by passing through a supersonic slit nozzle. Pump light from the fiber amplifiers (the red lines) bounces off highly reflective mirrors (blue) many times for maximum absorption by CO. The laser resonator formed by the grey mirrors goes into and out of the page.

transitions more likely, supersonic expansion allows the laser to operate at lower pressures, and lower pressures mean longer vibrational relaxation times. If the gas speed is fast enough (speed can be increased by using a low molecular weight diluent such as H₂) the vibrational relaxation time can be converted into a distance of several centimeters. CW pumping has the additional advantage of eliminating ASE problems, since once lasing begins, stimulated emission saturates the gain. Finally, if wavelength selective elements are used in the resonator, it may be possible to lase on the 1-0 fundamental in addition to the 2-1 and 3-2 fundamentals. Figure 72 shows one possible pumping scheme for cw optical pumping.

APPENDIX C: COHERENT EFFECTS IN CO

The model predicting how much pump energy the CO absorbs assumes that rate equations adequately describe the photon and molecule populations as a function of time. Under the low CO pressure conditions required to measure the rotational relaxation rate constants, this may not always be the case. When the mean time between collisions is long compared to the duration of the pump pulse, the methods of quantum mechanics are needed to describe the populations. Quantum mechanics accounts for possible prolonged coherence between the electric field of the pump pulse and the dipole moments it induces in the molecules. Prolonged coherence between the field and molecular dipole moments would show itself as an oscillation in the absorbed pump energy between 0 and 100% with increasing pump energy. The possibility of observing coherence effects in CO was considered by Brechignac but never experimentally observed. The presence of coherence, while interesting, posed more of a nuisance to the experiment than anything else. Time was spent studying the conditions under which prolonged coherence occurs to avoid confusion later if unexpected results were observed.

Coherence is most often associated with objects like waves having properties that oscillate with time. Two or more oscillating quantities are coherent if the phases of their oscillation are related in a non-random way. As examples, consider temporal and spatial coherence between light waves. The light's electric field is temporally coherent if, at the same position, the phase of the electric field at two different times is related. The field is spatially coherent if, at the same time, the phase of the electric field at two different positions is related. Oscillating quantities do not have to be identical for coherence to exist between them—the dipole moment of a molecule or group of molecules can be coherently related to the oscillation phase of an external electric field [64]. This makes sense considering that the electric field may have induced the dipole moment in the first place, or that the oscillating dipole moment generated the electric field. The coherent relationship between an external electric field and the dipoles—atomic or molecular—causes the photon and excited-state molecule populations to fluctuate in ways rate equations cannot describe.

An external electric field from a laser pulse displaces a molecule's electrons from their equilibrium position and induces a dipole moment. The spatial extent of the electric field is enormous compared to the spacing between molecules so that the electric field induces a similar dipole moment in large number of molecules. Shimoda³ labels the related phase and direction the induced dipole moments share with the external field as coherence. The coherent way molecules respond to the electric field—as described by their dipole moment—can be calculated quantum mechanically.

The quantum expectation value of the dipole moment is given by

$$\langle \mu \rangle = \langle \Psi | \mathbf{e} \mathbf{x} | \Psi \rangle = \int \Psi \mathbf{e} \mathbf{x} \Psi d^3x \quad (C1)$$

where e is the charge on an electron, $\mathbf{x}(t)$ is the displacement of the electron or electrons from the charge center, and $\mu(t) = e \cdot \mathbf{x}(t)$ is the classical value of the dipole moment. Ψ is the state vector describing the energy states of the molecular system while under the influence of the electric field. The state vector must be a solution to the Schrödinger equation given by

$$i\hbar \frac{\partial \Psi}{\partial t} = \mathbf{H}\Psi. \quad (C2)$$

In Eq. (C2), \mathbf{H} is the system Hamiltonian given by $\mathbf{H} = \mathbf{H}_0 + \mathbf{H}_\mu$. \mathbf{H}_0 describes the internal energy of the isolated molecule and \mathbf{H}_μ describes the interaction energy between the molecule and the external field: $\mathbf{H}_\mu = -\mu(t) \cdot \mathbf{E}(t)$. The coherence between $\mu(t)$ and $\mathbf{E}(t)$ lies in the $\mu(t) \cdot \mathbf{E}(t)$ expression where the phase and direction of $\mu(t)$ is assumed to remain linked to the phase and polarization direction of $\mathbf{E}(t)$. It is assumed the dipole moments of the molecules with respect to each other remain coherent so the sum of all μ yields a non-zero, macroscopic, time-dependent dipole moment density $\mathbf{P}(t)$. A time-dependent \mathbf{P} generates an electric field that adds back to the original incident electric field

³See page 128 of Shimoda's text.

[65]. One can calculate the contribution of $\mathbf{P}(t)$ back on $\mathbf{E}(t)$ using Maxwell's wave equation (see the elementary laser texts by Shimoda and Verheyen). $\mathbf{E}(t)$ is assumed to be weak compared with the internal electric fields binding the molecule together such that H_μ is much less than H_0 . Because $H_\mu \ll H_0$, perturbation theory provides an approximate solution to Eq. (C2) made up of a time-dependent superposition of the stationary eigenstates associated with H_0 . The assumed solution to Eq. (C2) is given by

$$\Psi = c_1(t) \phi_1(r) + c_2(t) \phi_2(r) + \dots + c_n(t) \phi_n(r), \quad (C3)$$

where $\phi_n(r)$ are the time-independent eigenstates of H_0 and $c_n(t)$ are coefficients whose square magnitudes represent the probability of the system being in state n . The c -coefficients can also be interpreted as representing the probability of transitions between states. For example, if a molecule is initially in state $n = 1$, $|c_2(t)|^2$ represents the probability of a transition from $n = 1$ to $n = 2$.

Substituting Eq. (C3) into Eq. (C1), an expression for $\langle \mu \rangle$ in terms of the c -coefficients can be found. The same arrangement of c -coefficients making up the solution for the dipole moment also appears in the elements of the system's density matrix. The connection between the density matrix and the dipole moment permits use of the density matrix in place of the dipole moment in calculations. With the density matrix, incoherent relaxation mechanisms (like collisions) can be introduced that otherwise could not be practically incorporated into Eq. (C2) [66].

When a constant amplitude, uniform, resonant electric field is applied to an isolated, collision-free, two-state system, the molecular population oscillates *fully* between the ground and excited state with time. The frequency of oscillation is the Rabi frequency Ω_R given by $\Omega_R = \mu E / \hbar$ where μ is the dipole moment between the upper and lower state and E is the amplitude of the applied electric field. If the frequency of the electric field is not quite resonant with the transition, the molecules will no longer all enter the upper state and the back-and-forth frequency of those doing so will increase. If the amplitude of the applied field changes with time as it does for a traveling pulse, the

associated Rabi frequency becomes a function of time given by $\Omega_R(t) = \mu E(t)/\hbar$, and a quantity that better describes the pulse's effect on the state populations is the time integral of $\Omega_R(t)$ called the pulse area $A(z)$:

$$A(z) = \int \Omega_R(t') dt' = \frac{\mu}{\hbar} \int E(z, t') dt'. \quad (C4)$$

In Eq. (C4), z is the direction of pulse propagation. Instead of the molecules collectively oscillating between the ground and excited state as in the constant electric field amplitude case, in the pulsed case the populations oscillate with pulse area. In the late 1960s, S. L. McCall and E. L. Hahn derived and experimentally verified for a non-degenerate, decay-free, two-state system the McCall-Hahn area theorem [67][68]

$$\frac{dA}{dz} = -\frac{\alpha}{2} \sin A \quad (C5)$$

where A is the pulse area defined in Eq. (C4), and α is the inverse Beer's absorption length. The area theorem shows that for a small A , $\sin A \approx A$ and Beer's law absorption is regained. On the other hand if A is equal to or slightly less than π , the medium rapidly and completely absorbs the pulse. For a pulse with area greater than π , the change in area with distance is positive so that A increases until it reaches a value of 2π . When $A = 2\pi$, the area ceases changing and the pulse passes through the medium completely unabsorbed. Beyond 2π , the pattern repeats with 3π acting as the next threshold between decreasing and increasing area.

McCall and Hahn labeled the ability of an $A = 2\pi$ pulse to pass through an absorbing medium unabsorbed self-induced transparency (SIT). A description of SIT more related to laser theory assumes that the medium absorbs the first half of a 2π pulse through stimulated absorption and that the second half of the pulse removes the energy from the medium through stimulated emission.

Complete absorption of a π pulse or complete transmission of a 2π pulse is rare because it is difficult to achieve prolonged coherence between the pump field and the

induced dipole moments. Any process interrupting the phase or direction of a molecule's dipole moment with respect to the field or surrounding dipoles destroys the coherence by driving the value of \mathbf{P} toward zero. Spontaneous emission and collisions are two mechanisms that destroy coherence between the field and the dipoles.

Spontaneous radiative transitions disrupt coherence because their contribution to the electric field is random in direction and phase. To arrange an observable coherent interaction requires ensuring the interaction time τ between the field and the atoms is shorter than the radiative decay time T_1 given by the inverse of the transition's Einstein A coefficient. For transitions between metastable states, this condition is easily met. Preventing collisions is more difficult. Collisions can reorient a molecule's alignment with the electric field or change it's velocity so that the molecule is Doppler shifted out of resonance with the field. Collisions interrupt the phase of the molecule's dipole moment so that μ is no longer in step with \mathbf{E} or the neighboring molecules. Collisions can remove the molecule from the interaction by promoting it to a different state. Of the collision types listed, phase interrupting collisions are the most prevalent. To observe coherence when collisions are present, the pulse duration must be shorter than the mean time between collisions T_2' . T_2' can be roughly calculated by inverting the transition's homogeneous FWHM line width $\Delta\nu_H$ [69]:

$$T_2' = \frac{1}{\pi\Delta\nu_H}. \quad (C6)$$

The pump pulse bandwidth is another variable that determines the visibility of coherence between the molecules. A wide bandwidth pump interacts with a broad range of molecules causing resonance over many frequencies. Even without collisions, the destructive interference that develops between in-phase oscillators oscillating at different frequencies prevents coherent effects from being observed. The time T_2^* it takes destructive interference to hide the coherence signal is related to the FWHM inhomogeneous line width of the gas $\Delta\nu_I$ by

$$T_2^* = \frac{2\sqrt{\ln 2}}{\Delta v_1} \quad (C7)$$

where T_2^* is known as the inhomogeneous dephasing time.

Optimal conditions for observing coherence occur in the sharp line limit [70] when $\tau < T_1, T_2, T_2^*$ and in the broad line limit when $T_2^* < \tau < T_1, T_2$. Sharp and broad refer to the width of the absorption line compared to the bandwidth of the pulse. In the sharp line limit, the electric field interacts with all portions of the absorption line width, but because τ is much less than T_2^* the coherent interaction is finished long before inhomogeneous dephasing can occur. In the broad line limit, the pulse interacts with only a fraction of the total bandwidth associated with T_2^* so that τ and the actual inhomogeneous dephasing time are similar since the bandwidth of the molecules interacting with the field is equal to the bandwidth of the pulse.

Another reason one rarely sees coherence effects is the requirement for the transition to be between two isolated states. This restriction is violated if one or both of the states are degenerate. Any additional state, even a degenerate one, brings with it its own dipole moment, introducing an interference oscillation in the population fluctuations. As more degenerate states are added, the coherent interaction becomes indistinguishable from an incoherent one [71]. In certain cases, transitions between degenerate levels can still be described by an ideal two-state system: the R(0) or P(1) transitions between the rotational and vibrational levels of a diatomic molecule in its electronic ground state are one such case. Whether one chooses the R(0) or P(1) transition, one of the levels will be three-fold degenerate. In this case however the optical transition selection rules for polarized light— $\Delta m_j = +1$ for right circular polarization, $\Delta m_j = -1$ for left circular polarization, and $\Delta m_j = 0$ for either linear polarization—bypasses the degeneracy and allows a four-state system to act as a two-state system.

The final assumption implicit in the theory but difficult to achieve experimentally is the plane-wave nature of the electric field. With hot spots in the intensity profile of the pump beam, different regions of the gas will experience large and small pulse areas.

Without a detector sensitive to the energy distribution across the pump's spatial profile, the coherence effects would be lost to detector averaging.

In review, the experiment must meet the following conditions to produce visible coherence effects:

- 1) The transition must occur between two individual states.

In CO the transition must be non-degenerate requiring a R(0) or P(1) pump.

- 2) The pump duration τ must be shorter than the mean time between collisions.

In 2 torr, the collision time is 50 ns. The OPO pump pulse width is 6 ns.

- 3) Pump duration must be shorter than or equivalent to T_2^* .

The pump pulse frequency bandwidth is approximately 100 MHz compared to the 300 MHz Doppler linewidth of CO at 300K. Assuming an effective dephasing bandwidth of 100 MHz, $T_2^* = 17$ ns.

- 4) The pump duration must be shorter than the radiative decay time.

In CO for $v = 2 \rightarrow 1$ transitions, the radiative decay time is on the order of 30 ms.

- 5) The pump pulse must at least approximate a plane wave.

The spatial filter used to remove intensity hot spots in the OPO pump beam creates a nearly gaussian intensity profile. The spatial filter also removes nearly 90% of the pump's initial energy so that the average pulse energy reaching the CO is around 0.4 mJ.

- 6) The pump area must be large enough so that $\sin A \approx A$.

Given the pump diameter of 1.8 cm, a pulse energy of 0.4 mJ, and a dipole moment value calculated from the Einstein A coefficient [72], the average pulse area for an R(0) pump transition is 0.1π . $\sin(0.1\pi)/(0.1\pi) = 0.984$.

Efforts to observe coherent effects by reducing the beam diameter to 1.5 mm—where the pulse area was near π —failed because ASE began at a diameter of around 8 mm. The steps taken to avoid ASE place the experiment outside the realm where coherent effects such as SIT are visible.

APPENDIX D: OPO CALCULATIONS

The OPO as originally configured was made up of two resonators: one called the seed resonator and the other called the power resonator. The seed portion was the OPO described at beginning of Chapter 3. Additional information about OPOs in general follows.

Uniaxial and Biaxial Crystals.

The heart of an OPO system is the non-linear crystal found inside the OPO resonator. The crystal's non-linear properties allow it to convert light of a higher frequency into light with a lower frequency provided certain conditions are met. The OPO system described in Chapter 3 relies on KTP crystals to double the frequency of the Nd:YAG laser and to generate $2.3\text{ }\mu\text{m}$ light inside the OPO resonator. What follows is a brief review of the nomenclature one encounters when studying OPOs. It relies heavily on the text by Sutherland [73]. KTP is a biaxial (mm2 class) as opposed to uniaxial crystal. Uniaxial crystals are simpler so they are described first. Figure 73 depicts the atoms in a uniaxial crystal bonded together in a cubic lattice by forces represented as springs. A different spring type represents a different strength bond. Since the bonds in the x-y plane are identical, the crystal exerts a polarization-independent influence on a light field propagating along the z-axis characterized by a single principal index of refraction. For light traveling in other directions, the bonds along the z-axis add a polarization-dependent contribution to the crystal's response. Since the z-axis bonds differ from those in the x-y plane, a second principal index of refraction must be included to characterize the crystal's influence on the light.

Crystals like the one shown in Fig. 73 are called uniaxial crystals because there is only one direction of propagation through the crystal along which the light experiences a constant, polarization-independent refractive index. This unique propagation direction in uniaxial crystals is labeled the crystal Z-axis (or c-axis or optical axis).

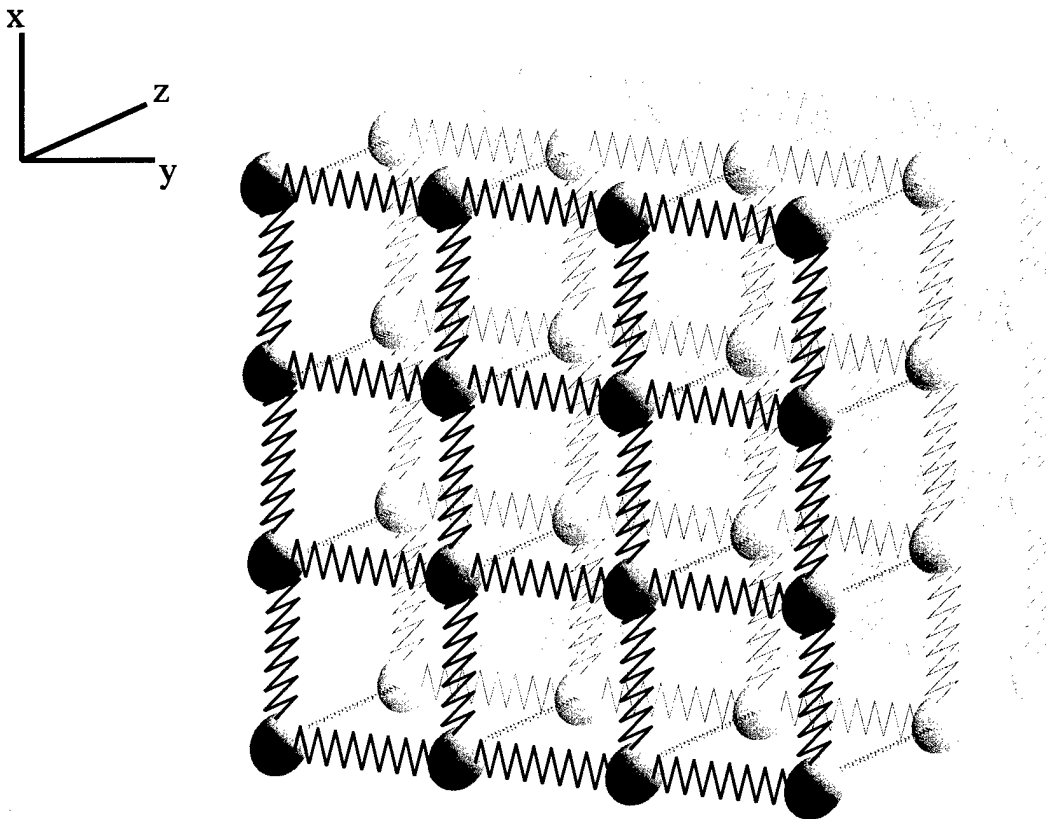


Figure 73. Uniaxial crystal. The diagram represents a uniaxial crystal. The dots represent atoms and the springs represent bonds between the atoms. The different spring types represent different bond strengths.

Figure 74 shows a more general case. Because there are three different spring types or bond strengths, the crystal's influence on light traveling through it is characterized by three different principal refractive indices. Crystals like the one shown in Fig. 74 are called biaxial crystals because there are two propagation directions along which the light can experience a constant, polarization-independent refractive index. The plane formed by the two optic axes is called the crystal X-Z plane, and the line bisecting the acute angle between the two directions is called the biaxial crystal Z-axis. (See Figure 16 on page 56 of Sutherland.)

Table 20 lists the KTP-F principal index values for each of the OPO wavelengths. These values came from Sandia National Laboratory's SNLO program⁴.

⁴ A free down-loadable program that calculates phase matching angles, walk-off, d_{eff} , etc. for more than 40 crystal types, both uniaxial and biaxial. One can use this program to independently check calculations. Go to <http://www.sandia.gov/search.html> and enter a search for snlo.

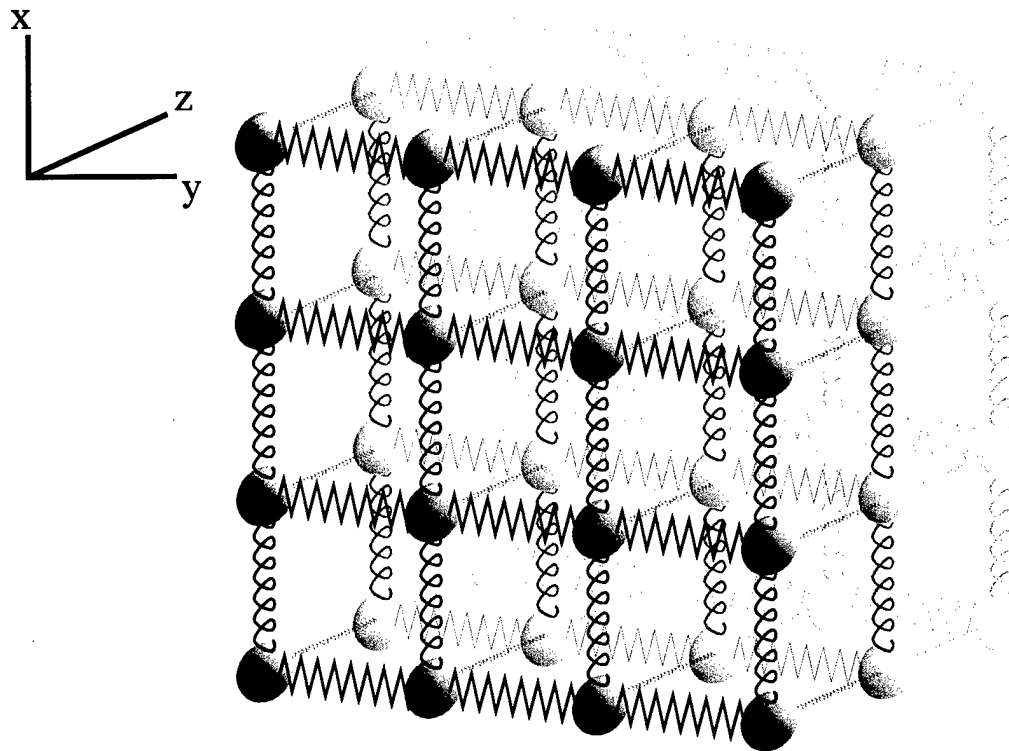


Figure 74. Biaxial crystal. A cubic biaxial crystal having three different spring types.

Light Propagating Through Uni- and Biaxial Crystals

Depending on its polarization, a light ray entering a uniaxial or biaxial crystal splits into two rays, with each ray having a polarization orthogonal to that of the other. To describe this effect mathematically, one must find a self-consistent monochromatic plane-wave solution to Maxwell's equations in non-magnetic, non-absorbing, non-conductive media. The result is an algebraic equation known as the Fresnel equation.

Table 20. Principal indices for KTP at the seed and power OPO wavelengths.

	532 nm	689 nm	1064 nm	1955 nm	2335 nm
n_x	1.77974	1.75847	1.74037	1.72321	1.71640
n_y	1.78977	1.76704	1.74787	1.72967	1.72242
n_z	1.88772	1.85545	1.82966	1.80683	1.79802

$$\frac{\sin^2(\theta)\cos^2(\phi)}{n^2 - n_x^2} + \frac{\sin^2(\theta)\sin^2(\phi)}{n^2 - n_y^2} + \frac{\cos^2(\theta)}{n^2 - n_z^2} = \frac{1}{n^2} \quad (D1)$$

The values of n_x , n_y , and n_z are the principal index values which depend on the crystal material and light wavelength. The angles are the standard spherical coordinate angles. The form of Eq. (D1) is that given in *Optics* by Klein and Furtak [74] and *Quantum Electronics* by Yariv. It is equivalent to the form given by Sutherland on pages 9 and 53. The Fresnel equation applies to both uniaxial and biaxial crystals.

Given a propagation direction inside the crystal (θ, ϕ) , the only other variable in the Fresnel equation is n . Assuming values for (θ, ϕ) and solving Eq. (D1) for n , one finds a quadratic equation in n^2 with two positive roots: n_1 and n_2 . These two roots correspond to the two rays inside the crystal with field polarizations perpendicular to one another⁵. In uniaxial crystals, one of the roots is constant (called the ordinary index) while the value of the other varies with propagation direction (called the extraordinary index). In biaxial crystals, both rays behave like the extraordinary ray of a uniaxial crystal, that is, each ray's refractive index varies continuously with input angle. A simplification in biaxial crystals occurs when the propagation direction lies in a principal plane: XZ ($\phi = 0$), YZ ($\phi = \pi/2$), or XY ($\theta = \pi/2$). When light propagates in a principal plane of a biaxial crystal, one of the two indices remains constant with propagation direction just as in a uniaxial crystal.

For a non-linear crystal to convert into other wavelength of a significant portion of the incident light, a condition known as phase matching must be met. Phase matching occurs when the phase velocities of all the different-wavelength beams propagating in the crystal are the same. In other words, light at each wavelength of interest must experience the same index of refraction. Such a condition can often be met provided the light propagates in the crystal in the right direction and with the right polarization. The convention for OPOs is to list the wavelengths in ascending order such that $\lambda_{p1} < \lambda_{p2} <$

⁵See Klein and Furtak Chapter 9 for a proof.

λ_d , where the subscripts follow the notation used in Sutherland. The propagation type (ordinary or extraordinary) follows in the same order where the letter o describes an ordinary ray and e describes an extraordinary ray, assuming propagation in a biaxial crystal is done in a principal plane. As an example, the combination oeo means the λ_{p1} light propagates as an ordinary ray; the λ_{p2} light propagates as an extraordinary ray; and the λ_d light propagates as an ordinary ray.

Phase matching angles can be calculated by finding simultaneous solutions to the Fresnel equation and one of equations (45), (46), or (47) on page 48 in Sutherland depending on the process. Though biaxial crystals are usually more complex than uniaxial crystals, the phase matching done in this particular OPO is all done in the principal planes, making the calculations simpler.

Phase Matching Angles

Table 21 shows phase matching angles calculated numerically on spreadsheet by simultaneously solving the Fresnel equation and one of Eqs. (45), (46), or (47) on page 48 of Sutherland. Because there are two indices of refraction (n_1 or n_2) associated with each wavelength, the phase matching condition with all 6 possible permutations must be tested—leaving the ooo and eee cases out—while tracking which n is ordinary and which is extraordinary as the o and e designation changes with principal plane. A complication occurs in the XZ plane: the ordinary and extraordinary switch at a threshold θ value. Sutherland defines this threshold value as Ω in equation (49) on page 53. Ω is also referred to in Table 16 on page 61 of Sutherland. In the doubling case, the sum-frequency-generation (SFG) condition must be used to find all possible phase-matching angles. Other quantities in Table 21 are d_{eff} and ρ where d_{eff} is measure of how effective a given set of conditions are at generating additional wavelengths (the greater the magnitude of d_{eff} the better) and ρ is the walk-off angle at which the ordinary and extraordinary rays separate (the smaller the better).

The crystal in the seed OPO was 12-mm long and was cut for o-e-o phase matching. The two crystals in the power OPO were 12 x 12 x 10 mm long and cut for o-

o-e phase matching. The two power OPO crystals were aligned with one another so the walk-off produced in the first crystal was reversed in the second.

The values of d_{eff} given in Table 21 are from the SNLO program (QMIX table) since efforts to calculate them independently were unsuccessful. Calculations for the walk-off angle (ρ) based on the expression given by Sutherland on page 89 gave results that coincided with the values given by the SNLO program.

Table 21. Phase Matching Angles, d_{eff} , and ρ .

Doubling	ϕ	θ	d_{eff} (pm/V)	ρ (mrad)
oee	0°	49.124°	0	--
oee	90°	39.586°	0	--
oeo	90°	69.604°	-1.87	30.89
eo _e	23.480°	90°	3.35	3.15
Seed OPO	ϕ	θ	d_{eff} (pm/V)	ρ (mrad)
oee	0°	42.518°	0	--
oeo	0°	47.738°	-2.66	53.66
oee	90°	32.056°	0	--
oeo	90°	37.584°	-1.22	46.59
Power OPO	ϕ	θ	d_{eff} (pm/V)	ρ (mrad)
oee	0°	36.366°	0	--
oeo	0°	48.884°	-2.71	0
ooe	0°	54.769°	-2.94	44.3
oee	90°	26.069°	0	--
oeo	90°	40.100°	-1.29	0
ooe	90°	46.392°	-1.45	42.97

** indicates the type of phase matching used in the OPO

Efficiency (η)

The efficiency value indicates what fraction of the available pump energy is converted into signal and idler energy. Efficiencies were calculated based on the expressions in Table 4 on page 39 of Sutherland. The doubling case uses the second-harmonic-generation (SHG) expression. Calculated values of η are shown in Table 22. The calculated SHG efficiency is greater than that measured because the actual beam is not the plane wave assumed in the theory. For real beams, much of the energy in the wings (both spatially and temporally) is unusable.

A similar discrepancy between predicted and actual efficiency also occurs in the OPO difference-frequency-generation (DFG) case for the same reasons. Table 23 shows the calculated results. Note that the 2.3 μm energy output of the power OPO is 100 mJ per pulse.

The Initial OPO Configuration

In the following description, the terms pump, signal, and idler refer to, respectfully, the short-wavelength high-energy pulses that supply the energy for wavelength conversion, the light concurrently sent into the OPO acting as a seed, and the

Table 22. Frequency Doubling Efficiency (eoe case).

n_ω	1.788166 (avg)
$n_{2\omega}$	1.88772
beam radius (mm)	1.5
energy (mJ)	70
temporal pulse width (ns)	6
intensity (MW/cm ²)	165
d_{eff} (pm/V)	3.35
$\eta_{2\omega \text{ calculated}}$	0.79
η_{actual}	0.5

Table 23. Seed OPO (oeo case)_{XZ-plane} and Power OPO (ooe)_{XZ-plane}

OPO Parameters	Seed OPO	Power OPO
pump energy (mJ)	35	700
pump temporal pulse width (ns)	6	6
pump power (MW)	5.8	117
pump radius (mm)	1.5	6
pump intensity (MW/cm ²)	83	103
signal power	5 mW	0.76 MW
η_d	0.10	0.15
η_s	0.32	0.18
η_{combined}	0.42	0.33 (single crystal)
$\eta_{\text{combined actual}}$	0.14	0.31 (both crystals)

third wavelength generated as a byproduct of the interaction between the pump and the signal. Figure 75 shows the important components of the OPO as it was originally designed with the idler output of the seed OPO acting as the signal input for the power OPO. In the Fig. 75, S1 is coated to transmit 532-nm light and to highly reflect 689-nm light; S2 is coated to transmit 532-nm light and to reflect 60% of the incident 689-nm light; and S3 is highly reflective at 689 nm. S3 is connected to a piezo controlled mount. P1 is coated to transmit 1064-nm light and to highly reflect 2.3- μm light; P2 is coated to transmit 1064-nm light and to reflect 60% of the incident 2.3- μm light; and P3 is highly reflective at 2.3 μm . P3 is connected to a piezo-controlled mount. As described earlier, the piezo mounts allow the resonator spacing to be altered so that the wavelength of the signal light entering the resonator matches a cavity mode of the resonator. In the seed-OPO $\lambda_{p1} = 532$ nm, $\lambda_{p2} = 689$ nm, and $\lambda_d = 2335$ nm; and in the power OPO $\lambda_{p1} = 1064$ nm, $\lambda_{p2} = 1955$ nm, and $\lambda_d = 2335$ nm. Tunability of the OPO system came from the red diode laser tunable from 680 to 693 nm. Given the fixed pump wavelength of 532 nm, the energy conservation equation

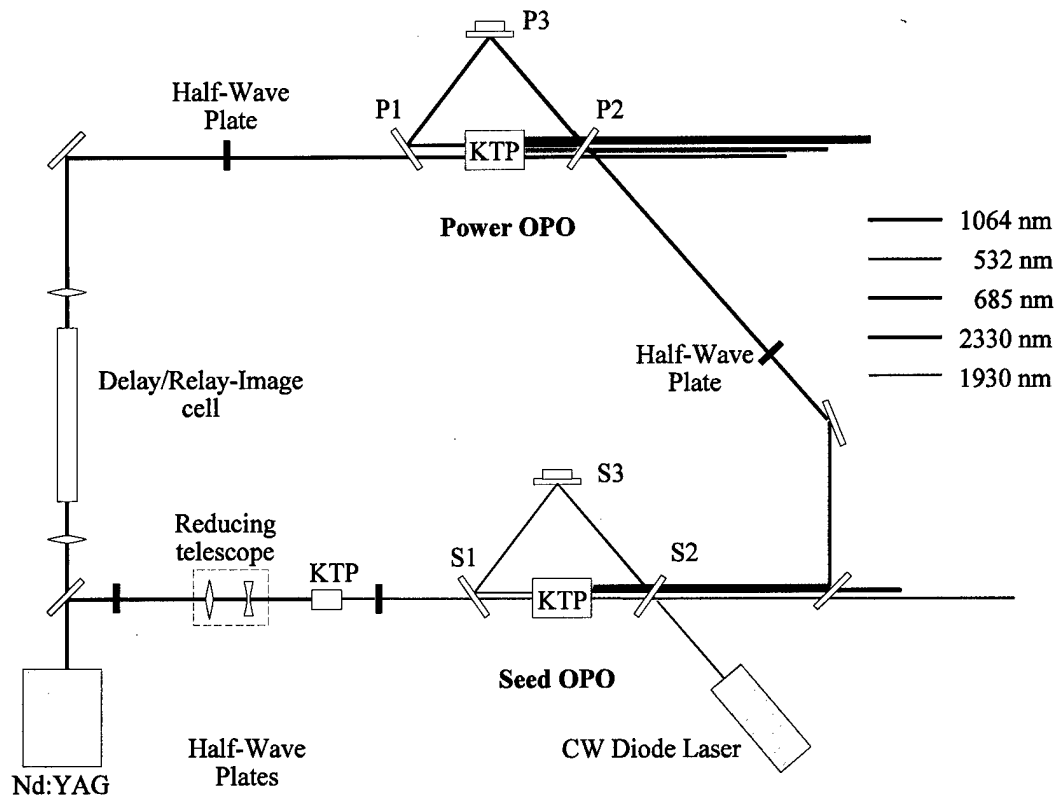


Figure 75. Power OPO. The OPO showing both the seed and power OPO oscillators as originally configured.

$$\frac{1}{\lambda_{\text{pump}}} = \frac{1}{\lambda_{\text{signal}}} + \frac{1}{\lambda_{\text{idler}}} \quad (\text{D2})$$

gives an idler wavelength that varies from 2290 to 2440 nm. Both OPOs employed flat-mirror ring resonators with the mirrors coated to reflect only the seed wavelength for the particular OPO.

The energy source for the seed and power OPO system was the same Nd:YAG laser described earlier. A 90/10 beam splitter divided the 1064-nm beam into two legs with 90% going to the power OPO and 10% going to the seed OPO. The energy sent toward the power OPO entered relay imaging cell that was part of a delay line. The image cell ensured good beam quality at the power OPO, while the delay line ensured optimal overlap between the pump and signal pulses inside the power OPO resonator.

The delay line was necessary because of the short but significant build-up time of the 2.3 micron idler in the seed OPO. A half wave plate switched the pump polarization to vertical before it entered the power OPO.

All KTP crystals were originally housed in a small ovens maintained at a temperature of 60 °C. According to the OPO's designer, laser energy could occasionally cause visible streaks to form inside the crystal. Called "gray tracking," the accumulation of streaks would eventually degrade performance. By maintaining a high crystal temperature the formation of tracks could be reversed much like the creation and subsequent annihilation of color centers in other types of crystals. Gray tracking was never observed and the ovens were eventually removed.

APPENDIX E: MODE MATCHING CIRCUIT

The purpose of the circuit is to adjust the placement of the top OPO resonator mirror (S3 in Figure 75) so that the red light leaking out of the resonator is maximized. This ensures a cavity mode is resonant with the frequency of the light coming from the diode laser. Since the amount of light exiting the resonator is proportional to the amount of light inside the resonator, maximizing one maximizes the other.

Figure 76 shows the circuit's main components. A mirror reflects the red light leaving the resonator into a detector. When the OPO is operating, the weak light from the diode is accompanied by the 10-Hz red pulses from the cavity. Efforts to remove the pulses optically proved fruitless as the red light from the diode seeds the pulses. As a result, the pulses share the seed's wavelength, polarization, and direction. Since the pulses disrupt the circuit's performance, a pulse suppression unit clips the voltage spikes out the detector's signal. The unit is made up of digital switches which shunt the detector output to ground for 2 ms during the voltage spike. While the detector is disconnected, a discharging capacitor maintains circuits input voltage. The capacitor is charged by the detector in between pulses. The Q-switch trigger from the Nd:YAG laser governs the timing of the pulse suppression.

The signal from the pulse suppression unit enters a lock-in amplifier (Stanford Research Systems Model SR510). A unity-gain buffer between the suppression unit and the lock-in amplifier provides impedance matching. For the lock-in amplifier to function, the detector signal must have a frequency component that matches the lock-in's reference frequency. A signal generator (Insteek Model GFG 8215A) supplies the lock-in's square-wave reference frequency (350 Hz). The same signal generator places a 350-Hz dither on the detector's voltage.

To create the necessary oscillation in the detector voltage, the signal generator's sinusoidal output (350 Hz) is attenuated and added to the DC voltage that drives the cavity mirror piezo mount. The AC signal drives the mirror back and forth just enough to change the amount of red light entering the resonator. The detector picks up the change in intensity and translates it into the voltage read by the lock-in amplifier.

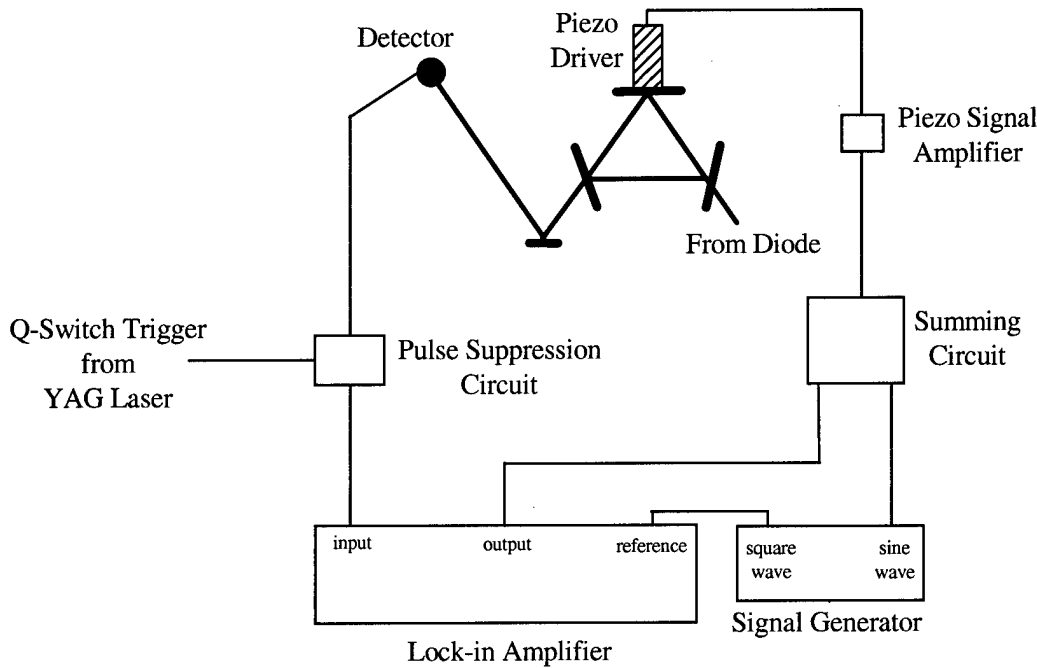


Figure 76. Main components of the mode matching circuit. The circuit maintains a cavity mode resonant with the frequency of the diode laser.

Although the frequency output of the signal generator is continuously tunable, only certain frequencies are usable. The mirror/piezo-mount system has its own resonances which are a function of the mirror mass and piezo response time. Both the frequency and amplitude of the voltage coming from the signal generator must be adjusted to avoid the resonances. Otherwise the mirror will not move smoothly back and forth at the desired frequency. The phase between the reference frequency and the dither on the detector voltage must be manually matched with the lock-in amplifier.

The output from the lock-in enters a summing circuit which integrates the signal from the lock-in and places the resulting positive or negative DC voltage on a capacitor. The capacitor voltage determines the direction the piezo mount moves. The 350-Hz sinusoidal signal from the signal generator is added to the capacitor voltage and passed through a buffer. The combined signal then enters a piezo driver (Thor Labs Model MTD691) which amplifies the signal and sends it to the mirror mount.

REFERENCES

1. A. E. Belikov, "Rotational relaxation time in CO free jets," *Molec. Phys.*, **98**, No. 6, 2000, pp 343-347.
2. S. Chandra, V. U. Maheshwari, and A. K. Sharma, "Einstein A-coefficients for vibrotational transitions in CO," *Astron. Astrophys. Suppl. Ser.*, **117**, 1996, pp 557-559.
3. J. Varan and P. E. Marik, "Carbon monoxide poisoning," *The Internet Journal of Emergency and Intensive Care Medicine*, **1**, No. 2, 1997. See: <http://www.ispub.com/journals/JEICM/Vol1N2/CO.htm>.
4. Dr. A. A. Ionin, private communication, May 1999.
5. A. D. Colley, et. al., "High brightness slab waveguide carbon monoxide laser," *Appl. Phys. Lett.*, **64**, No. 22, 30 May 1994, pp. 2916-2918.
6. N. G. Basov, et. al., "Efficient pulsed first-overtone CO laser operating within the spectral range of 2.5-4.2 μ m," *IEEE J. Quantum Electron.*, **36**, No. 7, July 2000, pp. 810-823.
7. A. J. Sauval, et. al., "On the accuracy of CO line positions for high resolution IR stellar spectroscopy," *Astronomy and Astrophysics*, **265**, No. 1, Nov 1992, pp. 355-359.
8. S. P. Belov, et. al., *Ap. J.*, **393**, 1992, p. 848.
9. L. D. Thomas, W. P. Kraemer, and G. H. F. Diercksen, "Rotational excitation of CO by He impact," *Chemical Physics*, **51**, 1980, pp. 131-139.
10. S. Green and P. Thaddeus, "Rotational excitation of CO by collisions with He, H, and H₂ under conditions in interstellar dust clouds," *Astrophysical Journal*, **205**, 1 May 1976, pp. 766-785.
11. V. M. Devi, et. al., "Self-broadening and self-shift coefficients in the fundamental band of ¹²C¹⁶O," *J. Quant. Spectrosc. Radiat. Transfer*, **60**, No. 5, 1998, pp. 815-824.
12. T. Drascher, et. al., "Temperature-dependent line shift and broadening of CO infrared transitions," *J. Mol. Spectrosc.*, **192**, 1998, pp. 268-276.
13. C. K. N. Patel and R. J. Kerl, "Laser oscillation on the X'Σ+ vibrational rotational transitions of CO," *Applied Physics Letters*, **5**, 1964, pp 81.
14. O. Svelto, *Principles of Lasers*, 4th Ed., Plenum Press, New York, 1998, pp 442.

15. C. H. Townes and A. L. Schawlow, *Microwave Spectroscopy*, Dover Publications Inc., 1975, p. 5.
16. D. C. Harris and M. D. Bertalouni, *Symmetry and Spectroscopy*, Dover Press, 1978, p. 100.
17. Herzberg, G., *Spectra of Diatomic Molecules*, 2nd Ed., Van Nostrand Reinhold Co., 1950, p. 522.
18. T. George, W. Urban, and A. Le Floch, "Improved mass-independent Dunham parameters for the ground state of CO and calibration frequencies for the fundamental band," *J. Molec. Spec.*, **165**, 1994, pp. 500-505.
19. See Ref [17], pp. 81 and 82.
20. J. O. Hirschfelder, C. F. Curtiss, and R. B. Bird, *Molecular Theory of Gases and Liquids*, John Wiley & Sons, New York, NY, 1964. ISBN: 0471400653.
21. G. D. Billing, "Vibration-vibration and vibration-translation energy transfer, including multiquantum transitions in atom-diatom and diatom-diatom collisions," in *Non Equilibrium Vibrational Kinetics*, M. Capitelli, Ed. Berlin, Germany: Springer Verlag, 1986, pp. 85-112.
22. J. M Huré and E. Roueff, "Analytic representations of rovibrational dipole matrix elements for the CO molecule and its isotopomers," *Astron. Astrophys. Suppl. Ser.*, **117**, 1996, pp. 561-568.
23. Recent experiments with electric discharge CO lasers operating on overtone optical transitions ($\Delta v = 2$) look promising and may provide a means of achieving high wall-plug efficiency while operating at desirable wavelengths. See Ref [6].
24. J. E. McCord, et. al., "Experimental investigation of an optically pumped mid-infrared carbon monoxide laser," *IEEE J. Quantum Electron.*, **35**, No. 11, Nov 1999, pp 1602-1612.
25. J. E. McCord, et. al., "Frequency-tunable optically pumped carbon monoxide laser," *IEEE J. Quantum Electron.*, **36**, No. 9, Sep 2000, pp 1041-1052.
26. J. D. White, A. Chakrabarti, and J. Reid, "High power, high efficiency optically pumped NH₃ lasers," *Appl. Phys. B*, **51**, 1990, pp 371-373.
27. L. M. Frantz and J. S. Nodvik, "Theory fo pulse propagation in a laser amplifier," *J. Appl. Phys.*, **34**, No. 8, 1963, pp 2346-2349.

28. B. C. Stuart, S. M. Cameron, and H. T. Powell, "Production, excitation, and laser dynamics of sulfur monoxide," *J. Phys. Chem.*, **98**, No. 44, 1994, pp 11499-11511.

29. S. Green, "Raman line widths and rotationally inelastic collision rates in nitrogen," *J. Chem. Phys.*, **98**, No. 1, 1 Jan 1993, pp 257-268.

30. Thermal Conductivity:
 M. P. Saksena, et. al., *Indian J. Pure appl. Phys.*, **7**, 1969, p 79.

Ultrasound:
 H. J. Bauer and H. Kosche, *Acustica*, **17**, 1966, p 96.
 P. G. Kistemaker, et. al., *Physica*, **48**, 1970, p 414.
 G. J. Prangsma, et. al., *Physica*, **64**, 1973, p 278.

31. D. Bassi, et. al., "State resolved rotational relaxation of CO in free jet expansion of He-CO mixtures," *J. Chem. Phys.*, **74**, No. 4, 15 Feb 1981, pp 2221-2227.

32. M. M. Ahern, D. A. Steinhurst, and M. A. Smith, "Rotational relaxation of CO in He, Ar, N₂, and CO free jets," *Chem. Phys. Lett.*, **300**, 12 Feb 1999, pp 681-686.

33. A. E. Belikov, M. L. Strekalov, and A. V. Storozhev, "Temperature dependence of the rotational relaxation cross-section in carbon monoxide," *Chem. Phys. Lett.*, **304**, 30 Apr 1999, pp 253-257.

34. R. G. Sharafutdinov, et. al., "State-to-state rate constants and rotational relaxation time in nitrogen," *Chem. Phys.*, **207**, 1996, pp 193-201.

35. J. P. Bouanich, et. al., "Pressure-induced lineshifts in the 2-0 band of CO self-perturbed and perturbed by He, Kr, O₂, and N₂," *J. Mol. Spectrosc.*, **179**, 1996, pp 22-31.
 N. Picque and G. Guelachvili, "Absolute wavenumbers and self-induced pressure lineshift coefficients for the 3-0 vibration-rotation band of ¹²C¹⁶O," *J. Mol. Spectrosc.*, **185**, 1997, pp 244-248.
 P. Duggan, et. al., "Testing lineshape models: measurements for v = 1-0 CO broadened by He and Ar," *J. Mol. Spectrosc.*, **186**, 1997, pp 90-98.
 P. M. Sinclair, et. al., "Line broadening in the fundamental band of CO in CO-He and CO-Ar mixtures," *J. Mol. Spectrosc.*, **191**, 1998, pp 258-264.
 T Drascher, et. al., "Temperature-dependent line shift and broadening of CO infrared transitions," *J. Mol. Spectrosc.*, **192**, 1998, pp 268-276.
 V. Malathy, et. al., "Self-broadening and self shift coefficients in the fundamental band of ¹²C¹⁶O," *J. Quant. Spectrosc. Radiat. Transfer*, **60**, No. 5, 1998, pp 815-824.
 J. C. Nicolas, et. al., "Tunable diode laser absorption spectroscopy of carbon monoxide around 2.35 μm," *Applied Optics*, **37**, No. 33, 20 Nov 1998, pp 7906-7911.
 J. Henningsen, et. al., "The 0-3 overtone band of CO: precise linestrengths and broadening parameters," *J. Mol. Spectrosc.*, **193**, 1999, pp 354-362.

36. J. J. BelBruno, J. Gelfand, and H. Rabitz, "Collision dynamical information from pressure broadening measurements: application to carbon monoxide," *J. Chem. Phys.*, **78**, Mar 1983, pp 3990-3998.
37. G. J. Rosasco, et. al., "Measurement and prediction of Raman Q-branch line self-broadening coefficients for CO from 400 to 1500K," *J. Chem. Phys.*, **90**, No. 8, 15 Apr 1989, pp 4059-4068.
38. J. P. Looney, G. J. Rosasco, L. A. Rahn, W. S. Hurst, and J. W. Hahn, "Comparison of rotational relaxation rate laws to characterize the raman Q-branch spectrum of CO at 295K," *Chem. Phys. Letters*, **161**, No. 3, Sep 1989, pp 232-238.
39. G. Millot, "Rotationally inelastic rates over a wide temperature range based on an energy corrected sudden-exponential-power theoretical analysis of Raman line broadening coefficients and Q branch collapse," *J. Chem. Phys.*, **93**, No.11, Dec 1990, pp 8001-8010.
40. G. O. Sitz and R. L. Farrow, "Pump-probe measurements of state-to-state rotational energy transfer rates in $N_2(v=1)$," *J. Chem. Phys.*, **93**, No. 11, 1 Dec 1990, pp 7883-7893.
41. As. A. Sudbo and M. M. T. Loy, "Measurement of absolute state-to-state rate constants for collision-induced transitions between spin-orbit and rotational states of $NO(X^2\Pi, v=2)$," *J. Chem. Phys.*, **76**, No. 7, 1 Apr 1982, pp 3646-3654.
42. R. A. Copeland, D. J. Pearson, and F. F. Crim, "Laser double resonance measurements of rotational energy transfer rates in $HF(v=2)$," *Chem. Phys. Letters*, **81**, No. 3, 1 Aug 1983, pp 541-546.
R. A. Copeland and F. F. Crim, "Rotational energy transfer in $HF(v=2)$: double resonance measurements and fitting law analysis," *J. Chem. Phys.*, **78**, No. 9, 1 May 1983, pp 5551-5563.
R. A. Copeland and F. F. Crim, "Rotational energy transfer in $HF(v=2)$: energy corrected sudden approximation scaling relations applied to double resonance measurements," *J. Chem. Phys.*, **81**, No. 12, 15 Dec 1984, pp 5819-5829.
Richard Alan Copeland, PhD dissertation, *Overtone vibration-laser double resonance measurements of energy transfer rates and mechanisms in $HF(v=2)$* , University of Wisconsin-Madison, 1982.
43. J. M. Robinson, et. al., "State-to-state vibrational energy transfer in DF ($v=1-3$)," *J. Chem. Phys.*, **93**, No. 5, 1990, pp 3207-3214.
Mark Alan Muyskens, PhD dissertation, *Vibrational and rotational energy transfer: relaxation of HF and DF by He , H_2 , D_2 , HF , DF , and N_2* , University of Wisconsin-Madison, 1989.

44. Ph. Bréchignac, "Transfer of rotational population in CO by IR laser double resonance," *Optics Communications*, **25**, No.1, Apr 1978, pp 53-58.
45. Ph. Bréchignac, A. Picard-Bersellini, and R. Charneau, "Direct measurement of collision-induced reorientation in CO," *J. Phys. B: Atom. Molec. Phys.*, **13**, 1980, pp 135-140.
46. M. E. Rose, *Elementary Theory of Angular Momentum*, Dover Publications, Mineola, NY, 1957. ISBN 0-486-68480-6.
- R. N. Zare, *Angular Momentum: Understanding Spatial Aspects in Chemistry and Physics*, John Wiley & Sons, New York, NY, 1988. ISBN 0-471-85892-7.
47. Ph. Bréchignac, A. Picard-Bersellini, R. Charneau, and J. M. Launay, "Rotational relaxation of CO by collisions with H₂ molecules: a comparison between theory and experiment," *Chemical Physics*, **53**, 1980, pp 165-183.
48. T. A. Brunner and D. Pritchard, "Fitting laws for rotationally inelastic collisions," *Dynamics of the Excited State*, John Wiley & Sons, 1982, pp 631-632.
49. Private communication with Dr. Michael Heaven, June 2001, Chemistry Department, Emory University, Atlanta, GA.
50. R. Fei, D. E. Adelman, T. Carrington, C. H. Dugan, and S. V. Filseth, "Rotational energy transfer in collisions between CN (X, v=2) and argon. Comparison with results for helium," *Chem. Phys. Letters*, **232**, Jan 1995, pp 547-553.
51. A. E. Belikov, M. A. Smith, "State-to-state rate coefficients for rotational relaxation of CO in Ar," *J. Chem. Phys.*, **110**, No.17, May 1999, pp 8513-8524.
52. Private communication with Dr. Michael Heaven, June 2001, Chemistry Department, Emory University, Atlanta, GA and Dr. Tony Smith, July 2001, AFRL, Albuquerque, NM.
53. J. C. Nicolas, et. al., "Tunable diode laser absorption spectroscopy of carbon monoxide around 2.35 μm ," *Applied Optics*, **37**, No. 33, 20 Nov 98, pp 7906-7911.
54. Suggestion made by Dr. Tony Smith at AFRL.
55. W. H. Press, *Numerical Recipes: The Art of Scientific Computing (Fortran Version)*, Cambridge University Press, 1989. ISBN 0 521 38330 7.

56. The arguments in this section are taken from the text by J. T. Yardley:

J. T. Yardley, *Introduction to Molecular Energy Transfer*, Academic Press, Inc., New York, New York, 1980. ISBN 0-12-768550-2. See Chapter 1.

57. A. J. McCaffery, et. al., "Rotational transfer, an angular momentum model," *J. Chem. Phys.*, **98**, No. 6, 15 March 1993, pp 4586 - 4602.

58. O. Svelto, S. Taccheo, and C. Svelto, "Analysis of amplified spontaneous emission: some corrections to the Linford formula," *Optics Communications*, **149**, April 1998, pp 277- 282; R. Tommasini and J. E. Balmer, "Amplified spontaneous emission and maximum gain-length product revised for general line shapes," *J. Opt. Soc. Am. B*, **16**, No. 4, April 1999, pp 538-545.

59. A. E. Siegman, *Lasers*, University Science Books, 1986.

60. H. H. Kee, G. P. Lees, and T. P. Newson, "Narrow linewidth CW and Q-switched erbium-doped fibre loop laser," *Electronics Letters*, **34**, No. 13, 25 June 1998.

61. D. Taverner, D. J. Richardson, L. Dong, and J. E. Caplen, "158- μ J pulses from a single-transverse-mode large-mode-area erbium-doped fiber amplifier," *Optics Letters*, **22**, No. 6, 16 Mar 1997, pp 378-380.

62. H. L. Offerhaus, N. G. Broderick, and D. J. Richardson, "High-energy single-transverse-mode Q-switched fiber laser based on a multimode large-mode-area erbium-doped fiber," *Optics Letters*, **23**, No. 21, 1 Nov 1998, pp1683-1685.

63. K. Shimoda, *Introduction to Laser Physics*, 2nd Ed (Springer Series in Optical Sciences, 1986). See chapter 7.

64. J. T. Verheyen, *Laser Electronics*, 3rd Ed (Prentice-Hall, Inc., New Jersey, 1995). See chapter 14.

65. I. Deutsch, University of New Mexico, Physics Department (unpublished Quantum Optics class notes, Fall 1999).

66. S. L. McCall and E. L. Hahn, "Self-induced transparency by pulsed coherent light," *Phys. Rev. Lett.*, **18**, No. 21, 1967, pp 908-911.

67. S. L. McCall and E. L. Hahn, "Self-induced transparency," *Phys. Rev.*, **183**, No. 2, 1969, pp 457-485.

68. N. Schupper, et. al., "Propagation of high-intensity short resonant pulses in inhomogeneously broadened media," *J. Opt. Soc. Am. B*, **16**, No. 7, 1999, pp 1127-1134.
69. H. M. Gibbs and R. E. Slusher, "Sharp-line self-induced transparency," *Phys. Rev. A*, **6**, 1972, pp 2326-2334.
70. H. Meyer and S. R. Leone, "Preparation and probing of alignment in molecular ensembles by saturated coherent pulsed laser excitation," *J. Chem. Phys.*, **105**, 1996, pp 5858-5871.
71. See Ref [65], page 671 for the pulse area and page 624 for the dipole moment in terms of the Einstein A coefficient. The polarization factor of 3, as in the example on page 675, has been assumed.
72. R. L. Sutherland, *Handbook of Nonlinear Optics*, Marcel Dekker, Inc., New York, 1996.
73. M. V. Klein and T. E. Furtak, *Optics*, 2nd Ed., John Wiley and Sons, New York, 1986.